RANDOM RAMAN LASING

A Dissertation

by

BRETT HARRISON HOKR

Submitted to the Office of Graduate and Professional Studies of
Texas A&M University
in partial fulfillment of the requirements for the degree of

DOCTOR OF PHILOSOPHY

Chair of Committee,	Marlan O. Scully
Co-Chair of Committee,	Vladislav V. Yakovlev
Committee Members,	George W. Kattawar
	Edward S. Fry
	Alexei V. Sokolov
	Aleksei M. Zheltikov
Head of Department,	George R. Welch

May 2016

Major Subject: Physics

ABSTRACT

The propagation of light in turbid media is something that is experienced by everyone, everywhere, everyday. These dynamics play an essential role in everything from the color of a material, to the multitude of colors present during a sunset. Considering the central role of these dynamics, there are still a great deal of outstanding questions that remain to be answered. Nonlinear light propagation in turbid media is one such question, with far ranging applications in biomedical imaging where it has potential to elucidate many biological processes label-free and *in vivo*. Conventional wisdom suggests that nonlinear effects, such as stimulated Raman scattering (SRS), should not play a significant role in the propagation of light through random media. The diffusive nature of elastic scattering restricts the interaction distance by limiting the depth at which high intensities can be delivered, thus reducing the efficiency of nonlinear optical effects. However, light scattering can dramatically increase the interaction length by multiply scattering the photons in a random walk type motion, making the overall outcome somewhat hard to predict.

Random Raman lasing uses SRS as the primary gain mechanism for a lasing process that receives feedback through multiple elastic scattering in the material. This is a fundamentally new optical system that pushes the boundaries of the understanding of light propagation in turbid media. The discovery of this lasing system will be presented along with several fundamental measurements of the process, some of which contrast with classical light transport theory and point towards exciting new physics. Furthermore, random Raman lasing opens the door to many exciting applications ranging from remote chemical identification at unprecedented range, in a single laser pulse, to a revolutionary new light source for imaging microscopy 10,000

times brighter than conventional sources while maintaining the low spatial coherence required for speckle-free imaging.

ACKNOWLEDGEMENTS

There is no doubt that this work would not have been possible without the tremendous support of my family, my friends, my advisers, and my colleagues. There are no words to express my tremendous gratitude for all of their support. Specifically, let me thank my advisers Dr. Marlan Scully and Dr. Vlad Yakovlev, and the rest of my committee Dr. Ed Fry, Dr. George Kattawar, Dr. Alexei Sokolov, and Dr. Aleksei Zheltikov for guiding me through this journey. I must thank my colleagues and friends from the Air Force Research Labs Dr. Benjamin Rockwell, Dr. Robert Thomas, Gary Noojin, Dr. Hope Beier, Dr. Morgan Schmidt, Dr. Michael Denton, Aurora Shingledecker, and Dr. Joel Bixler who allowed me countless hours in their labs working on these projects. This work would not have been possible without the help, guidance and thoughtful conversations with the people listed above as well as Dr. Hui Cao, Dr. Doug Stone, Dr. Alex Cerjan, Seng Fatt Liew, Dr. Brandon Redding, Dr. Luqi Yuan, Dr. Ziyun Di, Dr. Da-Wei Wang, Jonathan Thompson, John Mason, and Dr. Georgi Petrov.

Last, but not least, I would like to thank my family (my wife Brittany, my father Jim, and my mother Carolyn) for standing beside and always supporting me on this journey. Without their love and support, none of this would be possible.

TABLE OF CONTENTS

Page

LIST OF FIGURES

FIGURE Page

LIST OF TABLES

TABLE Page

1. INTRODUCTION*

1.1 Light Scattering

The scattering of light by matter is ubiquitous in everyday life. Rayleigh scattering of light from molecules in the atmosphere is responsible for the blue color of our sky, and multiple scattering in materials plays a fundamental role in the appearance of materials. It is perhaps surprising then that there are still new effects being discovered as a result of these chaotic and complicated dynamics [1–3]. The simple reason for this is that the physics of single scattering events are quite well understood, even when the wave nature of light must be considered; however, how these complicated dynamics generalize to the multiple scattering geometry, present in everything from biological tissue to powders, remains largely unknown for the general case requiring wave dynamics. Even when light can be treated as a particle, these problems are only feasible through numerical simulations, giving little insight to the intricacies of the dynamics of multiple scattering.

For light scattering off a single spherical particle, all relevant cross sections can be analytically calculated directly from Maxwell's equations. Such calculations are generally referred to as Mie scattering theory [4]. For simplicity, we will restrict ourselves to spherical particle scattering; however, non-spherical scattering can be computed numerically for large number of situations. It turns out that this is a rather general approach because randomly oriented particles, even if they aren't spherical, commonly average out to give good agreement with calculations for spherical particles of a similar size. For a spherical particle of radius r and complex index of refraction

*A portion of this chapter is reprinted with permission from "Efficient time-dependent Monte Carlo simulations of stimulated Raman scattering in a turbid medium" by B. H. Hokr, V. V. Yakovlev, and M. O. Scully, 2014, ACS Photonics, **1**, 1322-1329, Copyright 2014 by American Chemical Society

n, the total scattering cross section for light, with wavenumber k, for the particle is given by

$$\sigma_s(r) = \frac{2\pi}{k^2} \sum_{i=0}^{\infty} (2i+1) \left(|a_i(r)|^2 + |b_i(r)|^2 \right) \tag{1.1}$$

where $a_i(r)$ and $b_i(r)$ are given by

$$a_i(r) = \frac{\Psi_i(n_0 kr)\Psi_i'(nn_0 kr) - n\Psi_i(nn_0 kr)\Psi_i'(n_0 kr)}{\xi_i(n_0 kr)\Psi_i'(nn_0 kr) - n\Psi_i(nn_0 kr)\xi_i'(n_0 kr)} \tag{1.2}$$

$$b_i(r) = \frac{n\Psi_i(n_0 kr)\Psi_i'(nn_0 kr) - \Psi_i(nn_0 kr)\Psi_i'(n_0 kr)}{n\xi_i(n_0 kr)\Psi_i'(nn_0 kr) - \Psi_i(nn_0 kr)\xi_i'(n_0 kr)} \tag{1.3}$$

where n_0 is the index of refraction of the surrounding medium. The functions $\Psi(z)$ and $\xi(z)$ are related to half-integer-order Bessel functions of the first kind by

$$\Psi_i(z) = \sqrt{\frac{\pi z}{2}} J_{i+1/2}(z) \tag{1.4}$$

$$\xi_i(z) = \sqrt{\frac{\pi z}{2}} H_{i+1/2}(z), \tag{1.5}$$

and the prime notation implies a derivative with respect to the argument. The absorption coefficient can be found via the relationship

$$\sigma_a(r) = \sigma_{\text{ext}}(r) - \sigma_s(r) \tag{1.6}$$

where $\sigma_{\text{ext}}(r)$ is the extinction coefficient expressible in terms of the same Mie expansion coefficients $a_i(r)$ and $b_i(r)$ as before

$$\sigma_{\text{ext}}(r) = \frac{2\pi}{k^2} \sum_{i=0}^{\infty} (2i+1) \text{Re}\left[a_i(r) + b_i(r) \right]. \tag{1.7}$$

Provided that multiple particle effects can be neglected, the absorption and scattering

coefficients are related to the cross sections through

$$\mu_s = \int_0^\infty \sigma_s(r) N(r) \mathrm{d}r \tag{1.8}$$

$$\mu_a = \int_0^\infty \sigma_a(r) N(r) \mathrm{d}r \tag{1.9}$$

where $N(r)$ is the differential number density of scatterers. Thus, the total number density of particles in the sample, N_T would be

$$N_T = \int_0^\infty N(r) \mathrm{d}r. \tag{1.10}$$

The directional dependence of the emission is significantly more complicated, but for our purposes can be expressed in a single parameter known as the anisotropy parameter, $g = \langle \cos(\theta) \rangle$. Before we can compute this, we first need the differential scattering cross section which relates the incident intensity to the outgoing intensity

$$I_s(\rho, \theta) = \frac{\sigma_{\text{diff}}(\theta)}{\rho^2} I. \tag{1.11}$$

For spherical particles, there is no ϕ dependence on the scattering for unpolarized light. The differential scattering cross section averaged over an ensemble of spherical particles can be written as

$$\sigma_{\text{diff}}(\theta) = \frac{1}{2k^2 N_T} \int_0^\infty \left(|S_1(\theta, r)|^2 + |S_2(\theta, r)|^2 \right) N(r) \mathrm{d}r. \tag{1.12}$$

Here, $S_1(\theta, r)$ and $S_2(\theta, r)$ are known as the scattering amplitude

$$S_1(\alpha, r) = \sum_{i=1}^{\infty} \frac{2i+1}{i(i+1)} \left[a_i(r)\pi_i(\cos(\theta)) + b_i(r)\tau_i(\cos(\theta)) \right] \tag{1.13}$$

$$S_2(\alpha, r) = \sum_{i=1}^{\infty} \frac{2i+1}{i(i+1)} \left[a_i(r)\tau_i(\cos(\theta)) + b_i(r)\pi_i(\cos(\theta)) \right]. \tag{1.14}$$

The functions $\pi_i(\cos(\theta))$ and $\tau_i(\cos(\theta))$ are related to the Legendre polynomials through

$$\pi_i(\cos(\theta)) = \frac{P_i^{(1)}(\cos(\theta))}{\sin(\theta)} \tag{1.15}$$

$$\tau_i(\cos(\theta)) = \frac{\mathrm{d}}{\mathrm{d}\theta} \left[P_i^{(1)}(\cos(\theta)) \right]. \tag{1.16}$$

Now the anisotropy parameter can be expressed as

$$g = \langle \cos(\theta) \rangle = \frac{1}{\sigma_s} \int_{\Omega} \sigma_{\mathrm{diff}}(\theta) \cos(\theta) \mathrm{d}\Omega. \tag{1.17}$$

We have now defined all of the parameters required to describe light transport of unpolarized light through Monte Carlo simulations.

1.2 Monte Carlo

Undoubtedly the most common and popular methods to treat multiple light scattering are Monte Carlo simulations because of their relative simple intuitive picture and ability to handle relatively complicated boundary conditions. In a single sentence, Monte Carlo simulations treat light as a point particle which travels in a straight line until it undergoes a scattering event which is treated stochastically based on the parameters defined above. Beyond that, there are dozens of variations of this simple idea, each optimized for a particular reason or for a particular geome-

try [5–18]. Monte Carlo techniques are a generalized random walk problem, and are mathematically equivalent to the transport equation in the limit of a large sample size. All of the work which will be discussed in the following chapters involve Monte Carlo models that were developed and generalized from the incredibly popular Monte Carlo Multi-Layer (MCML) [6].

1.2.1 Random Number Generation

Monte Carlo methods involve stochastic processes, thus random number generation is a core component of the technique. In all of this work, a hybrid Tausworthe random number generator is used [19] because it is computationally efficient, has a lower memory requirement than the much larger Mersenne Twister algorithm, and has a period of approximately 2^{113} or 10^{40}, far exceeding our needs. This algorithm produces uniformly distributed random numbers which are normalized between 0 and 1; however, the simulations includes many kinds of probability distributions which must be sampled from. In general, and uniform random number, ξ, can be transformed to a random number, χ, which satisfies a distribution, $\rho(x)$, through inversion of

$$\xi = \int_a^{\chi} \rho(x)\mathrm{d}x \tag{1.18}$$

where a is the minimum value allowed for the distribution. This can be numerically integrated and inverted; however, the computational costs are severe if there are a lot of random numbers required. Thankfully, analytical solutions or alternative methods exist for common distributions. Notable to Monte Carlo simulations are the Gaussian distribution and the exponential distribution. For a Gaussian random number, there are a number of suitable techniques, but for the simulations discussed here, the Box-Muller algorithm was employed [20]. For two independent uniform random numbers,

ξ_1 and ξ_2, two independent Gaussian random numbers are obtained through

$$\chi_1 = \sqrt{-2\ln(\xi_1)}\cos(2\pi\xi_2) \tag{1.19}$$

$$\chi_2 = \sqrt{-2\ln(\xi_1)}\sin(2\pi\xi_2). \tag{1.20}$$

To sample an exponential distribution given by

$$\rho(x) = \mu e^{-\mu x} \tag{1.21}$$

Eq. 1.18 can be solved analytically to obtain a random number, χ, satisfying an exponential distribution

$$\chi = -\frac{\ln(1-\xi)}{\mu} = -\frac{\ln(\xi)}{\mu} \tag{1.22}$$

where the second equality is obtained due to the symmetry of ξ about 0.5.

1.2.2 Elastic Scattering and Boundaries

The distance a photon travels between scattering events is described by the exponential distribution,

$$\rho(d) = \mu_s e^{-\mu_s d} \tag{1.23}$$

where μ_s is the elastic scattering coefficient. Using Eq. (1.18), the dimensionless distance a photon travels to its next elastic scattering event is given by

$$s = \mu_s d = -\ln(1-\xi_1) = -\ln(\xi_1) \tag{1.24}$$

where the last step makes use of the symmetry of a uniform random number, ξ_1, around 0.5. Once s is assigned, the dimensionless length to the next boundary is

calculated by

$$s_b = \frac{(z_b - z)\mu_s}{v_z}. \tag{1.25}$$

Here, $z_b - z$ is the distance along the z-axis from the photon packet to the nearest boundary that the photon will hit, μ_s is the elastic scattering coefficient in the region the photon packet is currently in, and v_z is the z-component of the photon packet's direction vector. Next, to keep the photons synchronized, we must calculate the dimensionless length that the photon will travel in the current global time step,

$$s_t = \frac{c(i\Delta t - t)\mu_s}{n}. \tag{1.26}$$

Here, c is the speed of light in vacuum, n is the index of refraction of the current region, i is the counter that keeps track of the number of global time steps which have elapsed. Thus, $i\Delta t - t$ is a measure of how much time is left before the next synchronization. It is useful to define the dimensionless distance the photon packet will travel before it elastically scatters, encounters a boundary, or must pause to be synchronized with the other photon packets to be Δs

If s_t is less than either s and s_b, then $\Delta s = s_t$ and the photon packet will move in a straight line until the next synchronization. It will then wait for all other photon packets to reach this point before continuing. The new positions of the photon packet are given by:

$$\mathbf{r}' = \mathbf{r} + \frac{\Delta s}{\mu_s}\mathbf{v}. \tag{1.27}$$

If s is less than either s_b and s_t, then $\Delta s = s$ and the photon packet will move in a straight line to its next scattering event, using Eq. (1.27), where it will get a new

direction vector, $\mathbf{v}'$, given by [21]:

$$v'_x = \frac{v_y \sin(\phi) - v_x v_z \cos(\phi)}{\sqrt{1 - v_z^2}} \sin(\theta) + v_x \cos(\theta) \tag{1.28}$$

$$v'_y = -\frac{v_x \sin(\phi) + v_y v_z \cos(\phi)}{\sqrt{1 - v_z^2}} \sin(\theta) + v_y \cos(\theta) \tag{1.29}$$

$$v'_z = \sqrt{1 - v_z^2} \cos(\phi) \sin(\theta) + v_z \cos(\theta). \tag{1.30}$$

In the case where $|v_z| = 1$, these equations reduce to:

$$v'_x = \sin(\theta) \cos(\phi) \tag{1.31}$$

$$v'_y = \sin(\theta) \sin(\phi) \tag{1.32}$$

$$v'_z = v_z \cos(\theta). \tag{1.33}$$

The scattering angle, θ, is given by the Henyey-Greenstein distribution function,

$$\cos(\theta) = \frac{1}{2g} \left[1 + g^2 - \left(\frac{1 - g^2}{1 - g + 2g\xi_2} \right)^2 \right]. \tag{1.34}$$

Here, ξ_2 is a uniform random number between 0 and 1. In the case of isotropic scattering, the anisotropy factor, $g = \langle \cos(\theta) \rangle = 0$ the Henyey-Greenstein distribution reduces to $\cos(\theta) = 2\xi_2 - 1$. Scattering is assumed to be symmetric about the z-axis, thus the azimuthal angle is simply

$$\phi = 2\pi\xi_3, \tag{1.35}$$

where ξ_3 is another uniform random number between 0 and 1.

If s_b is less than either s and s_t, then $\Delta s = s_b$ and the photon will move in a straight line to the nearest boundary, using Eq. (1.27), where it will undergo reflection

or refraction in accordance to Fresnel's and Snell's laws. When a photon packet is incident on a boundary, either between two sample layers or between one layer and the background medium, Fresnel's law is applied to determine the probability of the photon packet reflecting off the boundary. If the index of refraction of the region that the photon is currently in, n_o, is larger than the index of refraction of region the photon is trying to transmit to, n_n, and the angle of incidence, α_i, is such that $\alpha_i > \sin^{-1}(n_n/n_o)$, then total internal reflection occurs and the photon is assigned a probability of reflecting of $R = 1$. When these conditions are not fulfilled, the probability that the photon packet reflects at the boundary is given by Fresnel's law,

$$R = \frac{1}{2}\left\{\frac{\left[n_o\cos(\alpha_t) - n_n\cos(\alpha_i)\right]^2}{\left[n_o\cos(\alpha_t) + n_n\cos(\alpha_i)\right]^2} + \frac{\left[n_o\cos(\alpha_i) - n_n\cos(\alpha_t)\right]^2}{\left[n_o\cos(\alpha_i) + n_n\cos(\alpha_t)\right]^2}\right\}. \tag{1.36}$$

The transmission angle is determined by Snell's law

$$\alpha_t = \sin^{-1}\left[\frac{n_o}{n_n}\sin(\alpha_i)\right]. \tag{1.37}$$

The photon packet then transmits at the boundary with the refracted angle α_t, if $R > \xi_4$, where ξ_4 is a uniformly distributed random number between zero and unity, otherwise the photon packet is reflected with the new direction $\mathbf{v}' = \langle v_x, v_y, -v_z\rangle$.

Once one of these three outcomes have occurred, the dimensionless distance remaining until the photon elastically scattered is updated using $s = s - \Delta s$. When $s = 0$, Eq. (1.24) is used and a new dimensionless distance to the next elastic scattering event is assigned and the process is repeated until the simulation terminates.

1.2.3 Absorption

Absorption is treated using the Russian roulette method [6,22]. In this technique each photon packet is assigned a weight, typically equal to unity to start. When a

photon travels a distance of Δs the photons new weight, w' is given by

$$w' = e^{-\mu_a(\Delta s/\mu_s)}w. \tag{1.38}$$

Once the photons weight shrinks below a threshold value, w_t, the photon has a probability of p of being removed from the simulation. In our work, we set $w_t = 10^{-6}$ to minimize the error incurred from this simplifying approximation. If the photon survives, it is given a new weight of $w' = (1/p)w$ and continues to propagate in the simulation. This has been shown to be a viable method of accurately simulating the effects of absorption while decreasing the variance of the simulations [22].

1.3 Raman Scattering

Raman scattering is the inelastic scattering of photons off the vibrational (or sometimes rotational) energy levels of molecules. During this process the photon either looses, Stokes scattering, or gains, anti-Stokes scattering, an amount of energy corresponding with the energy of the molecular level. These vibrational levels are commonly referred to as molecular fingerprints because they depend heavily on the molecular components and structure, giving Raman scattering incredible chemically sensitive contrast without the need of added dyes or tags. All of these tremendous advantages come at a significant cost, spontaneous Raman scattering is incredibly weak, only about 1 in 10^{10} photons undergo a Raman scattering even in a typical sample. Even with this significant limitation, Raman scattering has still found extensive use in practical applications ranging from cancer diagnosis [23, 24] to, the detection and identification of Anthrax [25].

Much like stimulated emission is a stronger cousin to spontaneous emission (fluorescence), stimulated Raman scattering (SRS) [26] is a stimulated, nonlinear cousin to spontaneous Raman scattering. Above a threshold value of the intensity, stimu-

lated Raman scattering produces exponential gain at the strongest Raman transition, resulting in quite efficient, laser-like emission at the Stokes frequency. Stimulated Raman scattering can result in conversion efficiencies on the order of 1 in 10 instead of 1 in 10^{10} with spontaneous Raman scattering; however, the stimulated Raman spectrum is often times limited to a single emission line, instead of the full Raman spectrum possible with spontaneous Raman, limiting specificity. Additionally, there are other nonlinear Raman processes, coherent anti-Stokes Raman scattering (CARS) and coherent Stokes Raman scattering (CSRS) that make use of molecular coherence to generate a strong chemically specific response.

1.4 Random Lasing

Random lasers are a class of lasers whose feedback is provided through multiple elastic scattering instead of a laser cavity [27]. They have received tremendous interest for the previous two decades due to their ability to thoroughly test our understanding of lasing processes [2, 28–34], while gaining additional insight into how nonlinear chaotic systems behave. Random lasers do not possess a laser cavity in the conventional sense; however, they do exhibit mode-like structure. More properly, random laser systems are best thought of as a highly multi-mode, high-loss, passive cavity formed by a disordered medium in one-, two-, or three-dimensions, that interacts non-linearly though some kind of gain mechanism to produce lasing [35]. This is a subtle statement which contains many properties that should be highlighted: First, random lasers are lasers in every since of the word, they produce laser emission through a coherent process even though the resulting emission has the properties of an incoherent light source due to the highly multi-mode nature of the emission. Second, there is a huge variation in the different gain and disordered systems used to achieve lasing [36–38]. In fact, the similarities between so many different systems is

quite surprising and points towards some very general physical dynamics, especially considering the unique effect that dimensionality has on random walk dynamics, first pointed out by Polya [39]. Lastly, the high-loss feature of the random lasing modes creates a system that allows coupling and competition between these modes in a far more rich way than traditional laser systems, allowing us to test our knowledge of topics that have been debated since the invention of the laser, such as what effects determine the laser linewidth [40, 41].

More recently, random lasers have garnered significant attention for their potential applications. They occupy a niché position acting much like a classical light bulb, while retaining the incredible brightness possible through lasing. The makes them attractive sources where laser-like brightness is desired, but the coherence of a traditional laser degrades the image [34, 42]. This has led to some new sources and applications in microscopy [38, 43]. Additional applications include laser-based displays [44] and remote sensing of chemicals [45].

In the remainder of this thesis we will highlight the discovery and initial development of random Raman lasing in a bulk three-dimensional powder. We will discuss both, the experimental, and the theoretical work that have lead the field forward thus far, including enhancing dynamics present in linear scattering, lasing threshold demonstration, nonlinear Monte Calro simulations, higher-order nonlinear dynamics, and discovery of dynamics consistent with Anderson localization. Furthermore, we will present the exciting fundamental insights and revolutionary applications that have resulted from random Raman lasing such as, kilometer-scale remote sensing in a single laser pulse and using random Raman lasers as exciting next generation light sources for microscopy.

2. SPONTANEOUS RAMAN ENHANCEMENT IN TURBID MEDIA*

2.1 Introduction

Raman spectroscopy has been widely used to obtain detailed chemical information about a system without the need for chemical markers. It has been used for a wide variety of applications including cancer diagnosis [23, 24], the detection of hazardous materials [25], and industrial quality control. Raman spectroscopy has previously been carried out in turbid media [46, 47]; however, the effect elastic scattering has on the process has yet to be investigated. In other words, is there a way to use elastic scattering to optimize Raman generation? Experimentally, colloidal solutions and metamaterials [48] offer the possibility of tuning elastic scattering to maximize the generation of a Raman signal.

As light propagates through an optically thick turbid medium, photons are elastically scattered multiple times, resulting in an increase in the distance a photon travels inside the medium. This gives the photon more opportunities to interact with the surrounding medium and generate a Raman photon, carrying with it spectroscopic information about the medium. Fig. 2.1 conceptually illustrate the idea of increased path length in the presence of elastic scattering.

Monte Carlo methods have become the gold standard for modeling light propagation in turbid media. They have previously been used to investigate the effects of elastic scattering, spontaneous Raman scattering [12, 21, 49, 50], polarization [9], fluorescence [11, 51], and amplified spontaneous emission [52]. However, elastic scattering has not been included in the parameter space of any of these investigations.

*Reprinted with permission from "Raman signal enhancement via elastic light scattering" by B. H. Hokr and V. V. Yakovlev, 2013, Opt. Express, **21**, 11757-11762, Copyright 2013 by Optical Society of America

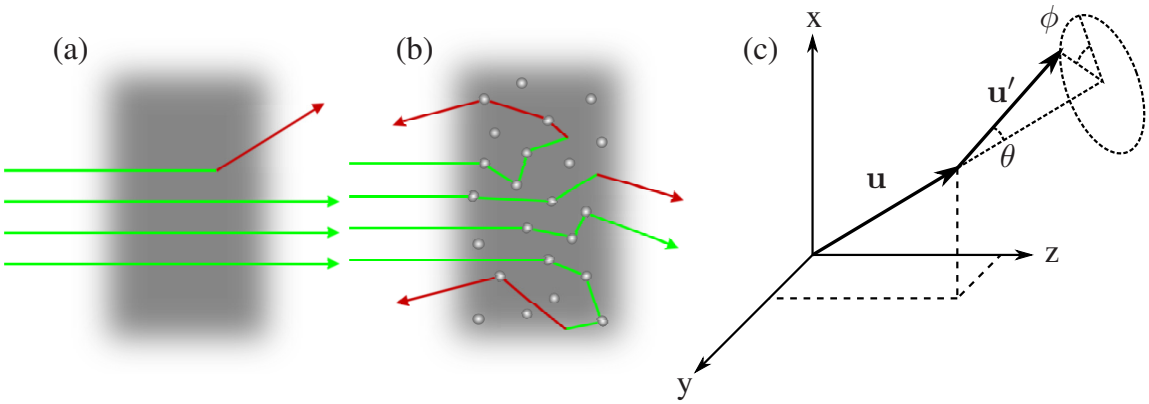

Figure 2.1: Conceptual figure illustrating how scattering increases the path length traveled inside a turbid medium: (A) without scattering, (B) with scattering, (C) coordinate system used to describe scattering. Where $\mathbf{u}$ is the direction vector before a scattering event, and $\mathbf{u}'$ is the direction vector after a scattering event.

We first discuss our Monte Carlo model for light propagation through a turbid medium. It takes into account elastic scattering, linear absorption, and spontaneous Raman scattering. This differs from previous models, in that we use a small, fixed step-size, allowing us to explore both the low scattering and high scattering regimes [53]. We demonstrate that increased elastic scattering leads to an enhancement of the Raman signal in both, the forward (transmission) and backward (reflection) directions. The spatial and temporal profiles of the Raman signal in the reflection geometry are shown to depend heavily on elastic scattering and closely mimic the distributions of the elastically scattered light [15].

2.2 Model

Consider a medium of small spherical particles with radii on the order of the wavelength of light suspended in an active Raman medium. This colloidal suspension allows the scattering mean free path to be variably controlled. Due to the small size of the scatterers and assumed large Raman cross section of the liquid, we assume all

the Raman signal is generated entirely in the liquid.

For simplicity, consider a short (1 ps full-width at half-maximum) Gaussian pump pulse with a Gaussian spatial profile normally incident on this medium. We assume the turbid medium is surrounded by vacuum and neglect reflections and refractions at the interfaces, since these will do little to change the effects we are interested in observing [6].

We are particularly interested in investigating the effects in both the low and high scattering regimes. Using the same model, we would like to accurately model the physics even when mean free paths are larger than the physical sample. To accomplish this, we use a fixed step size, Δr, significantly smaller than the shortest mean free path used in the simulation. This differs from traditional Monte Carlo simulations where each photon is propagated with a randomly distributed step size corresponding to the distance between successive scattering events.

To describe elastic scattering, linear absorption, or spontaneous Raman scattering, we define a mean free path, l_s, l_a, or l_R, respectively. During each step, there is a probability of an event given by

$$P_i = 1 - e^{-\Delta r / l_i}, \tag{2.1}$$

where i represents elastic scattering, absorption, or Raman scattering. Each mean free path represents the average distance a photon travels between a particular event.

Anisotropic elastic scattering is taken into account via the anisotropy parameter, $g = \langle \cos(\theta) \rangle$, and the Henyey-Greenstein probability distribution for the scattering angle, θ [54]. Elastic scattering is assumed symmetric around the original propagation axis, hence, ϕ is uniform. Both θ and ϕ are defined by the coordinate system illustrated in Fig. 2.1.

Raman scattering is more commonly discussed in terms of the Raman cross section. The Raman cross section relates to l_R by, $1/l_R = \sigma_R N$, where σ_R is the Raman cross section, and N is the number density of Raman scatterers. Spontaneous Raman scattering is typically very weak ($\sigma_R N \sim 10^{-7}$ mm^{-1}) for most condensed matter [55]. In order to obtain a usable signal to noise ratio, we would need to propagate about 10^9 photons per pulse. Due to computational limitations, we choose this effective cross section to be artificially large, $\sigma_R N \sim 10^{-2}$ mm^{-1}. Until pump depletion becomes non-negligible, this modification manifests itself as simply an overall multiplicative constant in the Raman signal. The parameters used in this paper did not result in pump depletion. Hence, we conclude that for the effects we are interested in, this artificially high Raman cross section does not effect the validity of our conclusions. This analysis is in agreement with previous investigations [21].

2.3 Discussion and Results

For each simulation below, the number of photons per pulse was set to 10^5 photons. We average over 25 independent pulses. The baseline parameters consist of a sample width, $w = 0.5$ mm, an anisotropy parameter, $g = 0.6$, a step size, $\Delta r = 0.001$ mm, an index of refraction, $n = 1.5$, and an effective Raman cross section of $\sigma_R N = 0.01$ mm^{-1}. We consider a full-width half-maximum temporal pulse width, $\delta\tau = 1$ ps, a full-width half-maximum beam diameter, $\delta\rho = 0.01$ mm, and a temporal pulse delay, $\Delta\tau = 5.0$ ps, for our incident pulse.

The volume concentration of scatterers is related to the scattering mean free path of the solution by $\Phi = 2d/\left(3 l_s Q_s\right)$ [56], where Φ is the volume concentration, d is the diameter of the scattering particle, and Q_s is the ratio of the particles scattering cross section to its physical cross sectional area known as the scattering efficiency factor. The scattering efficiency factor was set to 2.5. This agrees with

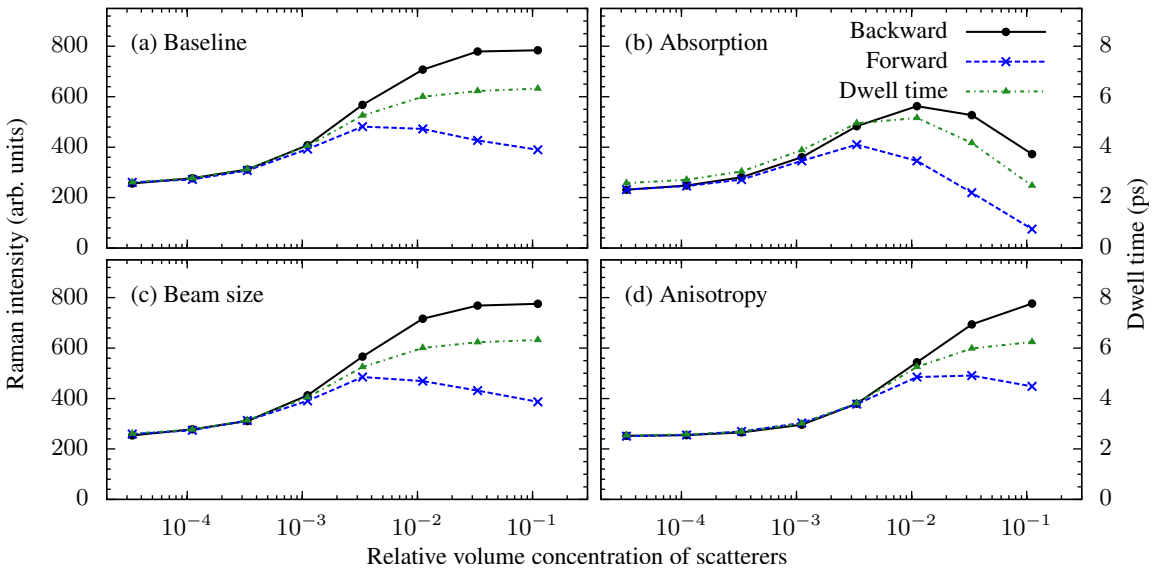

Figure 2.2: Intensity of the Raman signal and dwell time as a function of scatterer concentration: (A) the set of baseline parameters (see the text) are used, (B) a weak absorption ($l_a = 10$ mm) is included, (C) a larger diameter incident beam ($\delta\rho = 0.1$ mm) is used, (D) a larger anisotropy parameter ($g = 0.9$) is used.

the value computed from Mie scattering calculations for a ~ 1 μm diameter boron nitride particle, suspended in dimethyl sulfoxide (DMSO). DMSO was selected as the prototypical Raman active liquid due to its large Raman cross section. Because of its low absorption, available particle size, ability to suspend in DMSO, and large index mismatch with DMSO ($n_{\mathrm{BN}} \sim 2$ vs. $n_{\mathrm{DMSO}} \sim 1.5$), boron nitride was chosen to be the scatterer.

Fig. 2.2 demonstrates the results of several runs using varying parameters. In each case, we observe an enhancement of the Raman signal due to elastic scattering. The increase in the average time a photon spends inside the sample, known as the dwell time, is responsible for this enhancement. In the high scattering regime, a large portion of the incident pulse is scattered out of the sample near the surface. These photons do not travel a long distance in the sample, thus do not contribute

significantly to the Raman signal. On the other hand, photons that penetrate into the sample tend to have long path lengths, contributing greatly to the Raman signal. These two competing effects eventually compensate each other, and no additional enhancement is seen with a further increase in scattering.

In a completely transparent medium, one would expect half the Raman photons to be emitted in the forward direction and half in the backward direction due to the isotropic nature of spontaneous Raman scattering. This results in the Raman signals in the reflection and transmission geometry to be identical until the transport mean free path, $l_t = l_s/(1-g)$, becomes comparable to the thickness of the sample. At this point, reflections become dominant over transmission, leading to a preference in the backward direction.

By varying several parameters, the enhancement of the Raman signal is shown to be robust over a wide parameter space. The most significant change is due to absorption. In the low scattering regime, absorption has little effect because the path lengths traveled by the photons are small compared to l_a. However, in the high scattering regime, even a small absorption has a large effect. In a highly scattering non-absorbing medium some photons spend a very long time in the medium (illustrated by Figs. 3c and 3d). In the absence of absorption, these photons contribute significantly to the Raman signal because they experience the longest interaction distance. However, many of these photons will be absorbed before they exit the sample when a small amount of absorption is introduced.

Furthermore, the incident beam size has no effect on the total intensity of the spontaneous Raman signal. Equivalently, the pulse length will have no effect on this signal. The spatial and temporal Raman signals will, however, depend on the spatial and temporal behavior of the pump. Integrated over space and time, these effects average out. This will no longer be the case if stimulated effects are present and

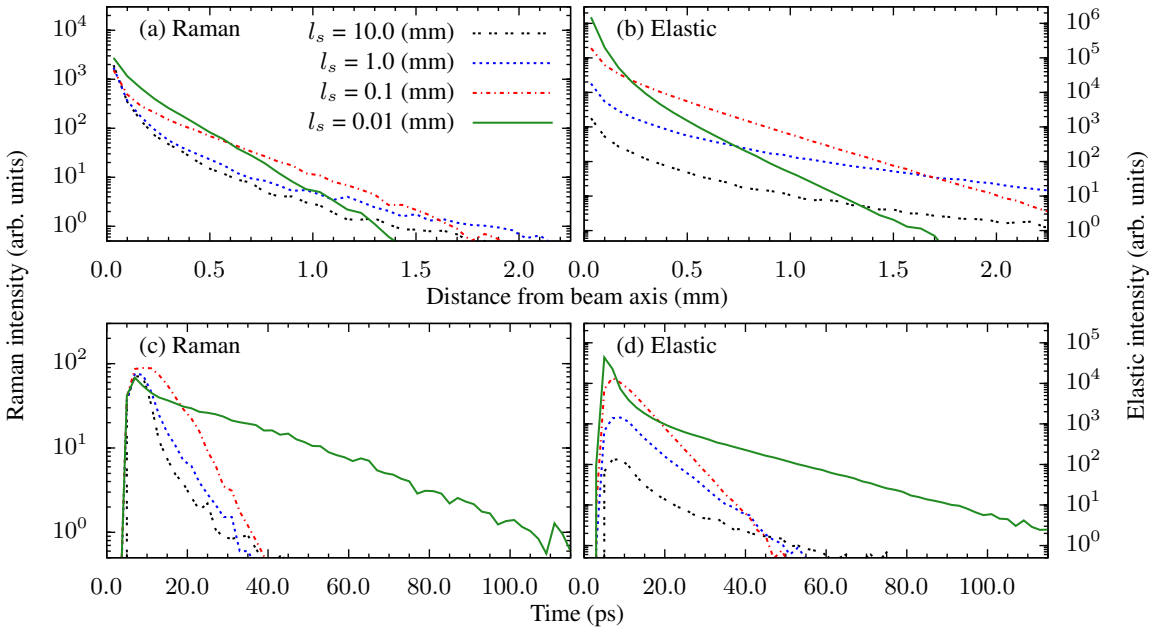

Figure 2.3: Backward spatial distribution of the: (A) Raman scattered light, (B) elastically scattered light. Backward temporal distribution of the: (C) Raman scattered light, (D) elastically scattered light.

could serve as a potential tool for analyzing whether nonlinear effects are present in a turbid medium.

When we increase the anisotropy, we see an effective shift towards lower scattering. This is because the meaningful length scale of a linear scattering problem is l_t, not l_s [57]. Hence, for a larger g, l_t is longer and the system behaves as if we have less scattering. This argument is valid for discussing linear effects, such as spontaneous Raman scattering, because such effects depend only on the average distance light travels inside the medium. We run into a problem if we try to apply this argument to a system which exhibits non-linear effects. These phenomena depend on the distribution of light inside the sample, which, in turn, depend on both l_s, and g independently.

Fig. 2.3 shows the spatial and temporal distributions of the light that exits the

sample in the reflection geometry using the same baseline parameters discussed previously. Here, for simplicity, we have assumed an infinite size detector that is in direct contact with the sample. Multiple values of l_s are shown to illustrate how the system varies with increased scattering. The first thing to notice is the spatial and temporal distributions of the Raman photons closely mimic those of the elastically scattered photons. This is not surprising because we have assumed that our sample has similar optical properties at both the fundamental and the Raman shifted wavelength. Fig. 2.3 illustrates that a technique such as spatially offset Raman spectroscopy (SORS) [58] is best suited for analyzing low scattering media. However, time resolved Raman spectroscopy [59] would be best suited for highly scattering media.

For low scattering (large l_s), the spatial distribution of the light initially broadens. This can been seen by the $l_s = 10$ mm curve decaying slightly faster than the $l_s = 1$ mm curve. Heuristically, this is because photons that emerge from the sample a significant distance from their initial location are the photons that, on average, penetrate the deepest into the sample [21]. Thus, in the case of a finite thickness sample whose thickness is small compared to l_t, these deep photons simply exit the sample as transmission photons. As scattering increases (l_s decreases) slightly, l_t correspondingly decreases, making the sample more optically thick and allowing more of these wide scattering photons to emerge as reflected photons. Once scattering increases to the point where l_t is small in comparison to the width of the sample, the sample behaves as a semi-infinite sample and the spatial distribution becomes more narrow. This can be seen by the much faster decay of the $l_s = 0.01$ mm line compared to the $l_s = 0.1$ mm line.

The temporal distribution of the backwards signal behaves in essentially the opposite way of the spatial distribution. The argument for why this is the case is the

same as above. The most striking feature in the temporal distributions is the appearance of a short spike in the $ls = 0.01$ mm line. This is a result of the photons that get reflected out of the sample in only a few bounces. The opposite effect of this is the long tail that is present in the same graph. This is generated by the photons that penetrate deep enough into the sample to where l_t is large compared to the distance to either surface, essentially trapping the photon in the medium generating the long tail.

2.4 Conclusion

A Monte Carlo model with a clear, simple physical picture has been implemented that includes elastic scattering, linear absorption, and spontaneous Raman scattering to demonstrate that increased elastic scattering enhances the generation of a spontaneous Raman signal in both the reflection and transmission geometries over a large parameter space. A strong dependence on elastic scattering is observed in both the backward spatial and temporal profiles of the detected light. Preliminary experiments currently under way using colloidal suspensions of boron nitride particles in DMSO show a good agreement with these predicted results.

3. THEORETICAL PREDICTION OF RANDOM RAMAN LASING*

3.1 Introduction

Stimulated Raman scattering (SRS) was first discovered by accident in 1962 by introducing nitrobenzene into the cavity of a ruby laser [60] and has been extensively studied both theoretically and experimentally for over 40 years. However, the behavior of stimulated Raman scattering and non-linear optical effects are relatively unknown in the presence of elastic scattering. One study has reported that the amplification of a Stokes beam can be enhanced by increased elastic scattering [61].

Random lasing was theoretically predicted by V.S. Letokhov in 1968 [62], but it took more than a quarter of a century for the random laser to be experimentally realized [63,64]. Random lasers are fundamentally similar to traditional cavity lasers except they use elastic scattering as a feedback mechanism in lieu of a Fabry-Pérot cavity. The feedback provided by elastic scattering can be either coherent or incoherent [27]. Coherent feedback occurs when elastic scattering forms closed cavities, allowing the feedback of both phase and amplitude information. In the absence of these cavities only amplitude information is maintained. This is known as incoherent feedback.

Random Raman lasing is of interest both fundamentally, for studying non-linear effects in a dramatically different environment, and practically, for developing spatially resolved spectroscopic imaging techniques in turbid environments such as biological tissue. The narrow gain bandwidth of stimulated Raman scattering makes it unlikely for a coherent feedback mode to experience positive gain. Thus, incoherent feedback is the dominant feedback mechanism. With interference effects playing a

*Reprinted with permission from "A proposal for a random Raman laser" by B. H. Hokr and V. V. Yakovlev, 2014, J. Mod. Opt., **61**, 57-60, Copyright 2013 by Taylor & Francis

small role, a Monte Carlo model is ideally suited to investigate this problem.

Monte Carlo methods have become an increasingly popular tool for modeling the propagation of light in a turbid environment. They were originally used to investigate the dynamics of light in the presence of elastic scattering and linear absorption [6], but have since been adopted to model polarization sensitive effects effects [9], fluorescence [11,51], amplified spontaneous emission [52], and spontaneous Raman scattering [12, 21, 49, 50].

Here we introduce a Monte Carlo type model that includes stimulated Raman scattering [65]. The results of the simulation are compared to known theoretical results in the no scattering, no absorption limit. Defining properties of the random Raman laser, modeled by Monte Carlo simulations, are considered in the following discussion.

3.2 Model

Unlike linear effects, non-linear optical effects, such as stimulated Raman scattering, depend heavily on the incident pulse shape. For simplicity, we assume that our pulse has both a Gaussian spatial distribution and a Gaussian temporal distribution, although arbitrary initial pulse shapes can be implemented as well [6]. To generate a Gaussian distribution, we make use of the Box-Muller transformation [20], which transforms a pair of uniform random numbers generated from a hybrid Tausworthe generator [19], into two normally distributed random numbers that comprise our

initial pulse. The generated initial conditions are

$$\begin{aligned} r_x &= \sqrt{\frac{(\delta\rho_p)^2}{4\ln(2)}\ln\left(\frac{1}{1-\xi_1}\right)}\cos(2\pi\xi_2) \\ r_y &= \sqrt{\frac{(\delta\rho_p)^2}{4\ln(2)}\ln\left(\frac{1}{1-\xi_1}\right)}\sin(2\pi\xi_2) \\ r_z &= \sqrt{\frac{c^2(\delta\tau_p)^2}{4\ln(2)}\ln\left(\frac{1}{1-\xi_3}\right)}\cos(2\pi\xi_4) - c\Delta\tau_p, \end{aligned} \tag{3.1}$$

where ξ_1, ξ_2, ξ_3, and ξ_4 are independent uniform random number, $\delta\rho_p$ is the spatial full width at half maximum diameter, $\delta\tau_p$ is the temporal full width at half maximum, $\Delta\tau_p$ is the initial pulse delay, and c is the speed of light in a vacuum. When a seed pulse is also used, it is described by an analogous expression in terms of its own set of these parameters.

The simulation progresses by propagating each photon a distance $\Delta r = \frac{c}{n}\Delta t$, where Δt is the time step, and n is the effective refractive index of the medium. This is in contrast to a large class of Monte Carlo simulations where each photon travels a random distance, described by an exponential distribution, to model elastic scattering. A fixed step size is used because the non-linear interaction requires knowledge of the location of other photons at that time. If a different step size is used for each photon in the simulation, all photons would be at different times during each step.

Furthermore, we define a probability of a photon undergoing elastic scattering, linear absorption, or spontaneous Raman scattering event given by

$$P_i = 1 - e^{-\Delta r/l_i}. \tag{3.2}$$

Here, l_i is the mean free path of a given linear process and i represents s, a, or R for elastic scattering, absorption, or spontaneous Raman scattering respectively. Care

must be taken to ensure that the step-size, Δr, is small compared to the shortest mean free path used. The mean free path relates to the respective cross section via $1/l_i = \sigma_i N_i$, where N_i is the number density of interaction centers. In the case of spontaneous Raman scattering we are required to treat the cross section as an empirical parameter since the Raman cross section is small. In order to obtain a usable signal to noise ratio, we would need approximately 10^9 photons per pulse. Computationally, we are currently limited to running approximately 10^5 photons per pulse even with large computer clusters. This artificially large Raman cross section is in agreement with previous studies [21].

Moreover, anisotropic elastic scattering is described by the Henyey-Greenstein probability distribution for the scattering angle θ [54]. The azimuthal scattering angle is assumed to be uniformly distributed. When a pump photon undergoes a spontaneous Raman scattering event it is converted to a Raman photon and the direction is randomized to correspond to the isotropic emission of spontaneous Raman scattering.

Stimulated Raman scattering is treated by defining an interaction between pump and Raman photons. For each Raman photon inside a sphere of radius r_{SRS}, centered around a pump photon, there is a "coin flip" probability of converting that pump photon into a Raman photon given by

$$p = 1 - e^{-P_{\mathrm{SRS}}\Delta r}. \tag{3.3}$$

Here, P_{SRS} is a probability per length used to describe stimulated Raman scattering and is related to the Raman gain coefficient, G. In other words, if there are n photons found inside the "interaction sphere", there are n independent coin flips, each with a probability p of converting the pump photon into a Raman photon. If

more than one "coin flip" comes up heads the first is the one used to convert the photon. When a pump photon is converted to a Raman photon via this process, the new Raman photon assumes the direction of the Raman photon whose coin flip generated the conversion. This idea of modeling non-linear effects via defining photon "interactions" could be generalized to other non-linear optical effects and is not specific only to stimulated Raman scattering.

3.3 Validation in the Zero Scattering Limit

The model used to describe linear effects is well known and has been thoroughly tested against many experiments. For this reason, we will assume that the model accurately simulates light propagation in a turbid medium. We will focus on demonstrating that our interaction model accurately describes stimulated Raman processes on their own in the absence of absorption and elastic scattering. Prior to gain saturation, stimulated Raman scattering leads to an exponential gain in the Raman signal of the form

$$I_R(z) = e^{GN_p z} I_R(0), \tag{3.4}$$

where G is the gain coefficient, N_p is the number of photons that make up the pump pulse, and z is the distance traveled through the medium. The incident intensity will be proportional to the number of photons we launch in the simulation. For convenience, we have included this proportionality constant inside the gain coefficient.

Fig. 3.1 illustrates the results of averaging 25 independent runs. Each run consisted of a 5 ps pump pulse containing 10^5 photons and a weak 5 ps seed pulse containing 100 photons. A seed pulse was included to reduce the variance in the simulation. Both pulses were given a full width at half maximum beam diameter of 0.05 mm. Elastic scattering and absorption were disabled to allow for direct comparison to equation (3.4). The parameters, $l_R = 200$ mm, $P_{\text{SRS}} = 0.1$ mm^{-1},

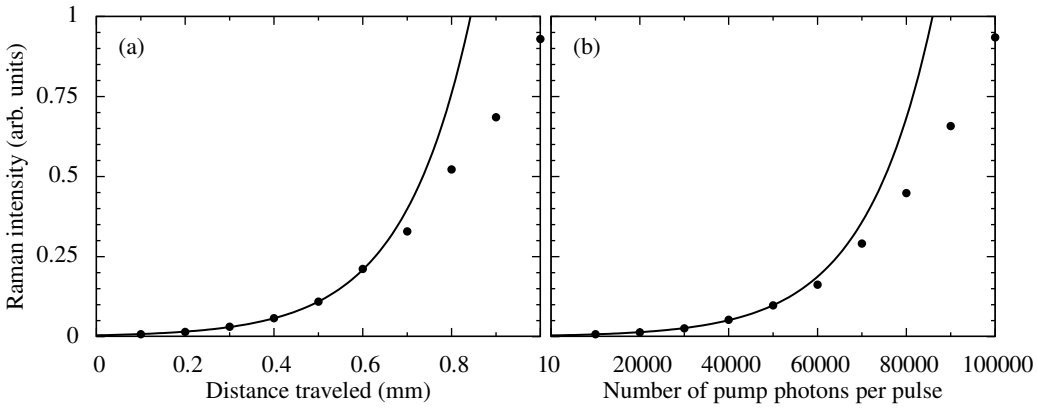

Figure 3.1: Raman intensity as a function of (A) the distance traveled through the Raman active media with the number of pump photons fixed at 10^5, and (B) the number of pump photons launched per pulse (pump intensity) with $z = 1$ mm. The dots are the results of the Monte Carlo simulation in the absence of elastic scattering and absorption. The solid line is a fit using equation (3.4) for the first 5 data points. In both fits the gain coefficient obtained was the same. At long distances and higher intensities, gain saturation is observed. The intensity units used correspond to 25,000 photons = 1.

$r_{SRS} = 0.01$ mm, and $\Delta r = 0.005$ mm, were used. As the incident pump intensity (photon number) and the sample thickness are varied independently, nearly identical behavior in the detected Raman signal is observed. The fits of the data, using equation (3.4), confirm that both variables lead to the same gain coefficient within one percent (6.466×10^{-5} mm^{-1} vs. 6.452×10^{-5} mm^{-1}). This is sufficient for us to conclude that prior to gain saturation (an assumption used in deriving equation (3.4)), the regime we will be interested in for random Raman lasing, our model is capable of accurately depicting stimulated Raman scattering. While this is not sufficient evidence to claim that this model will work perfectly in all situations, it suggests that we should be able to accurately model the features we are interested in. Ultimately, the true test of this "interaction" model's validity will come with comparison to experimental results.

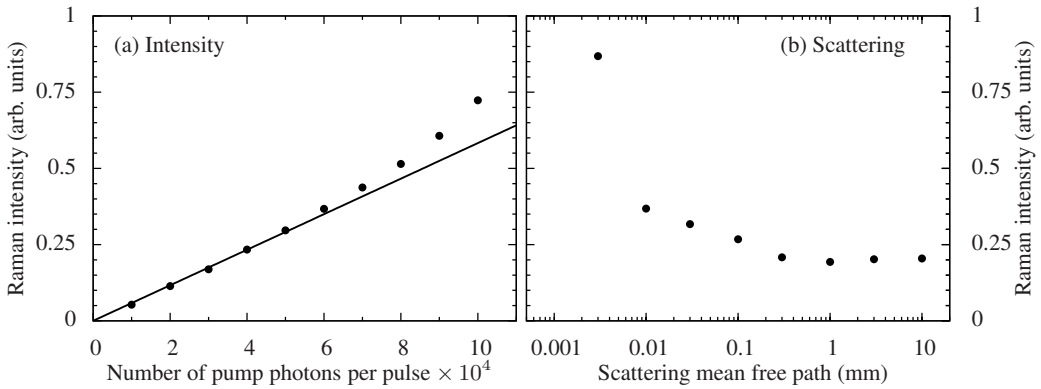

Figure 3.2: Raman intensity in the backward direction as a function of (A) incident pump intensity and (B) scattering mean free path. The dots are the results from the full Monte Carlo simulation using the parameters described in the text. (A) The line is a linear fit of the first 5 points showing a clear deviation from the linear trend associated with spontaneous Raman scattering at higher intensities. (B) The simulation shows that there is a clear threshold as the elastic scattering mean free path is decreased.

3.4 Results

Now, we turn our attention to using this model to predict some physical properties of a random Raman laser. To accomplish this, the same parameters as before are used with three exceptions: no probe pulse is included, the width of our sample will be taken to be 0.5 mm, and elastic scattering and absorption will be included using $l_s = 0.01$ mm and $l_a = 10$ mm respectively. The transverse dimensions of the sample are taken to be infinite.

Fig. 3.2 demonstrates that in a turbid medium with a sufficiently intense pump, there will be a deviation from the linear dependance on pump intensity expected when only spontaneous Raman scattering is present. This is analogous to similar measurements of traditional random lasers, and indicates that we are in the regime of stimulated Raman scattering. Therefore, this constitutes a random Raman laser in the sense that Raman gain exceeds losses and feedback is being provided solely

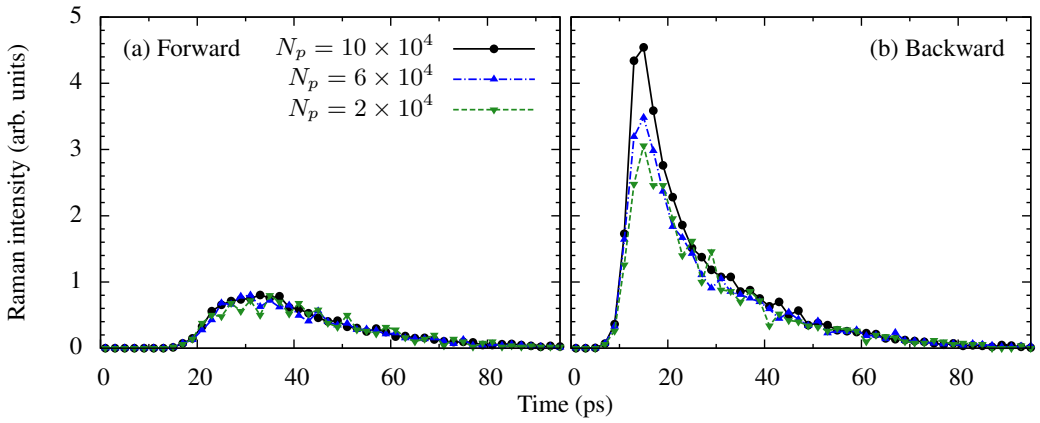

Figure 3.3: The temporal profile of the detected Raman intensity for several pump intensities in the (A) forward and (B) backward directions. The graphs have been normalized by dividing by the number of pump photons launched, N_p. The parameters used here are the same as those used in Fig. 3.2. The pump pulse was given a delay of $\Delta\tau = 12$ ps.

by elastic scattering.

In a highly turbid environment, the diffusion velocity in the medium is much smaller than the speed of light in a vacuum. This leads to a compression of the pulse as it first enters the medium. Hence, the pump is most intense at this moment, causing a large stimulated Raman signal to be generated very quickly at the front of the surface. A large amount of this signal escapes out the back of the sample and gives rise to the spike observed in fig. 3.3. This spike is an indicator of random Raman lasing.

3.5 Conclusion

A method for including stimulated Raman scattering into a Monte Carlo simulation has been developed that uses the concept of an interaction between pump and Raman photons. This model is compared against analytical results in the limiting case of no elastic scattering or absorption, and is then used to predict the temporal dynamics of a random Raman laser operating near the threshold for stimulated Ra-

man scattering. These simulations provide theoretical evidence for the presence of random Raman lasing.

4. EXPERIMENTAL DEMONSTRATION OF RANDOM RAMAN LASING*

4.1 Introduction

The propagation of light in a turbid medium is something that everyone experiences on a daily basis, yet there are many related fundamental problems that are left to be understood [66]. Everything from climate change [67], to biological imaging [68], to defending against terrorism attacks [25] benefit from a deeper understanding of how light propagates through a random medium. Throughout the last three decades numerous new phenomena, facilitated by elastic scattering, have been discovered and explored, such as coherent backscattering [1, 69], focusing via wavefront optimization [70, 71], and random lasing [2, 62]. Conventional wisdom suggests that nonlinear effects, such as stimulated Raman scattering (SRS), should not play a significant role in the propagation of light through random media. The diffusive nature of elastic scattering restricts the interaction distance by limiting the depth at which high intensities can be delivered, thus reducing the efficiency of nonlinear optical effects. However, light scattering can dramatically increase the interaction length by multiply scattering the photons in a random walk type motion, making the overall outcome somewhat hard to predict. An understanding of these dynamics are especially important for deep-tissue optical imaging utilizing multiphoton fluorescence [72, 73] and SRS [74, 75].

Raman scattering is the inelastic scattering of a photon from a molecule. The frequency of the scattered photon is determined by the frequency of a vibrational level of the molecule. The frequency shift of the Raman light with respect to the

*Reprinted with permission from "Bright emission from a random Raman laser" by B. H. Hokr, J. N. Bixler, M. Cone, J. D. Mason, H. T. Beier, G. D. Noojin, G. I. Petrov, L. A. Golovan, R. J. Thomas, B. A. Rockwell, and V. V. Yakovlev, 2014, Nat. Commun., **5**, 4356, Copyright 2014 by Macmillan Publishers Limited

pump light is unique to the molecule, making Raman spectroscopy a valuable tool for molecular and structural identification [76]. In the context of Raman lasing, spontaneous Raman scattering and SRS are analogous to fluorescence and stimulated emission, respectively. However, the nonlinearity associated with SRS distinguishes it from stimulated emission [77]. The Raman gain is proportional to the intensity of the pump. Unlike traditional lasing, energy cannot be stored by the system after the pump pulse is gone [78–81]. Thus, to observe Raman lasing, the medium must be pumped hard and fast. Furthermore, Raman lasers and traditional lasers differ in that the wavelength of light required to pump the laser does not depend on the electronic structure of the medium, and thus can be chosen to minimize absorption.

Random lasing was first predicted by V. S. Letokhov in 1968 [62], but was not experimentally observed until 1994 [63, 64]. Random lasers operate on many of the same principles as traditional lasers, except that multiple elastic scattering provides feedback in place of a Fabry-Perot cavity. Analogous to traditional lasers, random lasers have a threshold where gain exceeds losses and exponential amplification occurs at the lasing frequency [82]. Random lasers are traditionally divided into two categories: coherent and incoherent, based on the feedback that drives them [83]. Coherent feedback occurs with the generation of unstable periodic trajectories by multiple elastic scattering events [84]. These trajectories exhibit modes which are analogous to many randomly oriented ring cavities existing in the gain medium. When multiple scattering acts only to return energy back into the gain medium, but phase information is lost in the process, the system is driven by incoherent feedback [2]. Compared to the media typically used in random lasing experiments, SRS has a narrow gain bandwidth (typically less than 10 cm^{-1}). Thus, it is unlikely that a random lasing mode will lie in the gain bandwidth, making incoherent feedback the more likely dominate mechanism in random Raman lasing.

A random Raman laser uses SRS as the primary gain mechanism and relies on elastic scattering to provide feedback into the gain medium. To date, random Raman lasing has only been observed in a one-dimensional fiber system [85]. From a random walk viewpoint, one-dimensional systems are fundamentally different from three-dimensional systems. In a random walk of two or lower dimensions in an infinite space, with infinite time, the walker will eventually return to the starting location. However, in three dimensions there is no guarantee that the walker will ever return. This leads to a fundamental difference in the dynamics of photon diffusion in three dimensions.

Here, the first experimental evidence of lasing via a Raman interaction in a bulk three-dimensional random medium is presented [86]. The complicated dynamics of nonlinear pulse propagation in a turbid medium make an analytical approach to describing this problem very challenging. In order to better understand these processes, an earlier introduced [15, 65] Monte Carlo model was employed. These simulations provided a guide to the experiments and illuminated aspects of the dynamics that cannot be easily observed experimentally.

4.2 Results

4.2.1 Experimental Setup

The random Raman laser, illustrated in Fig. 4.1, was made of barium sulfate ($BaSO_4$) powder with particle diameters of 1-5 μm. $BaSO_4$ plays the role of both the Raman gain medium and the scattering centers. $BaSO_4$ was chosen due to its low absorption, both linear and nonlinear, and high scattering cross section throughout the visible spectrum. To pump the random Raman laser, short laser pulses with a center wavelength of 532 nm and a pulse duration of 50 ps were used. The incident radiation was gently focused onto the sample using a slightly offset beam expander

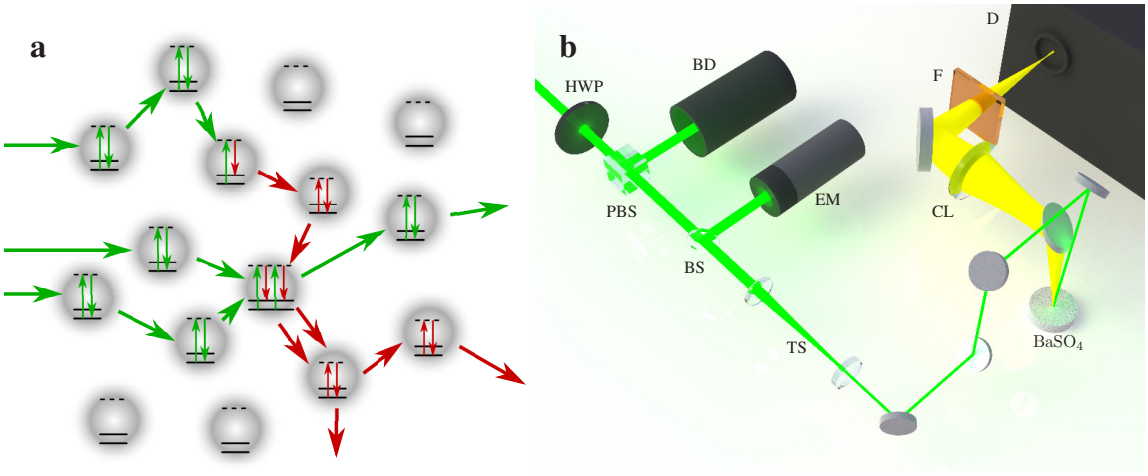

Figure 4.1: (A) Conceptual drawing illustrating random Raman lasing that is built up from spontaneous Raman scattering. Several pump photons are shown entering the medium. One undergoes spontaneous Raman scattering while the other two are simply elastically scattered. An additional Raman photon is created via stimulated Raman scattering between the two elastically scattered pump photons and the Raman photon. This is the mechanism that drives random Raman lasing. (B) Simplified diagram of the experimental setup for the random Raman laser. HWP - half-wave plate. PBS - polarized beam splitter. BD - beam dump. BS - beam splitter. EM - energy meter. TS - slightly offset 3x telescope to gently focus the beam onto the sample. $BaSO_4$ - barium sulfate powder with micron sized particles. CL - collection lens set up to image the sample on to the detector. F - filter. D - either an energy meter, spectrometer, or streak camera depending on the desired measurement.

as a compound lens, allowing for adjustments in the beam diameter incident on the sample (see Fig. 4.1). The best results were achieved with a beam diameter of about 1 mm. Smaller beam diameters limited the maximum amount of energy which could be deposited without observing damage to the sample, while the efficiency declined due to lower intensities when larger beam diameters are used. The emitted light was collected at near normal incidence and passed into an energy meter, a CCD camera, or a spectrometer via a set of mirrors and lenses for the appropriate measurements.

4.2.2 Threshold Dynamics and Efficiency

At low pump pulse energies, spontaneous Raman scattering, which manifests itself as a spectrum consisting of several lines whose relative intensities are not affected by the pump intensity, dominates the detected signal. Above the lasing threshold, the Raman spectrum collapses to a single Raman peak with a frequency shift of 985 cm^{-1} as shown in Fig 2b. At higher pump energies, a second and third peak were observed corresponding to the second- and third-order Stokes signal. These higher order signals are the result of light undergoing multiple shifts of 985 cm^{-1}. For example, the second-order Stokes signal is generated by the first Stokes light undergoing a second SRS process in which it picks up an additional 985-cm^{-1} frequency shift, resulting in a signal with a total frequency shift from the fundamental pump wavelength of 1970 cm^{-1}, and so on for the higher order processes. The presence of these higher-order processes further illustrate the substantial efficiency of the random Raman lasing process.

Once the pump energy increases beyond the threshold, (1.05 mJ in the experiment) gain exceeds losses and SRS dominates the conversion process and random Raman lasing ensues (see Fig. 4.2). At a maximum of 11.5 mJ of pump energy, 2.0 μJ of Raman signal was measured by the energy meter. Assuming a homogeneous angular distribution of the emitted Raman photons, the conversion efficiency of pump photons into Raman photons was approximately 1%. The astounding brightness of the random Raman laser is illustrated in Fig. 4.3 with a digital photograph and with a spectrum taken from a distance 21 m from the sample using a 20.3 cm off-axis parabolic mirror as a collection optic. This demonstrates that the random Raman laser is remarkably efficient considering typical conversion efficiencies for spontaneous Raman scattering are on the order of 10^{-8} [55].

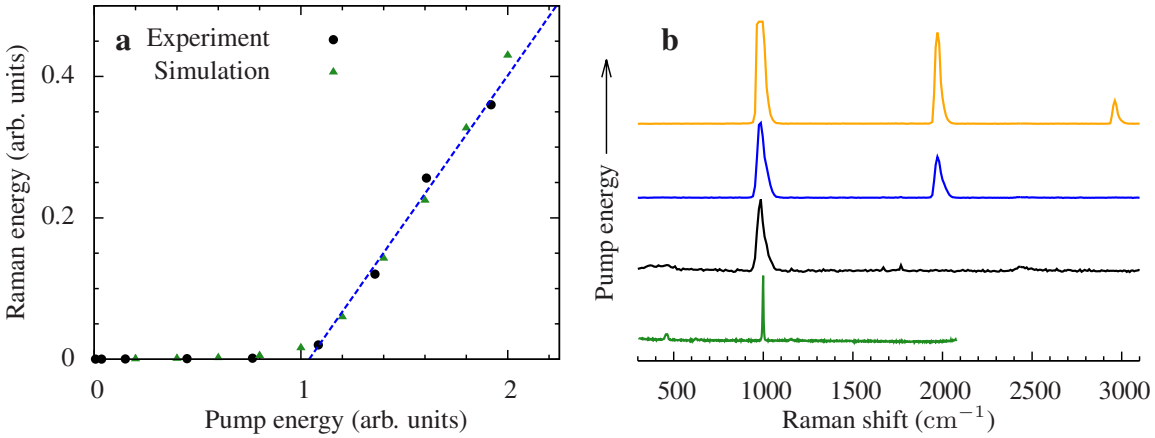

Figure 4.2: (A) Output Raman pulse energy vs incident pump pulse energy indicating a clear threshold where random Raman lasing begins. Black circles are the experimental data points, dashed blue line is a linear fit of the last 4 experimental data points, and green triangles are the results of Monte Carlo simulations. (B) SRS spectra of $BaS0_4$ powder at various pump powers illustrating the presence of higher order Raman transitions. The spontaneous Raman spectrum of $BaSO_4$ is shown for comparison, but was taken with a much higher resolution spectrometer. All spectra have been normalized to fit on the same scale, and the widths of the SRS spectral peaks were limited by the resolution of the spectrometer used.

Furthermore, a distinct feature of random Raman lasing is found in the dramatic variation of the beam profile of the emitted radiation on the surface of the sample. Below the lasing threshold, the spatial distribution of the emitted light of the random Raman laser is very broad and is due to spontaneous Raman scattering (see Fig. 4.4). This is the result of deep penetrating photons which spend a longer time in the medium, leading to a greater chance of inelastic scattering through Raman processes [15]. These deep-penetrating photons have a larger probability of exiting the sample with large radial offsets. However, above the threshold, the majority of the energy is emitted from a highly localized area near the surface (see Fig. 4.4). This is primarily due to the fact that a large amount of the SRS light is generated close to the surface, resulting in much smaller radial offsets. Strong SRS generation

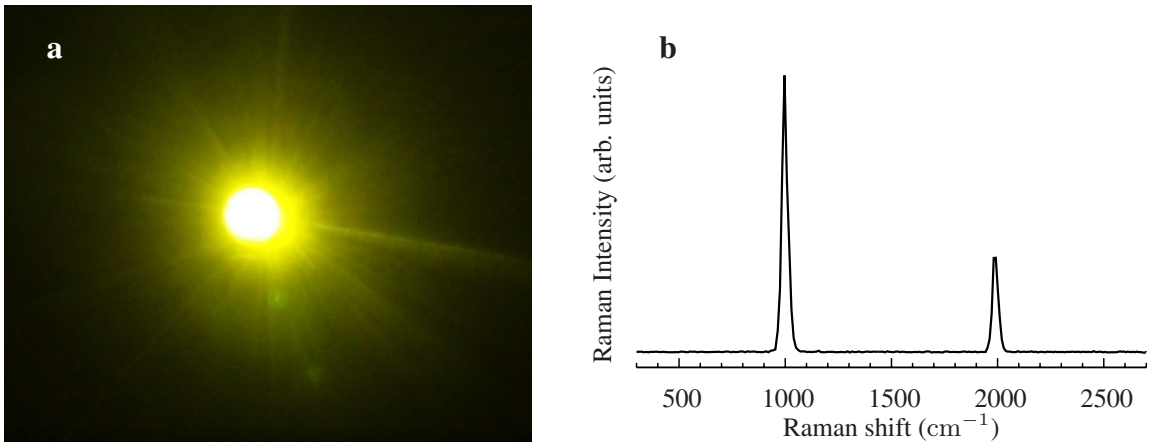

Figure 4.3: (A) Digital camera photo of random Raman lasing in $BaSO_4$ powder. (B) Spectrum of $BaSO_4$ taken through an 20.3 cm collection optic, 21 m away from the sample.

near the surface can be attributed to the slower speed of light intensity in turbid media compared to vacuum [87, 88]. Thus, photons initially arriving in the medium do not have time to leave the front surface of the sample before photons from the back of the pulse enter, causing the pulse to effectively be compressed. This light compression raises the intensity, generating a large SRS signal close to the surface.

4.3 Discussion

Many properties of the random Raman laser closely mimic those of a traditional random laser, however there are some notable differences. First, the gain bandwidth of a Raman transition is quite narrow (on the order of several cm^{-1}) and as a result, Raman lasing is monitored by measuring the relative increase of intensity of the strongest Raman line. Second, non-resonant Raman transitions involve virtual states, and are much faster than electronic transitions involving real atomic or molecular levels. Thus, transient (picosecond) dynamics of the pump pulse propagation through the medium play a pivotal role.

In our experiment, micron sized particles were chosen to ensure that no single particle promoted significant Raman gain [89, 90], thus requiring the feedback from elastic scattering to support random Raman lasing. When larger particles (hundreds of microns or larger) are used, it is possible that a single particle can support substantial Raman gain. This Raman signal would then be scattered around and would mimic random Raman lasing, however it should be stressed that this is would not be random Raman lasing. Such a situation would result in ordinary Raman lasing in a single particle which is then diffused throughout the medium by elastic scattering without subsequent amplification occurring.

4.4 Methods

4.4.1 Experimental Setup

For the pump source, the second harmonic pulse out of a Spectra Physics Quanta-Ray GCR-3RA that was injection-seeded with a 10-ps pulse out of a Spectra Physics Vanguard HM532 was used. This produces a 50-ps pulse at 532 nm. To control the pump power a half-wave plate was followed by a polarizing beam splitter. This allows us to adjust the intensity of the pumping laser without effecting the beam quality. The pump pulse is then gently focused onto the 1-5 μm $BaSO_4$ powder that was loosely packed into a small Petri dish by using a slightly offset 3x telescope consisting of a 150-mm focal length plano-convex was followed by a -50-mm focal length plano-concave lens. This setup allows us to slightly tune the spot size on the sample while maintaining a nearly collimated beam. The Fresnel reflections off of a 1.6-mm thick BK7 window, tilted at 45° from the beam axis, was used as a reference signal to measure the pump power. This signal was detected via a Coherent J4-09 energy meter. The reference signal was calibrated by measuring the ratio between the energy of the reference pulse and the energy of the pump pulse at the sample,

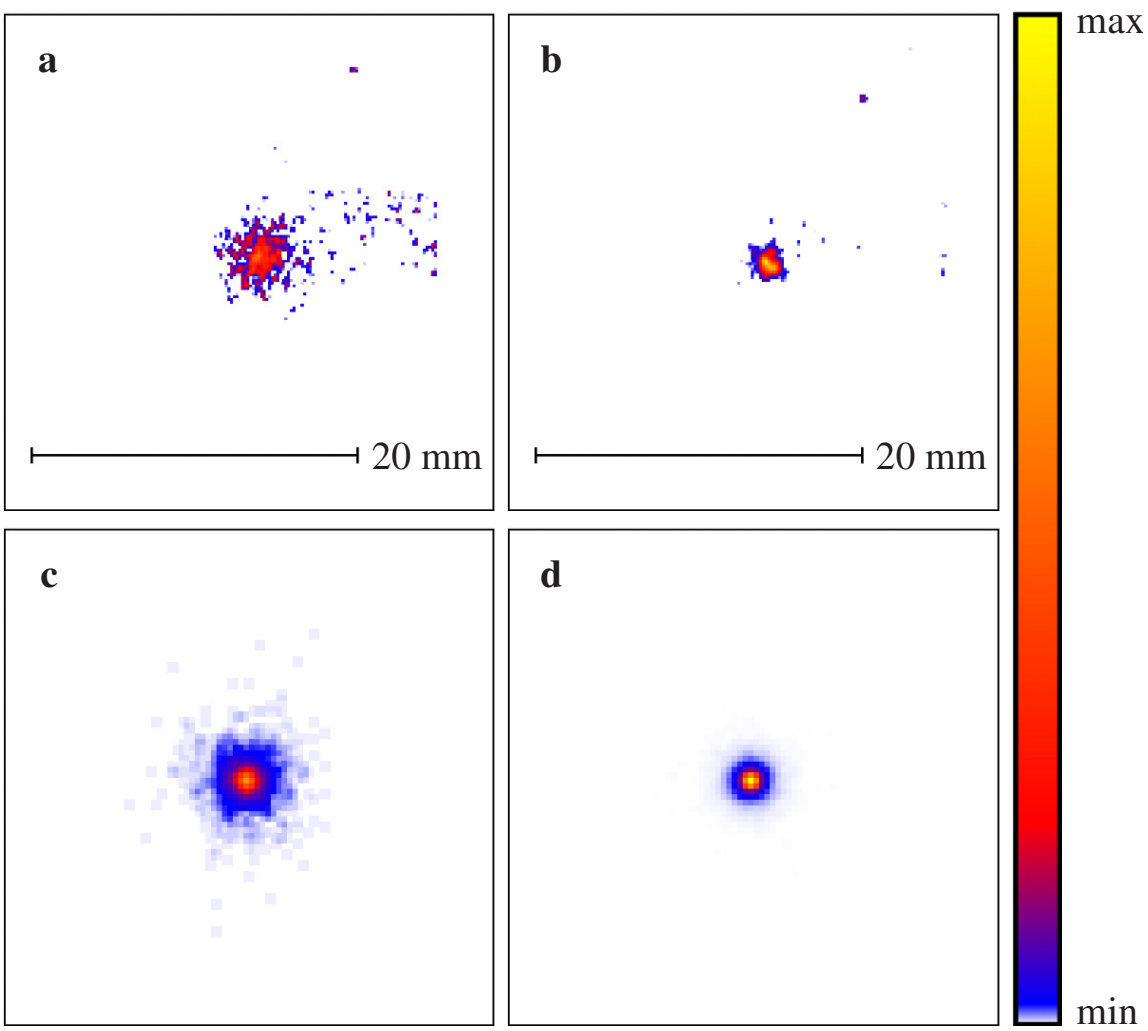

Figure 4.4: Spatial beam profiles, (A), below threshold experiment, (B), above threshold experiment, (C), below threshold simulation, and (D), above threshold simulation illustrating the significant change in the spatial profile of the Raman signal above and below the threshold. Background subtraction was preformed for the experimental images.

using an additional Coherent J4-09 energy meter.

The output Raman signal was picked off using a nearly parallel elliptical mirror, and imaged onto the detecting apparatus using a 5.08-cm diameter, 125-mm focal length lens. The excess 532-nm light was removed by using both lenses of a pair UVEX L99-LS6 YAG/KTP laser safety glasses as filters. The two lenses combined to give 9.00 OD of attenuation at 532 nm, 0.51 OD at 563 nm, and 0.47 OD at 594 nm. These absorption measurements were made using a Cary 5G spectrophotometer. These wavelengths correspond to the pump, the first-order SRS peak at 985 cm^{-1}, and the second-order SRS peak at 1970 cm^{-1}, respectively. Using an Ocean Optics USB 2000 spectrometer, it was confirmed that these filters reduce the 532-nm light to a level below that which can be measured by that spectrometer. For measuring the Raman energy in Fig. 4.4 a Coherent J3S-05 energy meter was used for the detecting apparatus. To measure the SRS spectra shown in Fig. 4.4, an Ocean Optics USB 2000 spectrometer was used. For the spontaneous Raman spectrum, an InSpectrum 300-mm spectrometer (Acton Research, Inc.) was used.

The spatial profiles shown in Fig. 4.3 were obtained using the same laser system, but the setup differed slightly. Instead of having the powder in a Petri dish and shining the laser down from the top, the $BaSO_4$ powder was placed in a 2 cm by 1 cm cuvette and imaged from the front using a Pulnix TM-6701AN monochrome CCD camera.

For the 21-m spectra an 20.3-cm off-axis parabolic mirror, with a focal length of 2.54 m, was set up across the lab at a distance of 21 m from the sample. A 5.08-cm diameter 193-mm focal length achromatic lens was placed near the focal spot of the mirror, 145 mm in front of the fiber mount of an Ocean Optics USB2000 spectrometer, in order to further focus the signal on to the slit, but without collecting any additional signal.

4.4.2 Monte Carlo Simulations

For spontaneous Raman scattering, a Monte Carlo model developed previously was used [15,65]. We will quickly review the model here for clarity. A Gaussian pulse, consisting of 10^5 photons is sent into a scattering medium characterized by scattering (l_s), absorption (l_a), and Raman (l_R) mean free paths. Photons are propagated for a fixed amount of time during each step of the simulation. This is in contrast to many Monte Carlo schemes that propagate each photon by the distance to its next scattering event, thus causing all photons in the simulation to effectively have different clocks. During each step there is a probability of an event given by

$$P_i = 1 - e^{\Delta r / l_i}, \tag{4.1}$$

where i represents elastic scattering, absorption, or Raman scattering, and $\Delta r = (c/n)\Delta t$. Elastic scattering is assumed to be anisotropic and is described by the Henyey-Greenstein probability distribution, characterized by the anisotropy factor $g = \langle \cos\theta \rangle$. Spontaneous Raman scattering is assumed to be anisotropic.

To include SRS effects an interaction between a pump and Raman photons is defined. For each Raman photon inside a sphere of radius r_{SRS}, centered around the pump photon, there is a binomial probability of converting that pump photon into a Raman photon given by

$$p = 1 - e^{-P_{\mathrm{SRS}} \Delta r}. \tag{4.2}$$

Here, P_{SRS} is a probability per length used to describe stimulated Raman scattering and is related to the Raman gain coefficient, G. When a pump photon is converted the new Raman photon takes the direction of the Raman photon whose coin flip generated the conversion.

For all the simulations presented in this paper the following values for the parameters were used: $l_s = 0.005$ mm, $l_a = 10.0$ mm, $l_R = 200$ mm, $r_{\mathrm{SRS}} = 0.025$ mm, $P_{\mathrm{SRS}} = 0.1$ mm^{-1}, $n = 1.6$, $g = 0.6$, $\Delta r = 0.002$ mm. The sample was assumed to be 5 mm thick and infinite in the transverse directions to simulate an infinitely thick medium (no photons were transmitted through the sample in any run). The incident pulse was assumed to be a 40-ps full-width at half-maximum pulse with a full-width at half-maximum beam diameter of 0.1 mm To generate the data in Fig. 4.4 25 independent runs were averaged, while Figs. 3c and 3d were generated using only a single run. In order to ensure that SRS did not contribute to the below threshold data presented in Fig. 4.3 stimulated effects were disabled in this simulation.

4.5 Conclusion

We have demonstrated the first random Raman laser in a bulk three-dimensional random medium. The lasing process is characterized by a distinct threshold, which is well below the damage threshold of the materials used for these studies. While many of the features are similar to traditional random lasers, the dynamics of random Raman lasing have a few notable differences which we have elucidated with the help of Monte Carlo simulations. While this report was focused on barium sulfate, the same effect has been observed in a number of organic and inorganic powders, using both picosecond and nanosecond laser pulses. Future work will further explore the fundamental mechanisms behind the random Raman lasing process and elucidate the use of this strong Raman light for remote sensing and as a useful light source for microscopy.

5. NONLINEAR MONTE CARLO SIMULATIONS*

5.1 Introduction

The propagation of light in the presence of scattering is a long standing problem of fundamental importance. Everything from light based biomedical imaging techniques to Earth based telescopes are intimately effected by the scattering of light. The multiple elastic scattering which takes place in optically thick turbid media is mathematically intractable. From the viewpoint of Maxwell's equations it requires knowledge of the location and shape of each individual scatterer. Ultimately this would involve solving Maxwell's equations with tremendously complicated boundary conditions, making the problem virtually impossible. In contrast, Monte Carlo simulations describe light as discrete particles which scatter in random directions at random intervals. These discrete particles are referred to as photon packets to distinguish them from the physical quantum of light, and indicate that a single photon packet can represent many more than a single physical photon. Monte Carlo simulations allow very complex dynamics to be simulated with only the knowledge of macroscopic physical properties of the medium. This allows anisotropic elastic scattering to be described using only two bulk material properties, the scattering coefficient and the average value of the scattering angle [5,6,91,92]. Historically, the major limitation in the application of Monte Carlo simulations has been their computationally intensive nature. Advances in computing power over the years, and more recently, the advances in graphics processing unit (GPU) computing, have made this largely a concern of the past [93].

*Reprinted with permission from "Efficient time-dependent Monte Carlo simulations of stimulated Raman scattering in a turbid medium" by B. H. Hokr, V. V. Yakovlev, and M. O. Scully, 2014, ACS Photonics, **1**, 1322-1329, Copyright 2014 by American Chemical Society

In addition to elastic scattering, Monte Carlo simulations have been made to handle the effects of absorption in much the same way. However, to reduce the variation from run to run, the concept of partial absorption is commonly used [6,22]. This allows the photon packet to be partially absorbed by defining a photon weight that is reduced as the photon packet propagates through the medium. Ultimately, when the photon packet's weight is reduced below a threshold value, a Russian roulette process is used to eliminate the photon packets in a way which conserves energy [6].

Furthermore, Monte Carlo simulations have been extended to investigate other linear effects such as fluorescence [94–97] and spontaneous Raman scattering [12,15, 98,99]. Various methods have been used to accomplish this, but the ones most in line with our present approach define an appropriate probability law (Beer's law in the case of linear effects) which describes the probability of a photon packet to undergo a certain process in a given step.

Traditionally, it is thought that the diffusion of light in a turbid media renders nonlinear effects unimportant. The recent discovery of random Raman lasing shows that this is not the case when intense pulses of light are used [45,86]. Other notable advances, involving wavefront optimization hint at the possibility of being able to focus light to a smaller region inside a turbid environment, further elucidate the need for a better understanding of nonlinear optics in the presence of scattering [66,100]. In addition to random Raman lasing, nonlinear Raman effects offer the possibility for non-invasive label-free biomedical sensing and imaging deep in tissue [25,73,101–104].

To date, the only nonlinear effect to be considered by Monte Carlo techniques is multi-photon fluorescence [8,11,105]. These simulations rely on the computation of a linear response function for the medium. This is computed by propagating a point source of photons, considering only absorption and elastic scattering, through the

medium and keeping track of the photon density throughout the medium. The linear response function is then convolved with the pulse to be considered, and the effects of fluorescence are computed from the intensity distribution. This approach works well so long as the nonlinear effect remains weak and temporal dynamics can be ignored, as is often the case with multi-photon fluorescence. However, stimulated Raman scattering (SRS) is an instantaneous effect making transient dynamics important. Additionally, due to the presence of exponential gain SRS can saturate the pump pulse, making the assumption that the nonlinear effect doesn't effect the distributions of photons in the medium a poor one. Thus, in order to accurately describe the effects of SRS a new approach is required.

Here, a nonlinear Monte Carlo (NLMC) model for SRS is presented [17]. The nonlinear effects are treated by deriving probability laws for a pump photon packet to be converted to a Stokes or anti-Stokes photon packet which depend on the local density of photon packets. By treating the problem in this fashion secondary effects such as pump depletion are automatically taken into account. This process is quite general, and allows for generalization to other nonlinear effects. The model is then validated using both analytical and experimental results. In addition, the derived probability law is related back to physical parameters through comparison with one-dimensional propagation equations.

5.2 Results

5.2.1 Model

The nonlinear Monte Carlo method presented here is based on a standard Monte Carlo multi-layer (MCML) method [6]. For the sake of clarity and completeness, we will summarize the parts of the traditional MCML model that were used here.

To simulate nonlinear effects, such as SRS, knowledge is required of each photon

packet's position at a given time. To include time resolution into the simulation, a global time step, Δt, is defined. Each photon packet is propagated independently during a single global time step. However, at the end of each time step, all the photon packets must be stopped and synchronized with each other. When the photon packets are synchronized, the photon densities required for treating SRS are computed. These photon densities are then used to calculate the nonlinear photon dynamics throughout the next global time step. This method allows for highly parallel computation, and is subject only to the constraint that the photon packets cannot move far enough during a single global time step that they significantly alter the photon density. Samples with high elastic scattering are perfect from this standpoint, as multiple elastic scattering results in a speed of energy diffusion which is slow compared to the speed of light, allowing a more course global time steps to be used without sacrificing accuracy. Once the combined weight of all the photons remaining in the simulation falls below a given threshold, for all simulations here this threshold is 0.001% of the initial weight, the simulation is terminated.

5.2.1.1 Initial Conditions

Pulses of light are initialized outside the turbid medium and formed by assigning (x, y, z) coordinates to N photon packets which satisfy the profile of the desired pulse. The simplest such pulse to consider would be a pulse that is incident on the sample that has both a Gaussian spatial and temporal profile. In this case, the initial distribution function of the pulse is given by,

$$\rho(x, y, z) = \frac{1}{(2\pi)^{3/2}\sigma_r^2\sigma_\tau} \exp\left(-\frac{x^2 + y^2}{2\sigma_r^2} - \frac{(z/c - \delta\tau)^2}{2\sigma_\tau^2}\right), \tag{5.1}$$

where c is the speed of light in a vacuum, $\delta\tau$ is a delay that is assigned to keep the pulse out of the turbid medium at the start of the simulation, σ_r is the standard

deviation in both the x and y directions, and σ_τ is the standard deviation in the t direction. The $1/e^2$ width of the beam relates to the standard deviation by $w = 4\sigma_r$ and the full-width at half maximum pulse length is related by $\Delta\tau = 2\sqrt{2\ln(2)}\sigma_\tau$. The front surface of the sample is always taken to be the $z = 0$ plane. To sample a Gaussian distribution with a uniform pseudo-random number generator, the Box-Mueller method was used [20]. This produces two independent normally distributed random numbers, χ_1 and χ_2, from two independent uniform random numbers, ξ and η,

$$R = \sqrt{2\sigma^2 \ln\left(\frac{1}{1-\xi}\right)} \tag{5.2}$$

$$\theta = 2\pi\eta \tag{5.3}$$

$$\chi_1 = R\cos(\theta) \tag{5.4}$$

$$\chi_2 = R\sin(\theta). \tag{5.5}$$

In addition to Gaussian distributions, arbitrary distributions can be sampled by integrating and then inverting the following equation for χ:

$$\int_a^\chi \rho(x)\mathrm{d}x = \xi. \tag{5.6}$$

Here, a represents the minimum value of the independent variable of the distribution, and ξ is a uniformly distributed random number between 0 and 1. In order to allow arbitrary distributions to be handled, Eq. (5.6) must be numerically solved. In our implementation, the numerical integration is accomplished using Simpson's method [106] and Brent's method for the numerical inversion [107]. This produced a stable and reliable method for generating arbitrary distributions.

In addition to prescribing the initial positions of the photon packets, the initial

direction must also be specified. In the most simple case of a collimated beam normally incident on the sample, the direction vector would be identical for all photon packets and be given by $\mathbf{v} = \langle 0, 0, 1 \rangle$. A focusing pulse can also be simulated by way of a coordinate transformation from collimated space to focusing space. To start, we initialize the photon packets as if there was no lens present giving each photon packet its collimation space location, $\mathbf{r} = \langle x, y, z \rangle$. Then the focusing space coordinates for that particle are given by,

$$x' = \frac{xz}{\sqrt{x^2 + y^2}} \sin\left(2\frac{\sqrt{x^2 + y^2}}{d_0}\psi\right) \tag{5.7}$$

$$y' = \frac{yz}{\sqrt{x^2 + y^2}} \sin\left(2\frac{\sqrt{x^2 + y^2}}{d_0}\psi\right) \tag{5.8}$$

$$z' = z \cos\left(2\frac{\sqrt{x^2 + y^2}}{d_0}\psi\right). \tag{5.9}$$

Here d_0 is the diameter of lens, and ψ is the angle that the focusing cone makes with the propagation axis, given in terms of the numerical aperture by $\psi = \sin^{-1}(\mathrm{NA})$. The direction vector of these focusing photons is $\mathbf{v}' = -\mathbf{r}'/|\mathbf{r}'|$. After the velocities are assigned, the depth of focus, z_f, can be assigned by a further translation, $z' \to z' + z_f$. It should be noted that wave effects like the diffraction limit are neglected by this approach. However, in the presence of scattering this is not a major concern as the pulse will be sufficiently scattered prior to reaching a non-physical, sub-diffraction limited size.

The target sample is composed of different layers. Each layer is described by a set of parameters which determine the optical properties of that layer. These parameters are: the index of refraction, n, the elastic scattering coefficient, μ_s, the anisotropy factor, g, the absorption coefficient, μ_a, the Raman scattering coefficient, μ_R, the SRS coefficient, μ_{SRS}. For the purpose of including reflection and refraction at the

Table 5.1: Comparison of an index matched sample containing elastic scattering and absorption with previous analytical solutions and Monte Carlo simulations. The uncertainty given represents the standard deviation.

Source	Reflection	Transmission
van de Hulst, 1980	0.09739	0.66096
NLMC	0.09734 ± 0.00023	0.66104 ± 0.00028
Wang et al., 1995	0.09734 ± 0.00035	0.66096 ± 0.00020
Doronin et al., 2011	0.09741 ± 0.00027	0.66096 ± 0.00017

surface, the medium surrounding the sample is given an index of refraction, n_0, and is assumed to have no scattering or absorption.

5.2.1.2 Spontaneous Raman Scattering

Spontaneous Raman scattering is a linear process just like elastic scattering and absorption, thus it can be treated in a similar manner. The probability that a pump photon undergoes spontaneous Raman scattering over a dimensionless distance Δs is given by,

$$P_R = 1 - e^{-\beta_R(\Delta s/\mu_s)}. \tag{5.10}$$

If a uniform random number $\xi_5 < P_R$ then the photon is converted into a Raman photon. Raman scattering is assumed to be isotropic, thus the new direction vector is given by Eqns. (1.31), (1.32), and (1.33) with the scattering angles given by:

$$\cos(\theta) = 2\xi_2 - 1 \tag{5.11}$$

$$\phi = 2\pi\xi_3. \tag{5.12}$$

Multiple orders of Raman scattering could be treated, however, in our simulations we neglect these higher order Raman processes.

5.2.1.3 Stimulated Raman Scattering

To treat SRS in the simulation we must have knowledge of the distribution of Raman scattered photons. This distribution is computed by assigning a grid of voxels to the computational domain then summing up the weight of each Raman photon located in each bin. This is computed only at the end of each global time step, thus the global time step itself must be chosen small enough such that the photon distribution does not undergo large changes during the course of a single time step. The probability that a pump photon undergoes a SRS process is given by.

$$P_{\mathrm{SRS}} = 1 - e^{-\beta_{\mathrm{SRS}}\rho_R(\Delta s/\mu_s)}. \tag{5.13}$$

Here, ρ_R is the local Raman photon packet density. This is computed by summing the total weight of Raman photons in the same voxel and then dividing by the volume of the voxel. The new direction is taken to be the weighted average of the direction vectors of Raman photons in the same voxel.

5.2.2 Validation

To ensure the basic elastic scattering and absorption dynamics of NLMC are working properly, the reflection and transmission coefficients obtained with the NLMC simulation are compared to previously obtained analytical results and previous Monte Carlo simulations for an index matched sample [6, 108]. The sample considered was 0.2 mm thick with a scattering coefficient of $\mu_s = 9.0$ mm^{-1}, anisotropy factor of $g = 0.75$, and an absorption coefficient of $\mu_a = 1.0$ mm^{-1}. 25 pulses each containing 10^6 photon packets were averaged together to produce the results shown in Tab. 5.1.

To validate the treatment of index mismatched boundaries, an index mismatched semi-infinite slab was chosen as a second example. The slab was given an index of

Table 5.2: Comparison of an index mismatched sample containing elastic scattering and absorption with previous analytical solutions and Monte Carlo simulations. The uncertainty given represents the standard deviation.

Source	Reflection
Giovanelli, 1955	0.2600
NLMC	0.25993 ± 0.00029
Wang et al., 1995	0.25907 ± 0.00170
Doronin et al., 2011	0.25957 ± 0.00043

refraction of $n = 1.5$ compared to the background index of $n_0 = 1.0$. Scattering was assumed isotropic ($g = 0$) and a scattering coefficient of $\mu_s = 9.0$ and absorption coefficient of $\mu_a = 1.0$ were used. The excellent agreement with previous results are shown in Tab 5.2. These results were averaged over 25 pulses each containing 10^6 photons.

To validate the NLMC model for SRS, we will compare the simulation results to previous experimental work on random Raman lasing in barium sulfate ($BaSO_4$) powder [86]. These results illustrated in Fig. 5.1 demonstrate the excellent agreement between the NLMC model and experimental results. The sample used in the simulation was 5 mm deep with an index of refraction, $n = 1.6$, an anisotropy factor, $g = 0.6$, a scattering coefficient, $\mu_s = 200$ mm^{-1}, an absorption coefficient, $\mu_a = 0.1$ mm^{-1}, a spontaneous Raman coefficient, $\beta_R = 5 \times 10^{-4}$ mm^{-1}, and a stimulated Raman coefficient, $\beta_{\text{SRS}} = 1.5 \times 10^{-5}$ mm^2. The global time step was set to $\Delta t = 0.1$ ps and the bin size was set to $d = 0.02$ mm. A single incident pump pulse with a full-width at half maximum pulse width of 50 ps and a $1/e^2$ beam diameter of 1 mm was sent into the sample, and the Raman weight exiting the sample in the reflection geometry was totaled. To generate the different pump energies, the number of pump photon packets simulated was varied over a range from 10^4 to 2×10^5.

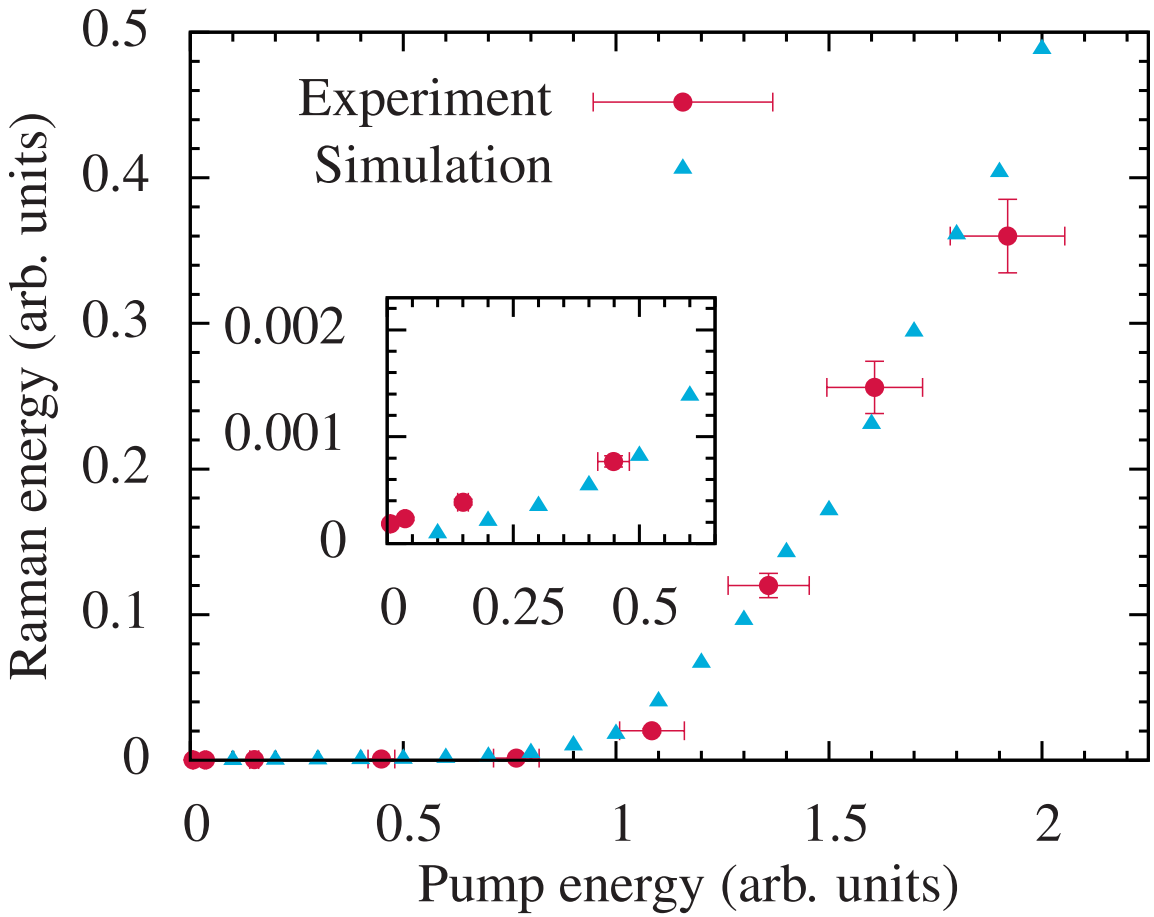

Figure 5.1: NLMC simulations compared with experimentally measured threshold data for random Raman lasing. The error bars shown represent the 7% uncertainty in the measurements of the energy meter used and the results are the average of 20 independent pulses.

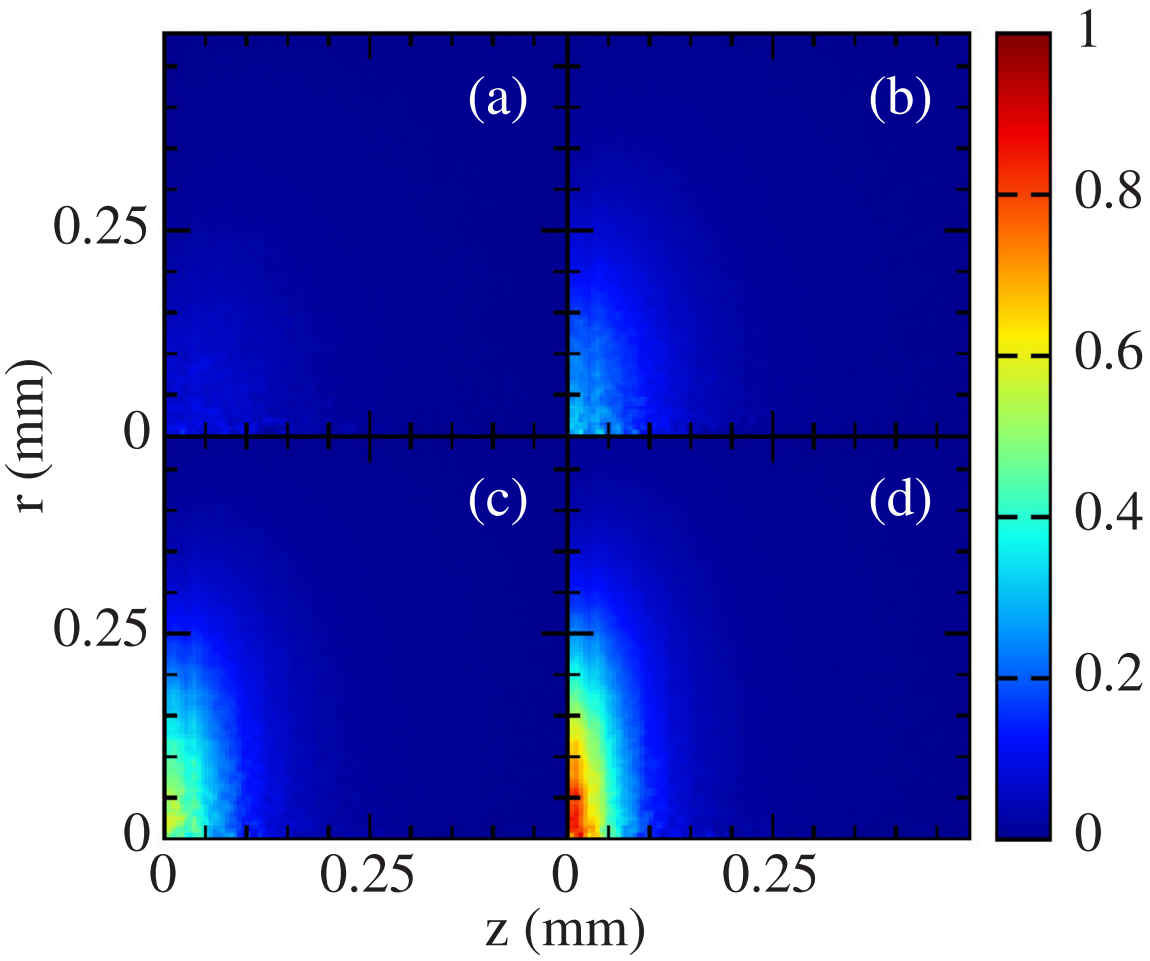

Figure 5.2: Density of Raman scattering centers for (A) 110,000, (B) 140,000, (C) 170,000, and (D) 200,000 incident pump photons. Intensities were normalized by the number of pump photons.

For each pump energy, 20 independent runs were computed.

5.2.3 Density of Raman Scattering Centers

In addition to exploring the efficiency of random Raman lasing, using the NLMC simulation, we can look at the distribution Raman scattering centers in the medium. The distribution of Raman scattering centers is something which can provide insight into random Raman lasing, but cannot be experimentally measured. Fig. 5.2 shows

the distribution of locations where a Raman photon is converted from a pump photon, known as a Raman scattering center. The parameters used were the same as above. Each graph is normalized by the number of pump photons. What is observed here is that the vast majority of Raman photons are generated in a relatively thin region of the sample, and are not the result of long path length photons. This supports the conclusion that the majority of the random Raman lasing signal is generated near the surface of the sample where pump intensity is largest. This is in contrast to a more steady state picture where longer photon paths would experience more gain. In this transient regime picture the NLMC simulations suggest that as these long path length photons continue to travel through the medium disorder induced pump depletion occurs, leading to a lower gain at later times [109]. The net result of this process is that photons trajectories which are present where pump intensities are greatest, are the ones most likely to contribute to random Raman lasing, and these photons need not be the ones with very long trajectories.

5.2.4 Scattering and Absorption Dependence

One of the most difficult difficult properties to measure with random Raman lasing is its dependence on scattering. To date, random Raman lasing has only been observed in fibers and powders, and neither of these systems offer the chance to experimentally vary the scattering and absorption properties of the medium. Some variation of the scattering coefficient would be possible in powders by pressing the sample with a known pressure, but at some point the particles will begin to make optical contact and will stop behaving like individual particles and will behave more like agglomerate particles.

While the dependence of SRS on scattering and absorption is difficult to experimentally realize, it is ideally suited for investigation with Monte Carlo simulations.

The results are shown in Fig. 5.3. All the parameters for these runs are the same as those used above except for the scattering and absorption coefficients. The pump energy was set to 200,000 photons to correspond to the largest value used in the comparison with experiment. A clear threshold for the scattering coefficient can be seen, and this value depends on the absorption coefficient. Both, the threshold and the decrease in the random Raman emission at higher scattering coefficient can be understood by the fact that scattering is both providing feedback as well as determining the excitation volume. At low scattering, there is insufficient feedback to support gain. When scattering becomes large there is sufficient feedback, but a smaller volume of the sample is excited because the pump tends to be localized near the surface of the sample. The smaller excitation volume decreases the efficiency of the process resulting in a decrease in signal for higher scattering. These conclusions are further supported by the large decrease in the signal due to absorption near the optimum scattering coefficient. Absorption limits the size of the excitation volume, shifting the most efficient scattering coefficient towards higher scattering, and decreasing the total emission, even for the rather small absorption coefficients used here.

5.3 Discussion

The probabilities used to describe the various Raman effects in the NLMC simulation can be derived from the one-dimensional equations governing the evolution of the intensity. Take for example the simplest case of spontaneous Raman scattering. In one-dimension the intensity of Raman photons can be described by,

$$\frac{\mathrm{d}I_R}{\mathrm{d}z} = \mu_R I_p. \tag{5.14}$$

In between scattering events a photon packet will travel in a straight line, thus Eq. (5.14) describes the dynamics of a photon packet where we take the z-axis to

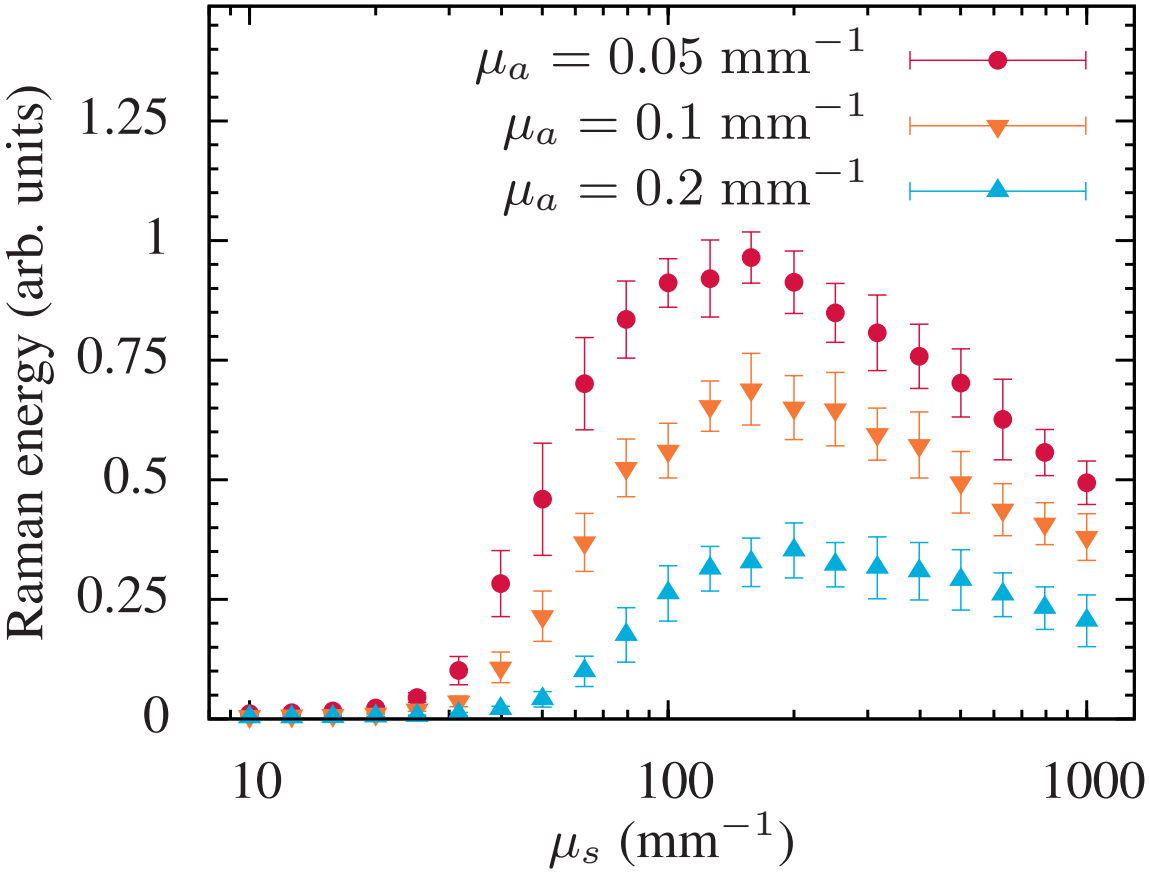

Figure 5.3: Dependence of SRS generation on scattering and absorption for a fixed pump intensity.

be the direction of propagation for that photon packet. We can integrate Eq. (5.14) over the distance that it travels in its current step,

$$\Delta I_R = \int_{z_0}^{z_0+(\Delta s/\mu_s)} \mu_R I_p \mathrm{d}z. \tag{5.15}$$

Under the assumption that this step size is small (not larger than $(c/n)\Delta t$) we can assume that the pump intensity remains constant over this small distance, thus

$$\Delta I_R \approx \mu_R(\Delta s/\mu_s) I_p. \tag{5.16}$$

These intensities can be put in terms of photon densities using the relation $I_i = \eta\hbar c(\omega_i/n_i)\rho_i$, where i represents pump, p, or Raman, R, signals respectively, and η is the number of photons represented per photon packet. With this, Eq. (5.16) can be rewritten in terms of the photon densities,

$$\Delta\rho_R = \mu_R(\omega_p/\omega_R)(n_R/n_p)(\Delta s/\mu_s)\rho_p. \tag{5.17}$$

This equation has the physical interpretation that $\mu_R(\omega_p/\omega_R)(n_R/n_p)(\Delta s/\mu_s)$ is the probability that a pump photon is converted to a Raman photon. To improve the behavior of this probability we can make use of the fact that this is small to write

$$\Delta\rho_R = \left[1 - e^{-\mu_R(\omega_p/\omega_R)(n_R/n_p)(\Delta s/\mu_s)}\right]\rho_p. \tag{5.18}$$

Now if we write

$$\beta_R = \mu_R(\omega_p/\omega_R)(n_R/n_p) \tag{5.19}$$

the probability that a pump photon packet will convert to a Raman photon packet in a given step will be given by

$$P_R = 1 - e^{-\beta_R(\Delta s/\mu_s)} \tag{5.20}$$

which is identical to Eq. (5.10).

The same method can be used to describe the more complicated nonlinear effects of SRS. In 1-dimension the Raman signal due to SRS is described by [26, 55],

$$\frac{\mathrm{d}I_R}{\mathrm{d}z} = GI_pI_R, \tag{5.21}$$

where G is the Raman gain coefficient given by [110, 111]

$$G = \frac{c\Delta N}{\hbar\pi^2 n_R^2 \omega_R^2 \omega_p \delta\omega_R} \frac{\partial\sigma}{\partial\Omega}. \tag{5.22}$$

Here, ΔN is the population density (containing any thermal distributions of states) of the molecular species leading to the gain, n_R is the index of refraction at the Stokes frequency, ω_R is the Stokes frequency, ω_p is the pump frequency, $\delta\omega_R$ is the Raman linewidth and $\partial\sigma/\partial\Omega$ is the Raman cross-section. Following the same procedure used for spontaneous Raman we end up with

$$\Delta\rho_R = \left[1 - e^{-G\eta\hbar c(\omega_p/n_p)\rho_R(\Delta_s/\mu_s)}\right]\rho_p. \tag{5.23}$$

Comparing this with Eq. (5.13) we can see that our SRS coefficient relates to the Raman gain by,

$$\beta_{\mathrm{SRS}} = G\eta\hbar c(\omega_p/n_p). \tag{5.24}$$

Monte Carlo simulations are notorious for being computationally demanding be-

cause large numbers of photon packets must be simulated to obtain accurate dynamics. In a traditional Monte Carlo scheme such as MCML, these photon packets can travel independently indefinitely. What we mean by this is that each photon packet does not require any knowledge about any other photon packets in the simulation. This makes Monte Carlo simulations trivially parallelizable and ideal for the massive computational power of modern day GPU's [14, 112].

In NLMC this is no longer the case. Due to nonlinear interactions, the photon packets require information about the distribution of other photon packets. This requires all parallel threads to stop, calculate the photon densities, and synchronize information. This reduces the level of parallelism, however the NLMC code still receives an enormous speed enhancement when run on GPU's. On our system, the GPU version of the code was able to run simulations consisting of 10^6 photon packets in just a few minutes. This run time is comparable to simulations using the CPU version of the code with only 10^4 photon packets. These simulations were run using double precision accuracy on a system that consisted of an 3.4 GHz quad core CPU (Intel; i7-2600K) with 16 GB of RAM and a GPU (NVIDIA; GeForce GTX 560 Ti).

At the heart of the NLMC model is the calculation of time resolved photon densities. The method we implemented to accomplish this is a bin sorting method. Each photon packet is sorted into bins and their weight is summed giving a measure of the photon density. This is readily parallelizable and fast, however, because a large grid must be stored, it requires a large amount of memory. On our system, GPU memory is the limiting factor to the number of photons that we can run in a single simulation. The NLMC method could be programmed in a way that this is not the case, however there would likely be a substantial degradation in performance due to the relatively slow speed at which memory is transferred to the GPU.

In condensed matter, the Raman coefficient is typically on the order of 10^{-7}

mm^{-1} [55]. With our current implementation we are limited to a few million photon packets per pulse. With an increase in GPU memory and further optimization, it is reasonable to expect that tens of millions of photons would be possible in a reasonable amount of time. However, this is still barely approaching the level where only a few photon packets undergo spontaneous Raman scattering. Because of this computational limitation, previous Raman Monte Carlo simulations have simply taken β_R to be artificially large [21, 65]. This is justified by the fact that when only spontaneous Raman effects are present β_R simply contributes a multiplicative factor on the amount of Raman generated (provided pump-depletion does not become a problem). This breaks down in the presence of SRS. When SRS effects are present, the value of both β_R and β_{SRS} play a role in the dynamics of the simulation. This can be seen in Fig. 5.4. In practice this does not appear to be as large of a problem as one would suspect. Fig. 5.1 serves as an example of the accuracy of the method even with an unphysically large β_R.

While not explicitly included in the derivation of the probabilities used in the NLMC simulations, pump depletion is taken into account in the simulation itself. The process of converting pump photon packets into Raman photon packets removes energy from the pump field reducing the probability of later photons converting. Thus, the mechanics of the simulation process itself take care of pump depletion effects. It should be noted, in any single global time step pump depletion effects are ignored because the photon densities are not updated during this time. Thus, care should be taken not to use a large time step when the simulation is in the strong saturation regime.

In the NLMC simulations there are two parameters which control the accuracy of the simulations when nonlinear effects are present, the global time step, Δt, and the photon density bin size, d. In practice these two should be matched such that during

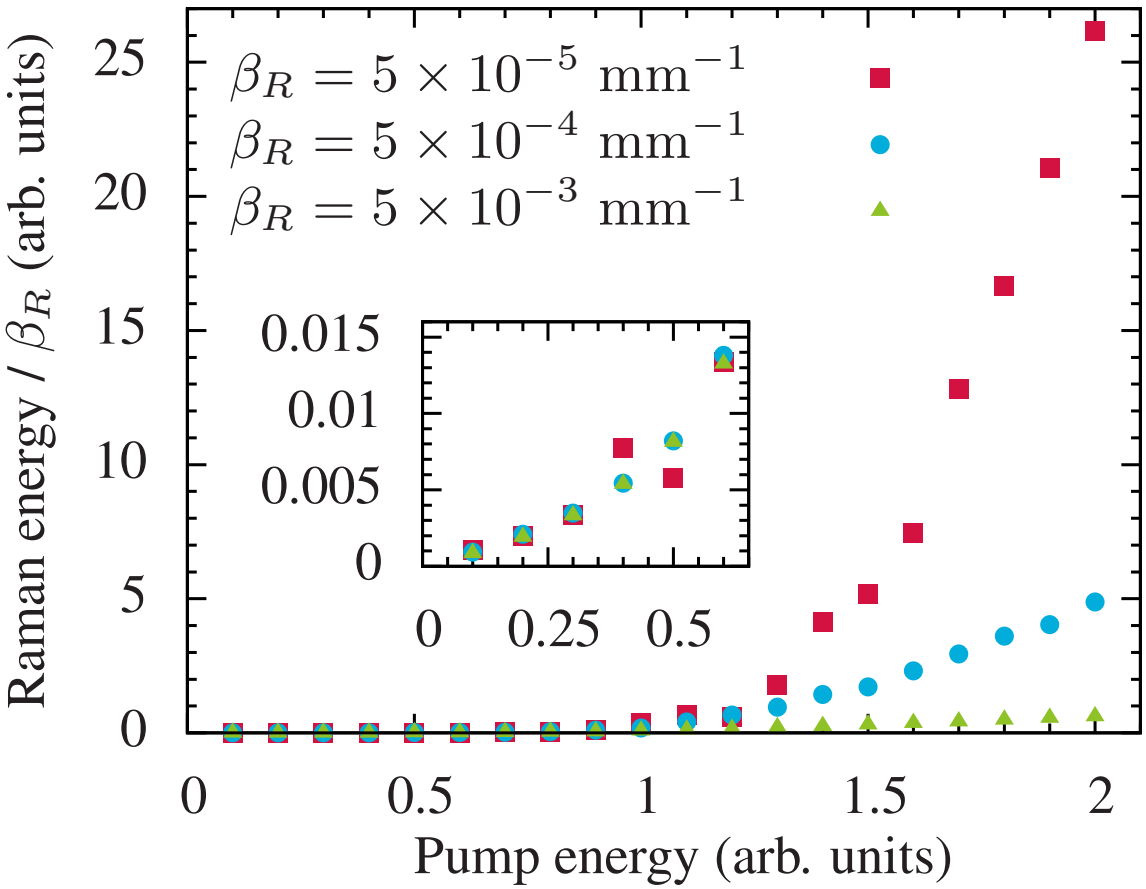

Figure 5.4: SRS generation with various spontaneous Raman coefficients showing that in the limit of no SRS this trivially results in a constant multiplicative factor, but in the high intensity regime the dynamics are far more complicated.

a global time step the motion of a single photon packet does not substantially change the photon densities needed to calculate the nonlinear probabilities. To ensure this is the case, we simply require $(c/n)\Delta t \leq d$, where in this case n is taken to be the smallest index of refraction of all the layers.

To generate the random numbers for our implementation, a Hybrid Tausworthe generator was used [19]. This generator has the advantage of being faster and requiring less memory than a Mersenne twister method [113] while still providing a period greater than 10^{36}. To generate these numbers in parallel each photon packet is assigned its own set of 4 initial seeds generated using the built in random number generator which is itself seeded with the current time, ensuring each run is independent of the last.

In the current NLMC code, only SRS is considered, however, the concept of introducing intensity dependent coefficients by way of computing the photon density is not limited to just these effects. This idea can be generalized in a straight forward manner to handle other nonlinear effects like absorption saturation, second and third harmonic generation, coherent anti-Stokes Raman scattering (CARS) etc. Additionally, higher order Stokes and anti-Stokes processes can be treated by allowing Stokes photons to undergo additional Stokes processes [114].

In the treatment here we have assumed that each wavelength propagates through the simulation using the same optical properties. Wavelength dependent properties could easily be implemented by defining a new set of optical properties for each type of photon and keeping track of this throughout the simulation.

It is important to note that while this technique shows excellent agreement with experimental data it neglects the wave nature of light. All phase matching conditions are automatically satisfied for SRS. Thus, it is not a coherent wave mixing phenomena but is more closely related to stimulated emission where the newly created photon's

phase depends only on the phase of the stimulating photon and not on the phase of the pump photon. However, the generated intensity does not depend on the phase of the stimulating photon. In other words, the process has the same probability of occurring regardless of this phase.

5.4 Conclusion

Currently there are no methods capable of accounting for the wave effects of light propagation in turbid media in the presence of nonlinear optical effects. However, for very simple systems, finite difference time domain (FDTD) [115] methods might be possible, but this approach is ultimately limited by the requirement that the location of each scattering particle must be known. Additionally, the possibility of extending the probabilistic approach of describing SRS employed here to electric field Monte Carlo (EMC) simulations [116–118] exists, but such methods still treat light as local particles with definite direction instead of waves which do not have a well defined direction, thus it is unclear at this moment if this will allow significant gain to warrant the increased complexity.

Here we have presented a method for including nonlinear effects into Monte Carlo simulations, specifically SRS. The ability to include these effects in Monte Carlo simulations will allow for a better understanding of the nonlinear dynamics of light in a turbid media, advancing fields such as nonlinear microscopy of biological tissues and increasing our understanding of new fundamental effects such as random Raman lasing.

6. CASCADED PROCESSES IN RANDOM RAMAN LASING*

6.1 Introduction

Random lasing has been a topic of considerable interest for nearly two decades [2, 29, 30, 33, 42, 82, 119]. Much of this interest is centered around the opportunity to study phenomena which are typically weak in a traditional scattering medium that has losses instead of gain. The effects being investigated include coherent backscattering, also known as weak localization [1, 69, 120], and Anderson localization of light, also referred to as strong localization [3, 121–124]. These processes are studied in random lasing media due to the presence of gain. Gain acts to preferentially amplify long path length photons, those most likely to be affected by localization processes, instead of absorption which attenuates these very photons which you wish to study.

The recent discovery of random Raman lasing has opened up a new regime in which to study light propagation in turbid media [65, 86]. Random Raman lasing offers several potential advantages over traditional random lasing for the study of these effects. First, random Raman lasers can be pumped with much more intense laser pulses because the medium, typically barium sulfate ($BaSO_4$), has extremely small linear and multi-photon absorption. This is difficult to accomplish in traditional random lasing because the medium must be able to absorb the pump wavelength. Fundamentally, stimulated emission, the gain mechanism in traditional random lasing, requires the physical absorption of photons followed by re-emission some time later, while stimulated Raman scattering (SRS) operates on virtual transitions and is essentially instantaneous. This fundamental difference in the processes leads to less

*Reprinted with permission from "Higher order processes in random Raman lasing" by B. H. Hokr, J. N. Bixler, and V. V. Yakovlev, 2014, Appl. Phys. A, **117**, 681-685, Copyright 2014 by Springer-Verlag Berlin Heidelberg

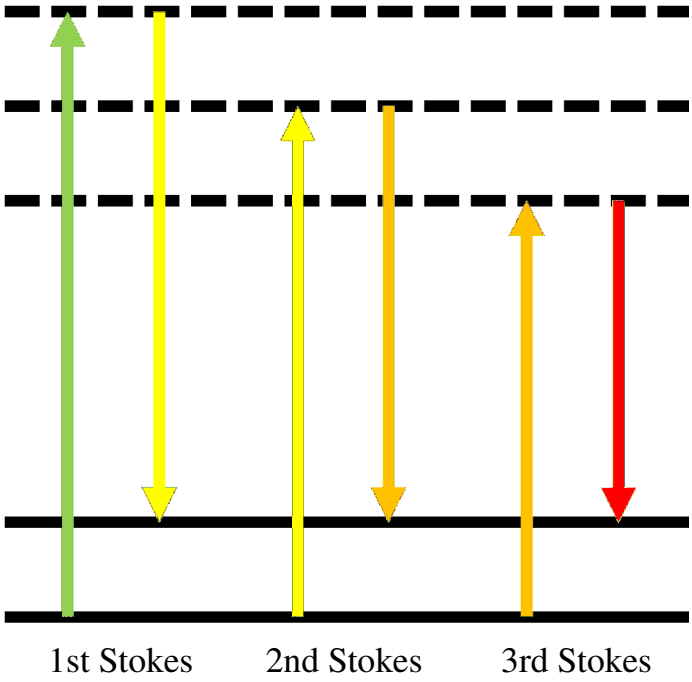

Figure 6.1: Conceptual drawing of higher-order SRS processes where the Stokes generations undergo SRS processes themselves. Each order of the process gives the output light an additional frequency shift equal to the energy of the vibrational transition.

heat being generated in the medium and allows much more powerful laser sources to be used without damaging the lasing medium. The more intense pump laser pulses used in random Raman lasing support tremendous gain, allowing for the generation of a very bright emission [45]. Second, the gain in random Raman lasing is fundamentally different than traditional random lasing. Because SRS does not involve the actual absorption of a photon the process cannot store energy unlike stimulated emission, which stores the pump photons energy until a stimulated emission process occurs or the molecule spontaneous relaxes. This transient nature of the gain manifests itself in the gain being proportional to the local intensity of the pump field. Additionally, random Raman lasing gives us an opportunity to study nonlinear optical effects in a turbid media. A better knowledge of these dynamics will help improve upon applications ranging from chemical analysis in turbid media [25, 104, 125] to stimulated Raman induced photoacoustics [75, 126, 127].

One of the most striking properties of the random Raman lasing emission previously reported is the presence of higher order SRS processes [45, 86]. These processes are the result of the Stokes shifted field undergoing an additional SRS processes, and picking up an additional Stokes shift. This is illustrated schematically in Fig. 6.1, and the experimental data is reproduced in Fig. 6.2. These higher order emissions require both a large gain and a long pathlength in the medium to develop, thus they are a natural place to investigate for the role of localization type effects in random Raman lasers.

In order to study the effects of localization, we first must understand how these higher order processes could develop in the absence of wave effects such as localization. Monte Carlo simulations treat light as a pure particle, thus they are not sensitive to wave effects that are responsible for localization. In other words, Monte Carlo simulations provide us with a view of what the emission from the random

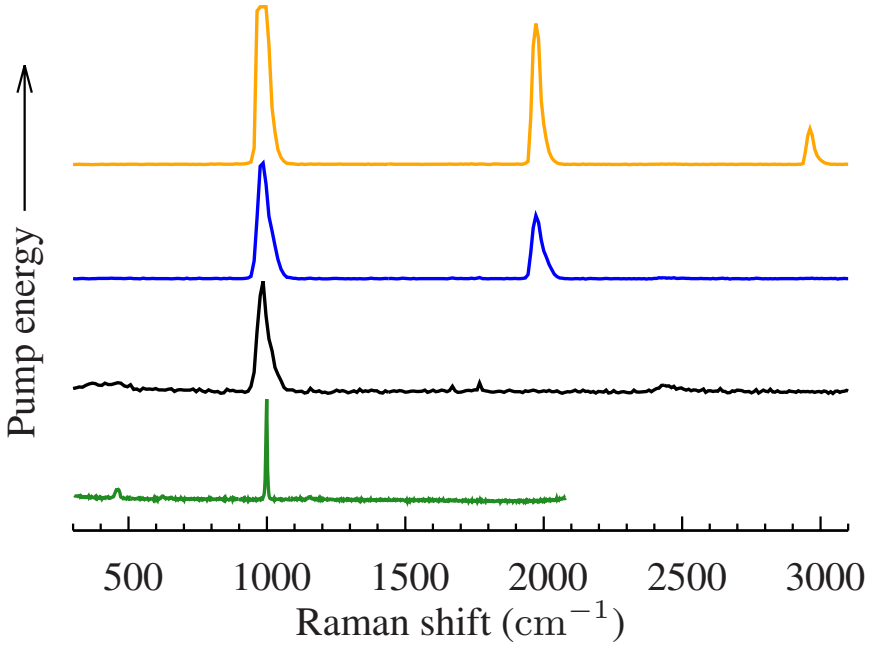

Figure 6.2: Experimental data showing the clear presence of higher order Stokes modes.

Raman lasing would look like in the complete absence of localization. This picture will allow us to compare these results to future experimental results, and enable us to conclude whether or not wave propagation effects play an important role in the dynamics of random Raman lasing.

Here, we present Monte Carlo results which study some of the most striking features of the higher order Stokes processes which have been observed in random Raman lasing [114]. We first study the threshold behavior of these higher order modes and then move forward to discuss the temporal behavior of these dynamics in the absence of wave propagation effects. This data will allow us to better study wave propagation effects in random Raman lasing by elucidating which effects can be explained by ordinary transport equation dynamics and which effects require wave propagation to be fully described.

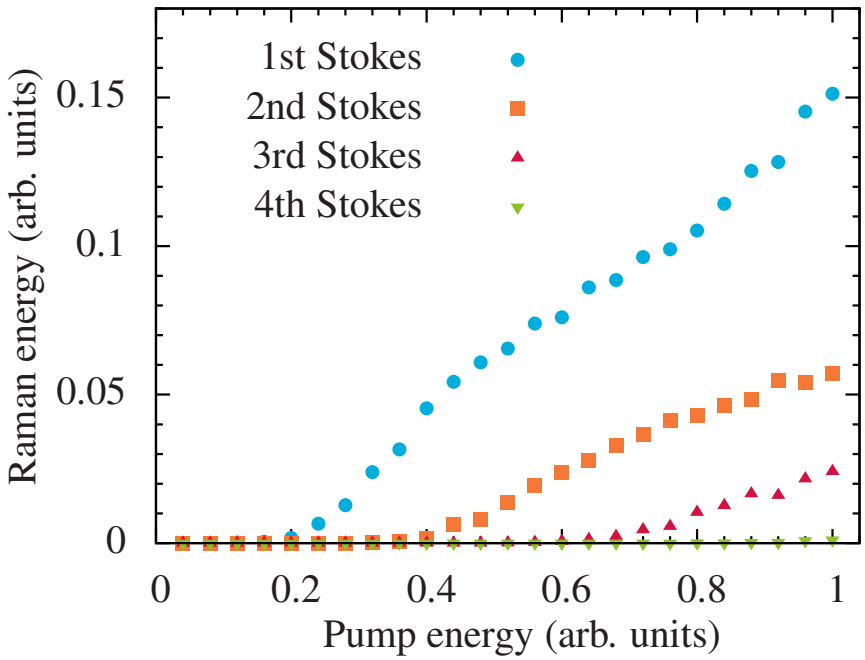

Figure 6.3: Monte Carlo simulations showing the threshold like behavior of each of the Stokes lines.

6.2 Methods and Results

To model the behavior of the higher order processes, we employ the nonlinear Monte Carlo (NLMC) simulation developed previously [15, 114]. To summarize the method here, elastic scattering is treated by assigning a random distance to the next elastic scattering event, given by the distribution

$$\rho(d) = \mu_s e^{-\mu_s d} \tag{6.1}$$

where μ_s is the scattering coefficient and d is the distance traveled by the photon. Once a scattering event occurs, the scattering angle is given by the Henyey-Greenstein distribution function in terms of the anisotropy, $g = \langle \cos(\theta) \rangle$, and a uniform random

number, ξ, between 0 and 1

$$\cos(\theta) = \frac{1}{2g}\left[1 + g^2 - \left(\frac{1-g^2}{1-g+2g\xi}\right)^2\right]. \tag{6.2}$$

Absorption is treated by assigning each photon to start with a weight of unity. After each step its new weight is given in terms of the absorption coefficient, μ_a, the distance traveled in that step, d, and the index of refraction of the medium, n, by

$$w' = e^{\mu_s(d/n)}w. \tag{6.3}$$

Each step, photons are given a probability of undergoing spontaneous Raman scattering given by,

$$P_R = 1 - e^{\beta_R(d/n)}. \tag{6.4}$$

Here, β_R is a measure of the strength of the Raman transition. Due to computational restraints, this parameter must be taken to be artificially large. However, over a reasonable parameter space this has not been seen to cause large deviations in the behavior of the model outside of an overall multiplicative constant in the strength of the signal. Additionally, comparison with experimental results confirm that the parameters here are in good agreement. When a photon Raman scatters it is converted from one photon type (pump, 1st Stokes, 2nd Stokes, etc.) to the next Stokes line. To include SRS in the simulation, the photon densities of each type of photon are calculated using a binning method. Once this is done the probability of a photon undergoing SRS is given by,

$$P_{\mathrm{SRS}} = 1 - e^{\beta_{\mathrm{SRS}}\rho_R(d/n)} \tag{6.5}$$

where ρ_R is the photon density of the Stokes mode that the photon will scatter into if this "coin flip" is successful, and β_{SRS} is a measure of the strength of the SRS process.

To model random Raman lasing, we chose the parameters which give the best fit to the available experimental data [114]. The sample was set to be 5 mm thick and 6 mm in the transverse directions. No photons in any of the simulations were able to penetrate through the sample, thus it can be treated as semi-infinite. Photon packets encountering the side boundaries of the sample were terminated at the surface. While this is a potential source of error, the few photons which do penetrate this far are extremely unlikely to undergo stimulated processes because the photon density is so small in this region. Thus, we can safely conclude that any error incurred by this finite transverse sample approximation will be very small compared to the stimulated contribution of the effects which we are interested in. The index of refraction was set to $n = 1.6$ to correspond to the index of refraction of $BaSO_4$. The medium was given an anisotropy factor of $g = 0.6$, a scattering coefficient of $\mu_s = 200$ mm^{-1}, an aborption coefficient of $\mu_a = 0.1$ mm^{-1}, a spontaneous Raman coefficient of $\beta_R = 5 \times 10^{-4}$ mm^{-1}, and a stimulated Raman coefficient of $\beta_{\text{SRS}} = 1.5 \times 10^{-5}$ mm^2. The spontaneous Raman coefficient and the stimulated Raman coefficient govern the strength of their respective process in the Monte Carlo simulations, and are defined and related to physical constants in previous work [114]. The global time step of the simulation was set to 0.1 ps and the bin size was set to 20 μm. A single incident pump pulse was used in all the simulations, however the strength of this pulse was varied. The pump pulse was Gaussian in space and time, with a full-width at half-maximum pulse length of 50 ps and a $1/e^2$ beam diameter of 1 mm. In all cases the collected signal is all the photons of a particular type that exit the sample in a reflection geometry. For every set of parameters the Monte Carlo simulations were

averaged over 10 runs, each using a different initial seed for the random number generator.

The threshold behavior of the different Stokes lines is shown in Fig. 6.3. For these runs, all the parameters descibed above were held constant and the number of photon packets making up the pump pulse were varied from 20,000 to 500,000 in increments of 20,000. This is akin to varying the pulse energy of the pump pulse. It should be noted that while the 4th Stokes signal is small, it is nonzero and beginning to undergo stimulated processes for the largest pump power used. One of the more surprising features of this is just how efficiently the 1st Stokes photons can be converted to these higher order modes. At the largest pump power used, 24% of the pump photons were converted to Raman photons of some kind. Of these, nearly 1 in 3 were converted into higher order Stokes modes.

The temporal dynamics of these processes are shown in Fig. 6.4. These are expected to be paramount to understanding the role of wave effects in random Raman lasing because localization effects will lengthen the amount of time that photons will stay in the medium. One of the interesting features that can be seen is the delay between the pump signal and the 1st Stokes, and between the 1st Stokes and 2nd Stokes and so on. It is readily seen that this delay decreases as the pump intensity is increased. The most likely reason for this is that at high pump intensities, the threshold for SRS processes occurs before the peak of the pulse. Thus, the stronger the pump pulse, the earlier that the system crosses this threshold. For sufficiently intense pump pulses, pump depletion effects can start to be seen in the scattered pump signal, and even in the 1st Stokes signal at a high enough intensity.

Furthermore, the total decay time of the pump pulse and Stokes modes does not vary significantly over the range of scattering coefficients that are reasonable for a highly scattering powder (30 mm^{-1} to 1000 mm^{-1}). In Fig. 6.5 it is readily visible

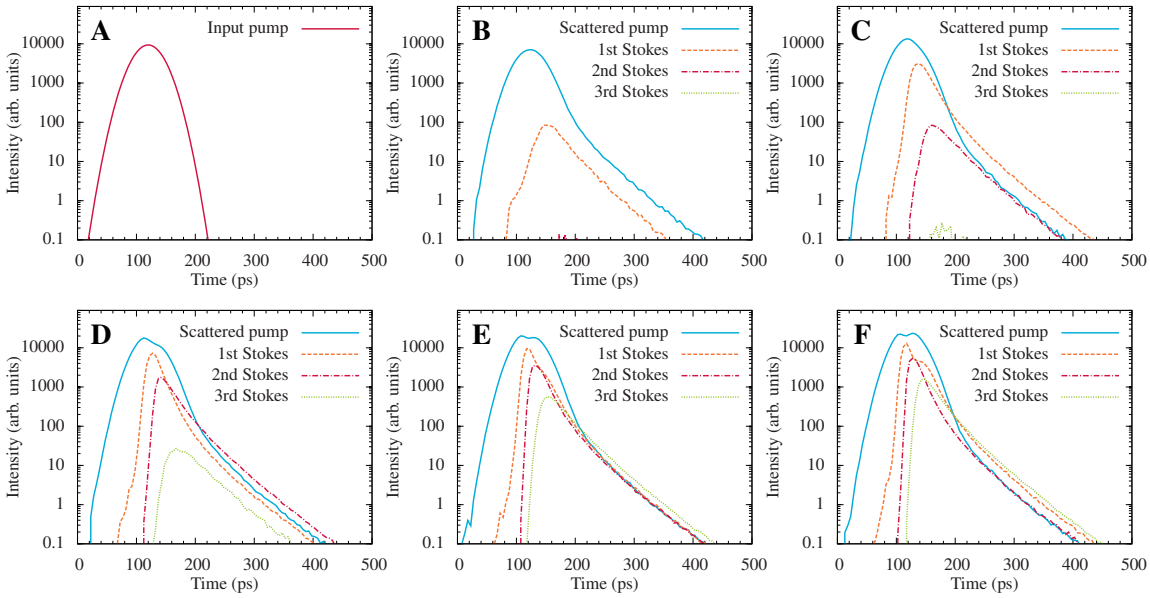

Figure 6.4: (A) Temporal distribution of the input pump pulse used in the Monte Carlo simulations. Note that the vertical scale for this is arbitrary as it depends on the strength of the input pump used. (B-F) Temporal dependence of the various Stokes lines as well as the residual pump for different strength pumps in a reflection geometry. All five plots are plotted using the same vertical scale, thus are comparable. The input pump strengths are as follows: (B) 100,000 photon packets, (C) 200,000 photon packets, (D) 300,000 photon packets, (E) 400,000 photon packets, and (F) 500,000 photon packets.

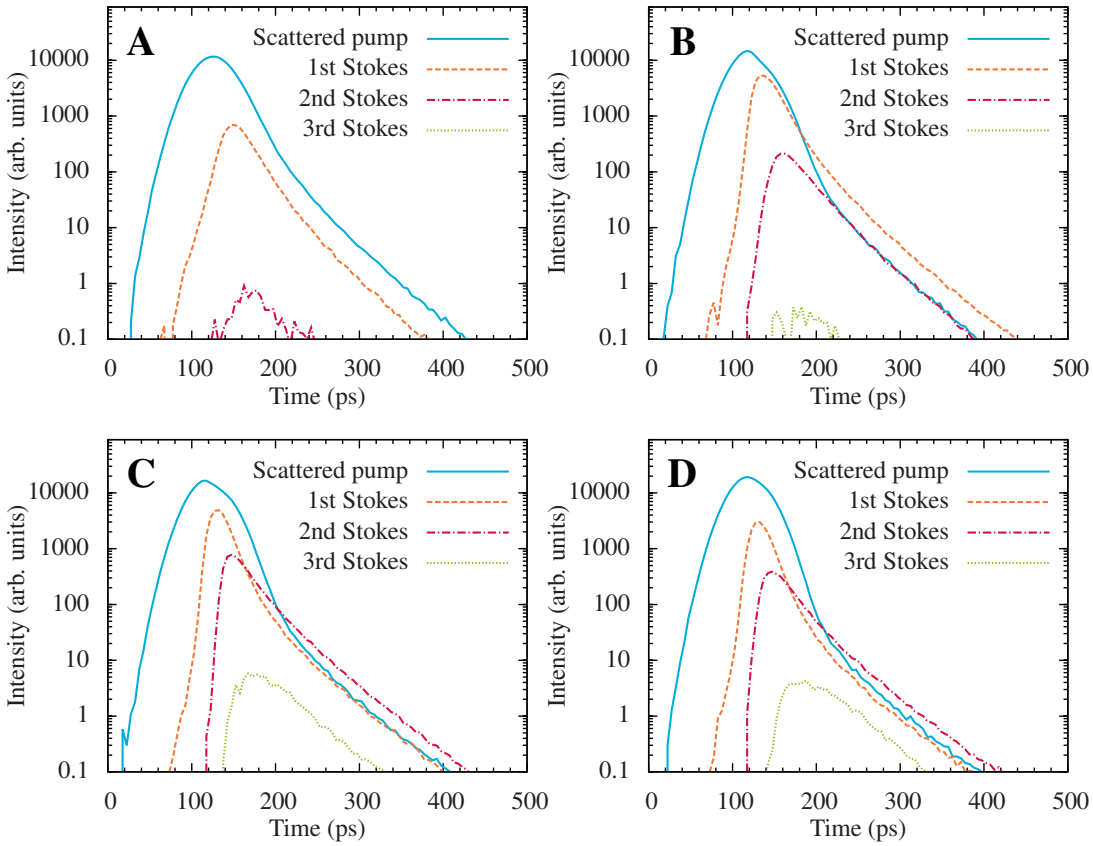

Figure 6.5: Temporal dependence of the scattered pump and the various Stokes orders for various scattering coefficients. (A) $\mu_s = 30$ mm^{-1}, (B) $\mu_s = 100$ mm^{-1}, (C) $\mu_s = 300$ mm^{-1}, (D) $\mu_s = 1000$ mm^{-1}. 250,000 pump photon packets were simulated for each run and all other parameters are those used in all the other simulations.

that increases in scattering lead to increased efficiency of random Raman lasing. This is a result of the lower scattering media allowing the photons to more easily diffuse throughout, lowering the photon densities, and reducing the SRS gain.

6.3 Discussion

Typically higher order SRS processes are only observed in systems such as propagating high intensity pulses down a fiber or when high intensity femtosecond pulses are used in a Raman crystal [128]. The presence of these higher order modes in ran-

dom Raman lasing using an unfocused 50 ps pulse is quite surprising. Furthermore, the generation of each line is surprisingly efficient, even in the absence of localization effects. In the presence of localization effects, it is logical to expect the generation of these higher order modes to be even more efficient, due to the longer interaction paths.

While an analytical approach to describing the dynamics of a 3D random Raman laser would be completely intractable, Monte Carlo simulations offer a good opportunity to understand how these dynamics fit into those associated with particle like transport equations dynamics. Such an understanding will be necessary in the search for definitive proof that optical Anderson localization can exist in a bulk 3D system. By comparing these results with future experiments, we will be able to search for deviations from transport theory that would signify the presence of wave propagation effects. Additionally, we will be able to distinguish the difference between localization effects and absorption, which has been an issue in previous searches for localization [121].

6.4 Conclusion

The presence of higher-order, cascaded stimulated Raman scattering effects has been confirmed in random Raman lasing. The presence of these highly nonlinear effects points to the tremendous gain present in random Raman lasing systems. This seemingly oversized gain hints at the presence of high-Q modes, potentially due to localization dynamics, ultimately contributing to this incredible gain. Further work is certainly required to confirm or deny the presence of these exotic modes, but in either case the presence of these higher-order effects indicates that there is still a great deal to learn about the dynamics random Raman lasing.

7. THE POSSIBILITY OF ANDERSON LOCALIZATION IN RANDOM RAMAN LASING

7.1 Introduction

Lasers are promising to revolutionize lighting technology, with laser headlights already appearing in production automobiles. For some of these applications, the coherence of a laser is a significant hindrance. One potential class of lasers that can overcome this is random lasers [27]. Their highly multi-mode emission gives their emission properties more like a classical light bulb or a light emitting diode (LED), yet they exhibit laser-like brightness due to the presence of exponential gain [42]. In addition to promising applications, random lasers push our understanding of the physics of wave propagation. The complex intertwining between multiple scattering and nonlinear gain provide a seemingly ideal platform to study fundamental wave propagation processes, such as Anderson localization [129], but accepted examples of Anderson localization, in the optical domain, in 3-dimensional systems remain elusive.

Anderson localization, which was discovered by Anderson in 1958 [130], is of great interest in solid-state physics. He demonstrated that the wave-packet of an electron can be absent of diffusion in a disordered medium [131]. Elucidating the underlying physics in a medium with strong disorder provides insight on the transport of particles, including electrons and photons. Recently, Anderson localization of light in photonic lattices with disorder has drawn considerable interest [3,124]. Due to the imperfections in optical media, it is impossible to disregard disorder in any optical system. Thus, the performance of systems with strong disorder is of great importance for known optical phenomena. For example, random nano-lasing has been studied in

the Anderson localized regime [129]. However, there has not been any research into the effect of Anderson localization on random Raman lasing.

Random Raman lasing [85,86], random lasing which uses stimulated Raman scattering as the gain mechanism, is emerging as an interesting platform to study wavelike phenomena. Fundamentally, the advantage of random Raman lasing, compared to traditional random lasers based on stimulated emission, is the low absorption of the pump radiation. This allows the pump to penetrate a much larger volume than stimulated emission lasing, where strong pump absorption is required to obtain a population inversion. In addition to low absorption at the pump wavelength, random Raman lasers have virtually no absorption at the emission wavelength, allowing the lasing emission to propagate very long paths without attenuation. On the other hand, traditional lasing requires non-zero absorption for the emission wavelengths because detailed balance guarantees that stimulated emission and absorption share the same coefficient. Ultimately, this means that propagation in regions where the pump was unable to generate a population inversion suffers significant losses due to absorption. In addition to significantly reducing the losses for extended, or long pathlength modes, the low absorption possible in random Raman lasing systems allows for very intense pump pulses to be used without damage to the powdered sample, leading to an extremely bright emission which is attractive as a light source [45,132].

Here, we present several pieces evidence that point to a deviation from classical radiation transport, each of which is consistent with effects expected from the presence of extended modes and Anderson localization. First, non-linear Monte Carlo simulations have provided useful insights into the dynamics of random Raman lasing [17, 114], and have been able to reproduce all experimental features quite well with one exception. They fail to predict the very long temporal life-time of the Raman emission. Second, random Raman lasing emission has been shown to be highly

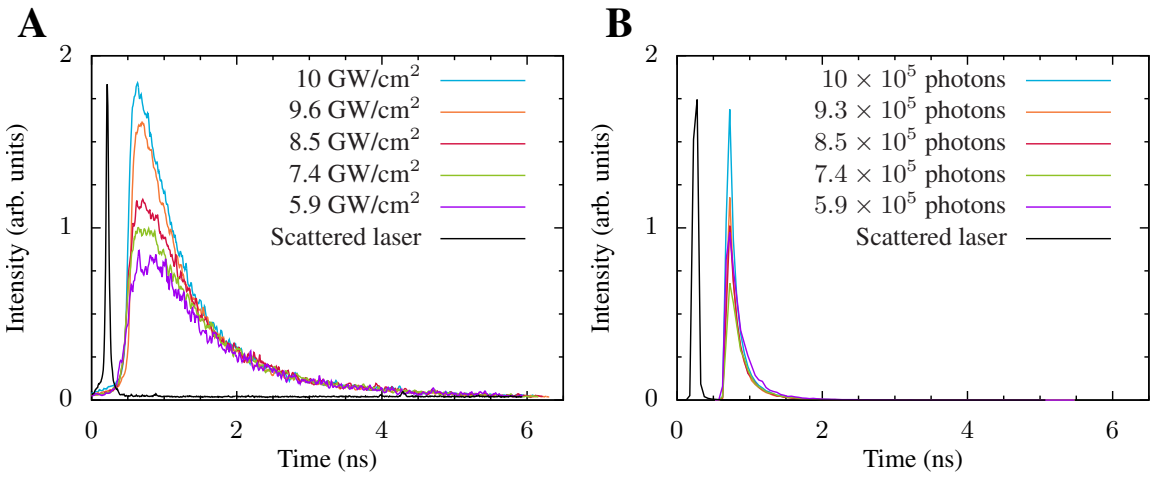

Figure 7.1: The temporal profile of the random Raman laser emission versus pump energy. (A) is the experimental data and (B) is the results of non-linear Monte Carlo simulations. The elastically scattered pump is shown for reference. Each trace has been normalized so that the exponential tails overlap by fitting an exponential decay and dividing each trace by the normalization coefficient. The exponential decay appears independent of pump power.

multi-mode [132], consisting of hundreds of lasing modes, while results from more rigorous theoretical calculations predicts at most a few modes are possible. This hints at multiple, essentially independent random Raman lasers are operating simultaneously, which again, points to extended, localized modes playing a role in the dynamics. Finally, from measurements on the speckle contrast of the emission, it is seen that a seemingly unique speckle pattern is formed with each random Raman laser pulse. This is in contrast to how a typical laser operates where its modes are quite coupled, even in the case of random lasers [33]. With random Raman lasers, it seems that there exist many independent modes that each acquire their own unique phase with each laser pulse, leading to the formation of a new speckle pattern. It is important to fully disclose that none of these constitute direct evidence of Anderson localization, but each of them contradicts with the current theory and are all consistent once the effects of Anderson localization are considered.

7.2 Results

Barium sulfate ($BaSO_4$) was used as the active Raman medium and the source of scattering in the random Raman laser. The powder was lightly packed into a 1 cm diameter, 1 cm deep cylindrical container with the top open so that the laser never interacts with the sample container. This powder has a transport path length of 1.19 ± 0.03 μm which was measured using the coherent backscattering technique [133]. Given this very short transport path length we are likely in the strong localization regime.

A streak camera (C1587; Hamamatsu) with a fast streak card (M1952; Hamamatsu) capable of 2 ps temporal resolution was used to measure the temporal dynamics of the random Raman laser emission. The results are shown in Fig. 7.1. They demonstrate that significant levels of Raman light remains present in the cavity several nanoseconds after the pump pulse. This is in contrast to non-linear Monte Carlo simulations [17, 114] which predict a significantly shorter emission. The parameters used in these simulations correspond to experimental data as much as possible and are an index of refraction, $n = 1.636$, a scattering coefficient, $\mu_s = 2132.5$ mm^{-1}, an anisotropy parameter, $g = 0.7428$, an absorption coefficient, $\mu_a = 0.01$ mm^{-1} [134], a spontaneous Raman coefficient, $\beta_R = 2 \times 10^{-4}$, and a stimulated Raman coefficient, $\beta_{\mathrm{SRS}} = 10^{-6}$. The anisotropy and scattering coefficients used were computed using Mie scattering theory for a 1 μm sphere of $BaSO_4$ and are in reasonable agreement with those measured. For comparison, these values produce a transport path length of 1.82 μm. The computed values were used because the simulation requires the scattering coefficient and the anisotropy coefficient separately. These parameters are further defined and the simulations discussed in greater detail in a previous paper [17]. It is important to point out that the Monte Carlo simulations should

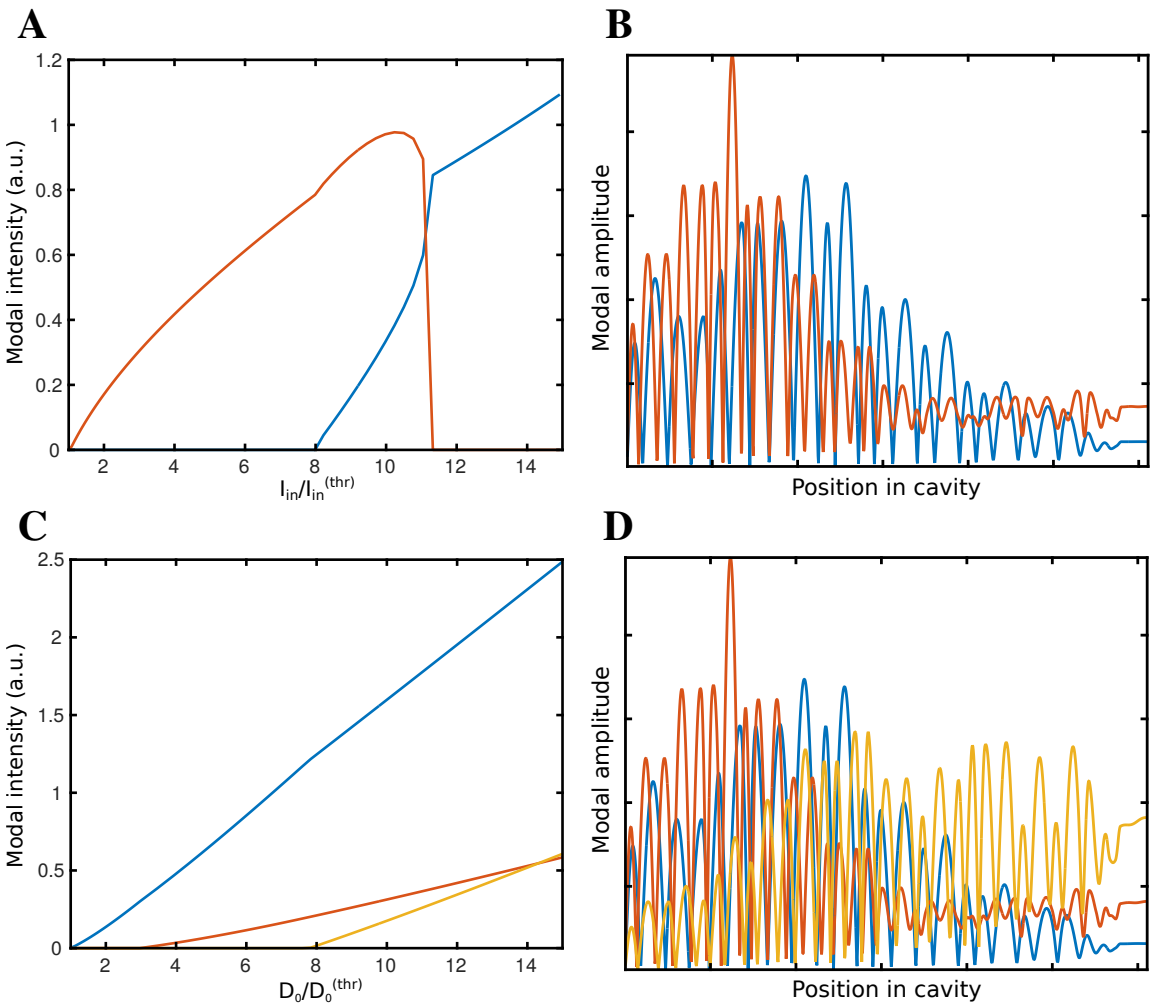

Figure 7.2: $L \approx 20\lambda_a$, $\lambda_a = \frac{2\pi}{40}$, the layers of the random cavity are $n = 1$, $n = 1.6$ (chosen due to n for barium sulfate), with 40 layers in total of different widths. Gain bandwidth = 4 (units of L/c). the Raman cavity is illuminated from right side. Both cavities have mirror on their left edge. Both cavities have uniformly distributed gain atoms.

account for all the relevant physical dynamics with the exception of any which arise due to the wave nature of light.

The steady-state ab initio laser theory (SALT) was designed to provide an exact treatment of the open cavity boundaries and spatially varying gain competition [135–138]. It yields a set of coupled differential equations in the frequency domain which can be efficiently solved numerically. Unlike previous Raman laser theories, this new theory self-consistently determines both the number of lasing modes and their frequencies, thus naturally accounts for both multi-mode operation and line-pulling effects between the natural Stokes frequency and the passive cavity resonances of the laser cavity. Using this new theory, we can directly compare the multi-mode proclivities of Raman gain media against traditional gain media for the same exact cavity holding all other relevant parameters, such as the gain width, equal. The results of such a comparison can be seen in Figs. 7.2A and 7.2C, which show the modal intensities as a function of pump strength in a random, 1-dimensional cavity for both a Raman and atomic gain medium respectively. Here, we see that the Raman gain medium usually only has a single mode active for any given pump power, in contrast with the atomic gain medium which is able to achieve multi-mode operation for most input pump strengths. We can understand this through looking at the associated lasing mode profiles shown in Figs. 7.2B and 7.2D. For the Raman laser, as the pump power is increased, the high Q lasing mode deep within the random cavity is eventually out-competed by the second lasing mode, which is lower Q, but exists closer to the edge of the cavity, and as such depletes the pump photons to the point where it drives the first lasing mode below threshold, turning it off. While the modes in the atomic medium do compete for gain with one another, this competition is through spatial hole-burning, rather than pump field depletion, which is an effect specific to χ^3 type gain media and parametric processes. These early

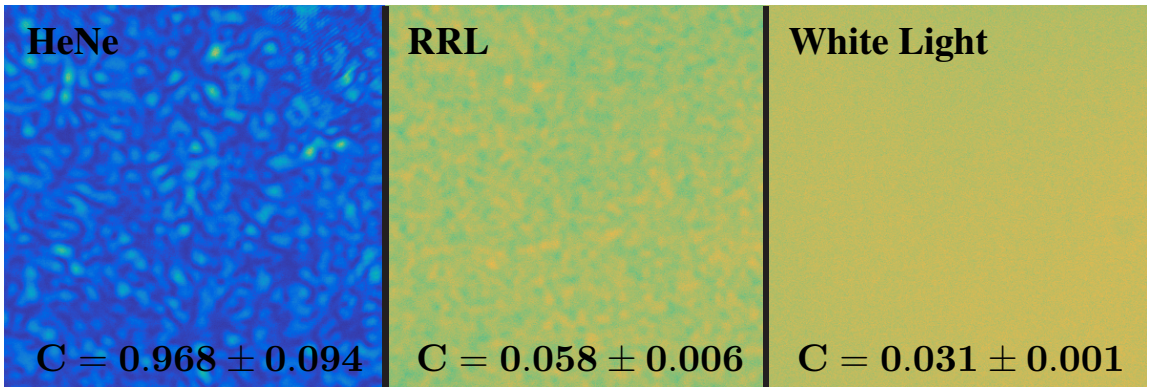

Figure 7.3: Speckle contrast of random Raman lasing. The speckle contrast measurements for a helium-neon laser and a halogen white light are shown for comparison and to illustrate the dynamic range of the measurement technique. This predicts 300 independent lasing modes present in the random Raman laser emission.

results indicate that within a single cavity, there can be at most a few simultaneous steady-state Raman lasing modes, many fewer than are possible with an atomic gain medium. Thus, to increase the multi-mode behaviour of Raman lasers, one must simultaneously pump a large number of effective cavities, in which each cavity exists only a few highly localized modes, which do not compete for gain with other neighbouring effective cavities.

To assess the number of lasing modes present in the random Raman laser, the speckle contrast was measured [139]. The speckle contrast is defined to be

$$C = \frac{\sigma}{\langle I \rangle} = \frac{1}{\sqrt{m}} \tag{7.1}$$

where $\langle I \rangle$ is the average value of the intensity, σ is the standard deviation, and m is the number of independent modes present. Using these definitions, we find that there are 300 independent lasing modes present in the emission. This well exceeds the predictions of only a few simultaneous lasing modes in the theory presented above.

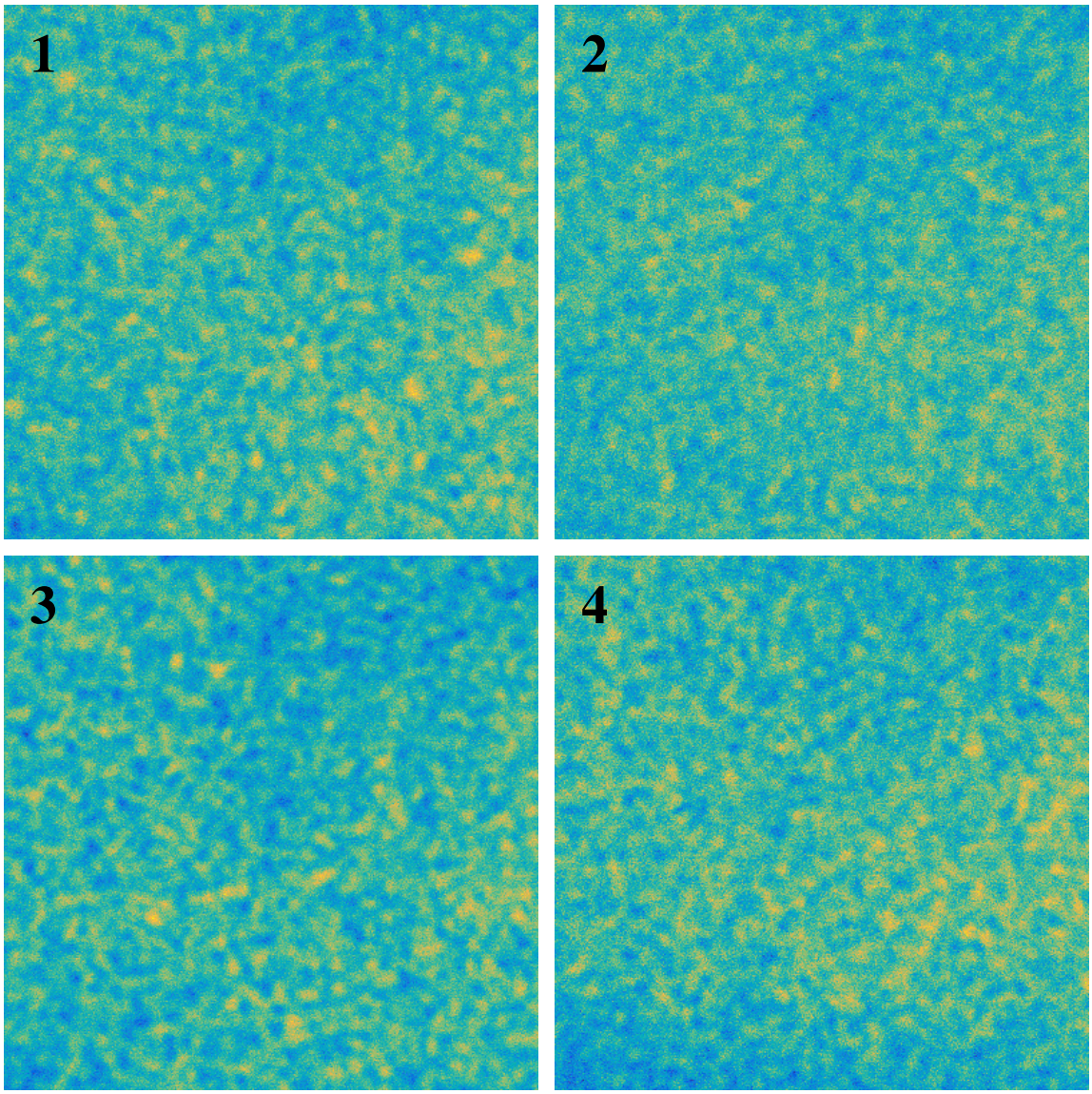

Figure 7.4: The speckle patterns emitted by four consecutive pulses from the random Raman laser. The image has been scaled to maximize the contrast of the speckle grains. The fact that each image is a unique speckle pattern hints that each laser mode gets an independent phase with each shot. This would not be the case if there was even weak coupling between the modes as in a traditional random laser.

To measure the speckle contrast, the light is coupled into a 2 m long 600 μm fiber. The light from the fiber is left uncollimated and was allowed to overfill the array of a 16-bit CCD (Orca-ER; Hamamatsu). The CCD was placed far enough from the fiber that the speckle grain size is significantly larger than the pixel size of the CCD. To demonstrate the dynamic range of the measurement technique, a helium neon laser was used as a highly coherent source, and a halogen light as a low-coherence source. The resulting images and speckle contrast are shown in Fig. 7.3. The speckle contrast was measured by selecting a 400x400 region of the CCD that was clear of debris. That region was further subdivided into 25 80x80 sub-regions. The speckle contrast of each sub region was computed independently by first subtracting a pedestal, to reduce the effect of the CCD dark counts on the calculation, and then computing the mean and standard deviation [140, 141]. This helps minimize any effects due to non-uniform illumination of the array. Multiple images were taken with each light source, and those used in the calculations for the random Raman lasing and halogen light source were selected by rejecting any images with saturated pixels and requiring the average counts per pixel to be greater than 20,000. This minimizes the effect of noise due to the CCD while ensuring that saturation is not occurring. For the Helium-Neon (HeNe) images, the requirement on average pixel count was not enforced due to the high contrast, but the laser power was adjusted to maximize the dynamic range of the detector without saturation. At the end, 21 images were used for the HeNe calculations, 28 images for the random Raman lasing emission, and 101 images for the white light. All of the sub regions from all of the images were first pooled together into a single data set and then averaged. The standard deviation of these calculations were used as the error.

Finally, the last effect discovered thus far that points towards localization in random Raman lasing again comes from the speckle pattern. On each sequential

laser pulse a seemingly unique speckle pattern forms in the emission. This effect is displayed in Fig. 7.4 where 4 subsequent laser pulses are shown. This is not typical of random lasers which retain the same speckle patterns over repeated shots, until some other perturbation in the system takes over and results in a new speckle pattern. Typically, this occurs through the small but non-zero coupling between modes. This allows each mode to share the phase from the initial spontaneous photon that initiated the pulse, resulting in only a global phase shift from shot-to-shot which would not effect the speckle pattern. On the other hand, if localized modes were present that were independent of each other, each of these modes would require its own so called "magic photon" which would give each mode its own independent phase each shot, resulting in a unique speckle pattern with each shot. It is important to disclose that at this time, we cannot yet definitively rule out perturbative effects such as movement of the powder from shot to shot, but when presented in conjunction with the other evidence a strong, clear picture emerges.

7.3 Conclusion

There are several key measurements where random Raman lasing deviates from classical, particle-like, diffusion predictions, and while none of these measurements by itself constitutes the proverbial "smoking-gun" of Anderson localization, Anderson localization appears to be the only single effect that is known which is consistent with all of these measurements simultaneously. For this reason, we conclude that it appears highly likely that Anderson localization plays a key role in the dynamics of random Raman lasing, making it a fascinating platform to test our theoretical understanding of wave-like diffusion in non-linear systems.

8. REMOTE CHEMICAL IDENTIFICATION VIA RANDOM RAMAN LASING*

8.1 Introduction

The ability to remotely identify materials in real time has long been a scientific holy grail. The search for extraterrestrial life, the necessity to assess the source of climate change, and the growing need of agriculture further drive the interest in developing chemically specific stand-off identification of materials [142–147]. The remote identification of organic compounds would aid in the search for extraterrestrial life and assist in the detection and monitoring of biological weapons [148, 149]. The detection of nitrates at long distances would enable the detection of explosives from safe distances [150, 151]. Traditionally, optical remote detection schemes have relied on non-directional incoherent processes [143–146]. These methods lack efficiency, limiting the maximum effective distance of the technique, or requiring excessive integration times for chemically specific identification. More recent advances have employed white-light generation in filaments [147] or lasing processes in atmospheric gases [152–155] to generate backward-propagating radiation that can be used to drive coherent spectroscopic techniques, such as coherent anti-Stokes Raman scattering (CARS) [148, 156]. However, these approaches are only applicable to atmospheric sensing.

With only the human eye, it is very difficult to distinguish between a harmless white powder and one which can be used in the production of high-powered explosives (see Fig. 8.1). However, each of these chemicals possess a distinct vibrational

*Reprinted with permission from "Single-shot stand-off chemical identification of powders using random Raman lasing" by B. H. Hokr, J. N. Bixler, G. D. Noojin, R. J. Thomas, B. A. Rockwell, V. V. Yakovlev, and M. O. Scully, 2014, Proc. Natl. Acad. Sci, **111**, 12320-12324, Copyright 2014 by National Academy of Sciences, USA

spectrum, allowing for chemical identification via vibrational spectroscopy. Raman scattering, the inelastic scattering of light from a vibrational level of a molecule, has been used for decades as a tool for nondestructive, label-free, chemical analysis of samples [76]. It is a powerful analytical technique with one significant drawback; the signal generated is extremely weak. Only about 1 in 10^{10} photons that enter a sample undergo spontaneous Raman scattering. However, once the incident intensity reaches a certain threshold, the process of stimulated Raman scattering (SRS) takes place, leading to the exponential growth of the Raman signal [80, 81]. The discovery of random lasing [2, 33, 64] leads naturally to the question of whether or not it is possible to achieve SRS in a random medium and ultimately random Raman lasing.

It is commonly thought that strong light scattering acts like diffusion to spread out light as it travels through a turbid medium, making nonlinear optical effects extremely inefficient. However, if the incident beam has spatial dimensions exceeding the characteristic diffusion length of light, the photons can not quickly leave the excitation volume, and multiple scattering effects result in a substantial intensity buildup. This high-intensity region promotes stimulated Raman gain, which above a certain threshold, leads to random Raman lasing. Random Raman lasing is much more efficient than spontaneous Raman scattering, and conversion efficiencies of several percent have been experimentally observed [157]. Recent advancements in optical wavefront optimization brings hope that it might be possible to remotely control the intensity distribution inside a scattering medium [70, 158], opening up room for further improvements in the efficiencies of random Raman lasing.

Here, we report on the single-shot stand-off identification of closely related chemical species via SRS from a distance of 400 m [45]. When corrected for losses incurred by clipping losses and imperfect reflections this corresponds to an effective distance of more than a kilometer. The light generated via the random Raman lasing process

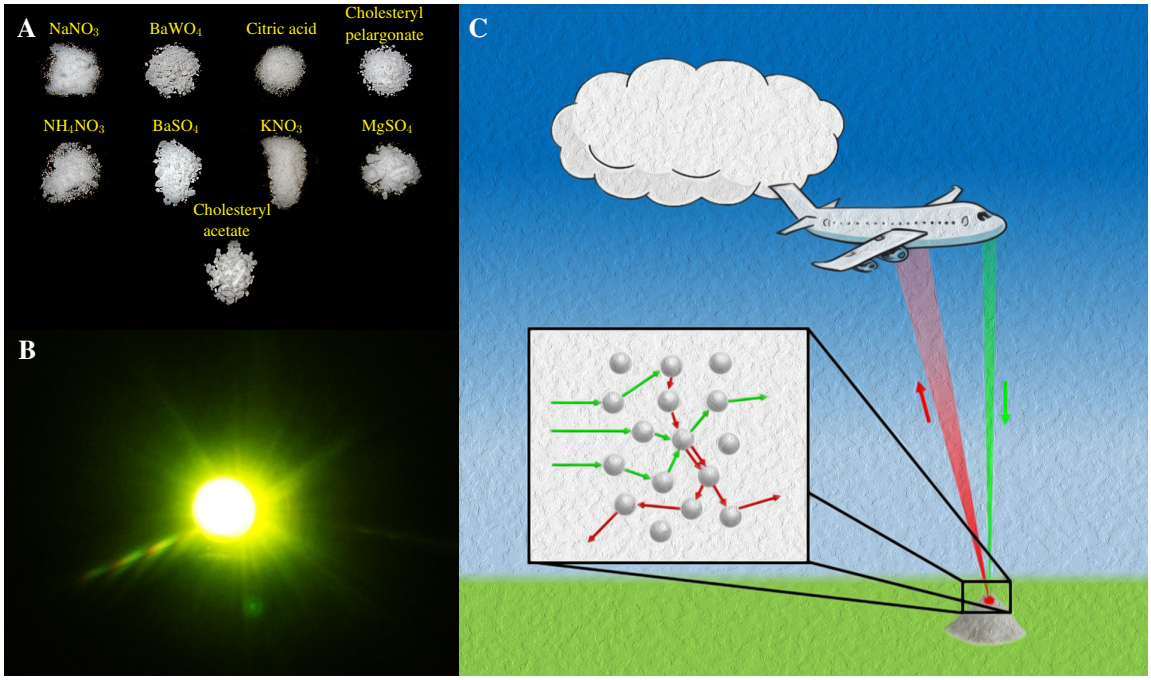

Figure 8.1: (A) A photograph of the various white powders where random Raman lasing has been observed. The "whiteness" of these powders depends on the illumination and the viewing angle, while SRS spectra provide excellent discrimination of these compounds in a single laser pulse. (B) A photograph of random Raman laser emission in $BaSO_4$ powder illustrating the brightness. (C) Conceptual drawing illustrating remote detection of white powders via random Raman lasing.

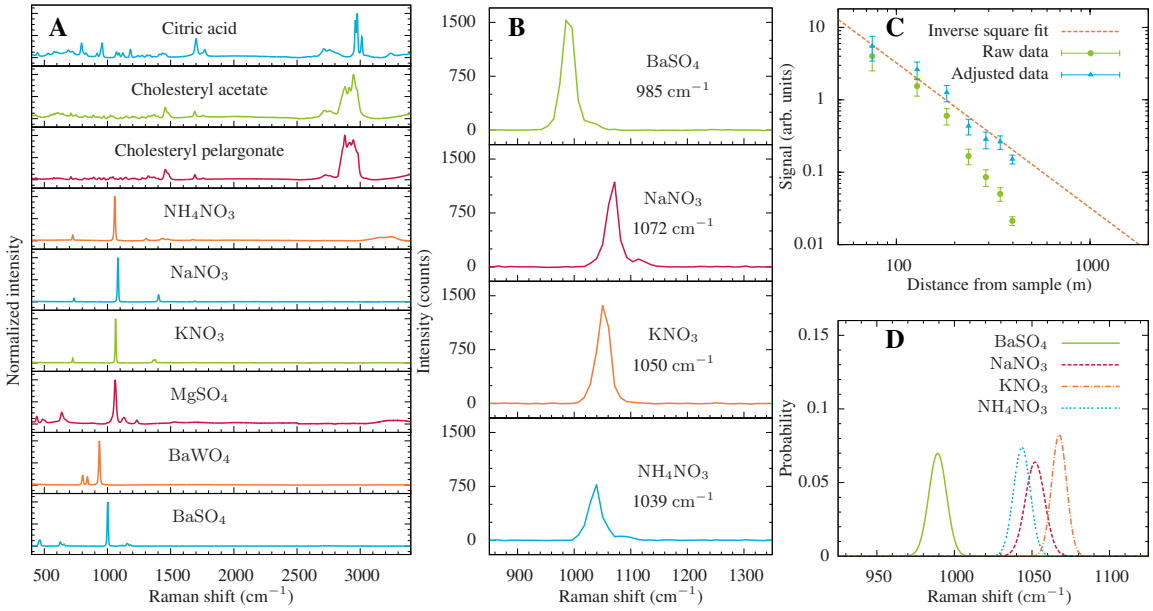

Figure 8.2: (A) Spontaneous Raman spectra of all of the chemicals where random Raman lasing has been observed. (B) Stimulated Raman spectra of similar chemicals taken at a distance of 400 m using a single laser pulse, illustrating that minute changes in the molecular makeup can be distinguished via SRS even with a relatively low resolution Ocean Optics USB2000 spectrometer with a spectral resolution of only 40 cm^{-1}. (C) The detected intensity from $BaSO_4$ as a function of distance from the sample the adjusted data is corrected for both mirror reflections and clipping losses. The error bars represent the standard deviation of the 50 shot data set taken at each distance. (D) Distribution of the peak value of the stimulated Raman spectra fit using Gaussian statistics, illustrating that nearly identical chemicals are still distinguishable.

is emitted isotropically due to multiple elastic scattering. It is demonstrated that this leads to a signal that is dependent on the inverse square of the distance from the sample. However, the random Raman lasing process produces a very bright emission (see Fig. 8.1). This ultra-bright signal makes long-distance, single-shot identification of materials possible. Additionally, we show that the random Raman lasing process is robust against the kind of wavefront degradation that can be introduced from atmospheric effects.

8.2 Results

Typical single-shot SRS spectra, taken at the maximum 400-m distance allowed by our setup, are shown for four chemically similar compounds in Fig. 8.2. The spectral resolution of the spectrometer available for those measurements (USB2000; Ocean Optics, Inc.) was limited by the 200 μm slit to be 40 cm^{-1}. These spectra illustrate two very important aspects of the proposed new approach: first, there is sufficient signal to allow the detection to be made at much longer distances, and second, similar chemical compounds can be identified using only the single Raman line that appears in SRS spectra. The latter point is somewhat masked by the poor spectral resolution of the spectrometer. However, a major motivation for this demonstration was to achieve robust remote chemical sensing using a very moderate budget. If a higher-resolution spectrometer with a more sensitive and less noisy array detector were used, 100% specificity of chemical identification would be possible at much greater distances. To demonstrate that it is possible to uniquely identify the chemicals based on only a single pixel difference, Fig. 8.2 shows the distribution of the wavenumbers corresponding to the maximum value of the SRS peak over many shots fit using Gaussian statistics. The spectral position of a Raman peak changes very little from shot to shot, i.e. less than the spectral resolution provided by a

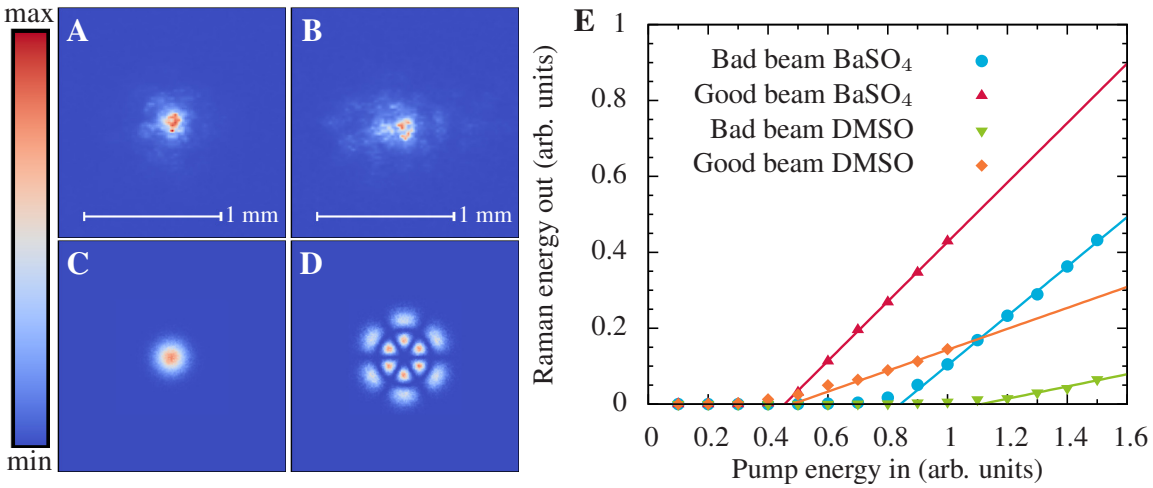

Figure 8.3: (A) Experimental beam profile of our laser at the surface of the sample, referred to as "good beam". (B) Experimental beam profile of our laser at the surface of the sample once a mask was placed in its path, referred to as "distorted beam". (C) Simulated Gaussian "good beam" used in the Monte Carlo simulations. (D) Simulated Laguerre-Gauss $TEM_{1,3}$ "distorted beam" used in the Monte Carlo simulations. (E) Efficiency plot generated by Monte Carlo simulations showing how beam quality affects the threshold dynamics of random Raman lasing compared to SRS in non-scattering environments.

single pixel on the spectrometer (about 11 cm^{-1} at these wavelengths). Thus, any variation in this peak value from shot to shot must be due to noise in the CCD, which is Gaussian in nature. By fitting the distribution of the SRS peaks to a Gaussian distribution, chemical identification can be obtained with a degree of confidence determined by the Welch t-test [159]. Due to their similar SRS spectra, the most difficult chemicals to distinguish were ammonium nitrate (NH_4NO_3) and sodium nitrate ($NaNO_3$); however, the spectra for these powders were statistically different with a two-tailed probability of 0.9999998. Thus, it is possible to distinguish very similar chemicals with a high degree of certainty even when the peaks differ by less than the resolution of the spectrometer by simply comparing the two distributions of the peak heights.

Due to the multiple elastic scattering dynamics present in the powder, the generated Raman light is emitted largely isotropically. This leads to an inverse square dependence of the signal on the distance from the sample. Using this and correcting for the losses incurred by mirror clipping and imperfect reflections in our setup, the signal level which we were able to detect at 400 m corresponds to a straight light distance of more than a kilometer.

Nonlinear processes are highly dependent on the local intensity of the light. In a non-scattering environment this leads to a strong dependence of the output intensity on the beam quality of the pump pulse. This presents a substantial problem when considering remote detection schemes where the pump beam must propagate over long distances. Not only do these long propagation distances make it difficult to form a tight focus due to the diffraction limit, but processes such as scintillation greatly degrade the beam quality over these distances. Scintillation is an effect caused by small variations in the refractive index due to small temperature fluctuations in the air, this leads to a time-dependent spatial modulation of the pump pulse. Thus, it is very important that a viable remote-sensing technique is relatively insensitive to beam quality fluctuations. To generate a "distorted beam" experimentally, the beam was passed through a metal mesh before it was focused onto the sample. In barium sulfate ($BaSO_4$) powder the "distorted beam" exhibited a 28% increase in the energy required to achieve random Raman lasing. This is quite small compared to the 51% increase in the Raman lasing threshold observed in a 4-cm quartz cell filled with dimethyl sulfoxide (DMSO). This observation was confirmed theoretically using a previously developed Monte Carlo model [15, 65] in which we simulated the nonlinear propagation of a Gaussian ($TEM_{0,0}$) beam and compared it with a $TEM_{3,1}$ as an oversimplified representation of the "distorted beam". This oversimplified representation will not quantitatively line up directly with the experiment, however,

it will provide a good qualitative analogue. In this simulation the SRS threshold was seen to increase by 85% in $BaSO_4$ and 131% in DMSO. Fig. 8.3 illustrates that random Raman lasing is much more robust against poor beam quality than ordinary SRS in a non-scattering medium.

8.3 Materials and Methods

Two laser systems were used for these experiments. The majority of the work was done using the 532-nm radiation generated by means of the second harmonic conversion of the 1064-nm produced by a Quanta-Ray GCR-3RA (Spectra Physics, Inc.). The GCR-3RA was injection seeded with a 10-ps pulse generated by a Vangaurd HM532 laser (Spectra Physics, Inc.). At the output, as much as 20 mJ of energy was available at 532-nm in a 50-ps pulse. The second system was a GCR-130 (Spectra Physics, Inc.) that was capable of producing 250 mJ, 8 ns pulses at 532 nm. A half-wave plate followed by a polarizing beam splitter was used to control the pump power, allowing for intensity adjustment without affecting beam quality. The pump was focused over a distance of 8.5 m onto the sample using a slightly offset 1.5x telescope constructed from a -10.0 cm focal length plano-concave lens followed by a 15.0 cm focal length plano-convex lens. The pump source was directed to the powder sample which was packed into a plastic dish with a diameter of 1.0 cm. The Fresnel reflections from a 0.16-cm thick BK7 window, placed at 45°, were coupled into an energy meter (J4-09; Coherent, Inc.) and used as a reference signal to measure the pump power.

In order to obtain a substantial optical path length in the lab, optical tables were set up at each end of the lab separated by a distance of 26.9 m. Seven broadband dielectric mirrors and metallic mirrors ranging in size from 5.08 cm diameter to 30.5 cm x 30.5 cm were placed on each table. The first of these mirrors was placed

22.2 m from the sample. The system of relay mirrors was aligned as to allow for 13 bounces of the Raman signal, each 26.9 m in distance. A 30.5 cm $\times$ 30.5 cm pick-off mirror was placed on a third optical table located a distance of 21.3 m from the final relay mirror. Finally, a 20.3-cm off-axis parabolic mirror with a focal length of 0.25 m was placed at a distance of 4.18 m from the pick-off mirror, resulting in a total optical path length from sample to primary collection optic of 397.4 m. The collected light from the 20.3-cm off-axis parabolic mirror was focused into the 200-μm entrance slit of a spectrometer (USB2000; Ocean Optics, Inc.). A 5.08-cm diameter 19.3-cm focal length achromatic doublet was placed near the focus of the parabolic mirror to help further couple the beam onto to slit. A 532-nm notch filter (Thorlabs, Inc.) was used to reject the remaining pump light before the spectrometer. Alignment was achieved with the use of a He-Ne laser that was directed down the same optical path as the pump source. To avoid stray light collection due to extraneous reflections off any of the relay mirrors in the system, each mirror was individually blocked prior to each measurement to verify that the alignment system did not support any other optical paths. This setup is shown in Fig. 8.4.

The inverse-square dependence of the intensity was measured using the same optical system described above with the spectrometer replaced by an energy meter (J3S-05; Coherent, Inc.). Barium sulfate powder (Sigma-Aldrich, Inc.) was used as the sample for these measurements. To alter the optical path length between the sample and the final collection optic, a mirror was removed from each of the optical tables. This resulted in a decrease in detection distance by 53.8 m for each set of mirrors removed. Mirror reflectivity was taken into account by assuming the metallic mirrors each had a reflectivity of 0.9 and the broadband dielectric mirrors had a reflectivity of 0.99. Clipping was calculated by finding the limiting aperture and calculating the percentage of the light cone that was reflected. For this calculation it

was assumed that only 90% of the diameter of the mirror was useful for reflecting the signal. It is important to note that the output light from the random Raman laser persists only for hundreds of picoseconds to a few nanoseconds, thus it would possible to time gate the detector to minimize the effects of the sun and other ambient light.

The spontaneous Raman spectra were collected using a custom-built Raman microscope. A 140-mW, 473-nm continuous-wave diode-pumped solid-state laser (DHOM-M-473-100; UltraLasers, Inc.) was used as the excitation source. The reflection off a dichroic mirror (LM01-480-25; Semrock, Inc.) was directed into a microscope objective (MPlan 20x/0.4NA; Olympus, Inc.). The Raman scattered light was collected by the same objective, and passed through the dichroic and a long-pass filter (Semrock BLP01-473R-25) before being imaged onto the 10-μm entrance slit of an 1/3-meter spectrometer (Acton, Inc.). For each sample, 30 averages were collected at two separate locations in the sample. Integration times varied from powder to powder, but all other acquisition parameters remained the same. The fluorescence background was removed from the spectra using a modified polyfit method with 250 integrations and a 5th-order polynomial [160].

The dependence of SRS on beam quality is often overlooked in laboratory experiments as most lasers output high-quality nearly Gaussian beams. However, as these beams propagate through air their beam quality degrades due to small variations in the refractive index, a process known as scintillation. To demonstrate that random Raman lasing is robust against poor beam quality we compared it to the generation of an SRS signal in a 1.0 cm x 4.0 cm cuvette filled with dimethyl sulfoxide (DMSO). We denote the "good" beam as the beam which we used for all the experiments. To generate a "distorted" beam several metal wires were placed in the beam path before it was focused down toward the target. The energy threshold was measured as the point when signal first becomes visible to the naked eye. In DMSO the "good"

beam had a threshold pulse energy of 0.680 ± 0.048 mJ while the "distorted" beam passed through threshold at 1.03 ± 0.072 mJ, an increase in the threshold by 51%. In $BaSO_4$ the "good" beam began to lase at 2.98 ± 0.21 mJ while the "distorted" beam required 3.80 ± 0.27 mJ, which is only a 28% increase compared to the "good" beam. Thus, while some effect on beam quality can be seen, the effect is relatively minor compared to traditional SRS generation.

To further understand the dependence of random Raman lasing on beam quality we made use of a Monte Carlo model very similar to previously developed models [25,26]. For the "good" beam we chose a pure Gaussian beam, while the "distorted" beam was modeled using a Laguerre-Gauss $TEM_{1,3}$ mode. To simulate DMSO we used a 0.0125 cm thick piece of glass followed by 4.0 cm of DMSO with an additional 0.0125 cm thick piece of glass. The glass was used to simulate the effects of the cuvette. The medium was taken to be infinite in the transverse directions. The glass was given an index of refraction, $n_{\text{glass}} = 1.5$, and an absorption coefficient, $\mu_a = 0.3$ cm^{-1}. The DMSO was given an index of refraction, $n_{\text{DMSO}} = 1.479$, and an absorption coefficient, $\mu_a = 0.3$ cm^{-1}. The $BaSO_4$ was assumed to be 1.0 cm thick and was given an index of refraction, $n_{BaSO_4} = 1.6$, a scattering anisotropy factor, $g = \langle \cos(\theta) \rangle = 0.6$, and a scattering coefficient of $\mu_s = 10.0$ cm^{-1}. Both materials were given the exact same Raman characteristics which are described by two parameters in the simulation: first, a Raman coefficient of $\mu_R = \sigma_R N = 0.001$ cm^{-1} and second, a Raman gain coefficient $\mu_{\text{SRS}} = 10^{-5}$ cm^2. The physical meaning of the Raman coefficient is quite analogous to that of μ_s and μ_a in that $1/\mu_R$ is the mean distance a pump photon travels before it undergoes Raman scattering. It is analogous to say that spontaneous Raman scattering is linear, thus it too will follow Beer's law. This coefficient must be taken artificially large due to computational constraints, and is explained and justified more fully in Refs. [26,28]. The Raman

gain coefficient is a measure of how strong the stimulated effect is. This enters into the simulation by assigning a probability of a pump photon converting to a Raman photon of $p = 1 - \exp(-\mu_{\mathrm{SRS}}\,\rho_{\mathrm{SRS}}\,\delta r)$ where δr is a small radius around the pump photon, and ρ_{SRS} is the local Raman photon density.

In order to simulate the $\mathrm{TEM}_{3,1}$ beam we must first solve, then invert the following equation for χ:

$$\int_a^{\chi} \rho(x)\mathrm{d}x = \xi, \tag{8.1}$$

where a represents the minimum value of the distribution, ξ is a uniformly distributed random number between 0 and 1, and $\rho(x)$ is the probability distribution function. To create a method that can simulate not only $\mathrm{TEM}_{3,1}$ distributions but other distributions as well, we chose to handle this numerically. To accomplish this, we make use of the well known Simpson's method for the integration and Brent's method for the subsequent inversion.

8.4 Conclusion

A new method for chemically specific remote identification of powders has been demonstrated using the random Raman lasing mechanism. Chemical identification of several similar chemical species was shown at an effective distance of over a kilometer using an inexpensive setup (we estimate the overall cost to be of the order of $\$25,000$). The random Raman lasing process that facilitates these signals has been proven, through both experiment and Monte Carlo simulation, to be robust against the poor beam quality that is likely to occur when propagating a laser beam over long distances. The ability to remotely detect chemicals in real time at large distances opens the door to a variety of applications ranging from explosives monitoring and detection to monitoring nitrate levels for smart agriculture. Future studies will be required to address the chemical sensitivity of these methods and if non-homogeneous

samples will be able to sustain lasing on multiple lines, or if the dominant species will be the only Raman line observed.

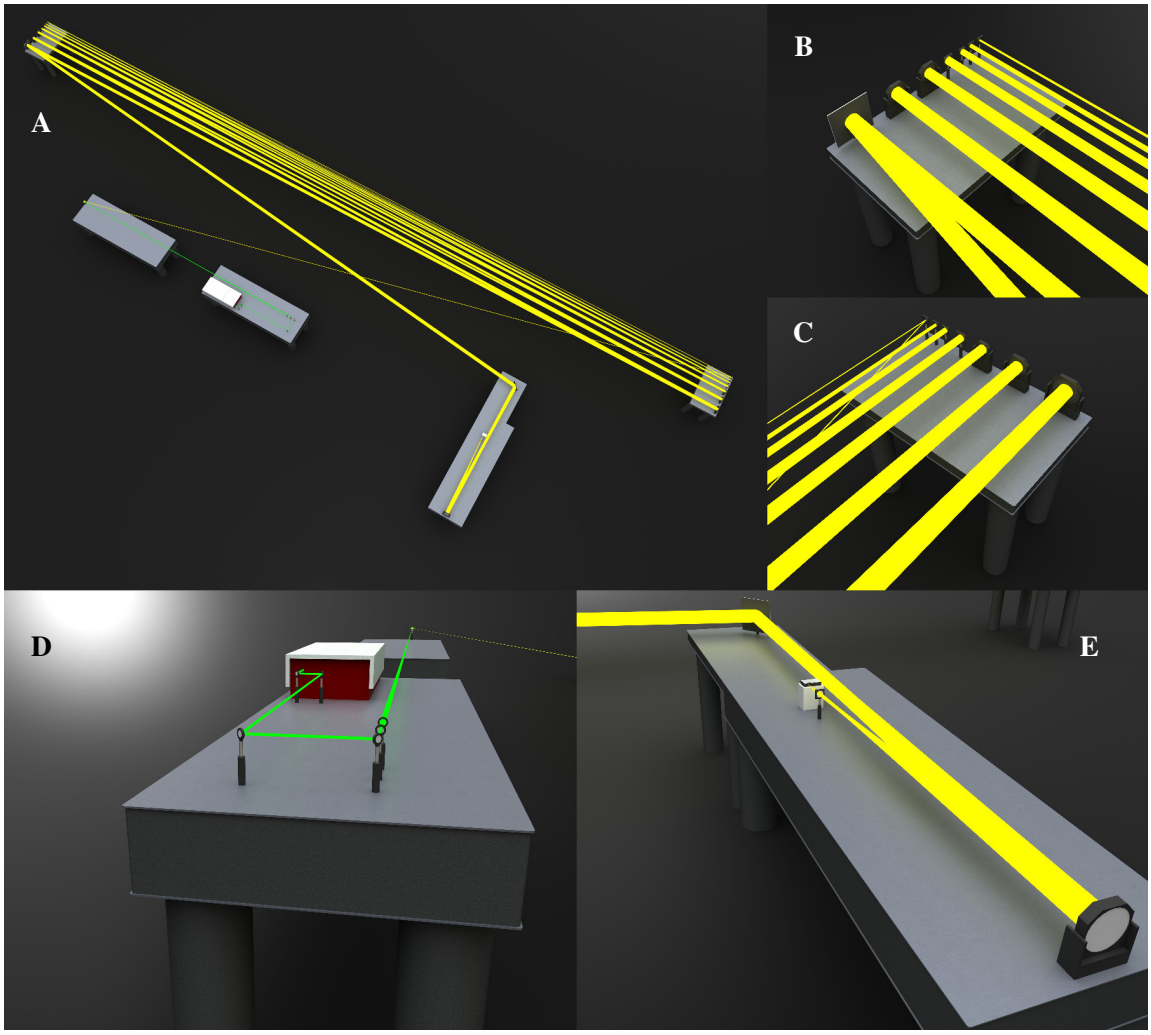

Figure 8.4: (A) To-scale drawing of the experimental setup. For reference the large optical tables are 12 ft in length, and the total path length of the sample beam from sample to the primary collection optic is 397.4 m. (B) Close-up view of the mirrors on the left end table. (C) Close-up view of the mirrors on the right end table. (D) Zoomed-in view of the preparation of the pump beam. The beam is focused onto the sample a distance of 8.5 m away from the slightly offset 1.5x telescope. (E) Close-up view of the detection scheme. The light is focused with a 2.54-m off-axis parabolic mirror onto the slits of an OceanOptics USB2000 spectrometer. A 19.3-cm achromatic doublet was used to further focus the signal onto the spectrometer.

9. IMAGING WITH RANDOM RAMAN LASING

9.1 Introduction

One of the biggest limitations of optical microscopy techniques for biological applications is speed. Laser based microscopy techniques including Raman [25, 74, 75, 101, 103, 156, 161–164], and fluorescence [72, 73, 165, 166] are limited to scanning pixel by pixel due to the speckle pattern of the laser caused by the large spatial coherence. To acquire high-resolution, megapixel-scale images at video rate (30 frames per second) one needs to have a pixel acquisition time of less than 33 ns. While laser sources with repetition rates in excess of this are readily available often times the signal level, detection equipment, and scanning rates of the laser cannot achieve sufficient speeds. Thus, to obtain real-time, dynamic information about the sample using a laser-based microscopy technique one must sacrifice resolution, signal to noise, field of view, or all of the above.

Traditionally, the way around the issue of speckle is to use an incoherent light source such as an arc lamp [167] or light emitting diodes (LEDs) [168] to do full-frame microscopy. However, such sources lack sufficient spectral radiance for Raman spectroscopy, and lack the temporal peak power to be used for any nonlinear optical effects. More recently, random lasing emission and highly multi-mode chaotic cavity lasers have been shown to provide light that is both bright and speckle free [42], but they are still broadband (typically 10's of nanometers). That is, there is no existing light source capable of producing narrowband, nanosecond-duration, speckle-free light. Random lasing via a narrowband Raman transition, known as random Raman lasing (RRL) [17, 45, 86, 114], provides a bright emission which is narrowband and has low spatial coherence.

Random lasing can be simply thought of as a laser in which feedback is provided by elastic scattering from a powder instead of the mirrors of a Fabry-Pérot [2]. Similar to traditional lasers, random lasers also have modes; however, random lasing modes are not as simple as transverse and longitudinal modes, and are usually more coupled than they would in a typical laser cavity [33]. Random lasers, or other highly multi-mode lasers, offer the unique combination of laser-like brightness, but extremely low coherence [27, 34, 38, 169]. This makes them an ideal source for imaging applications [42, 43]. Random Raman lasers [65, 85, 86], where stimulated Raman scattering (SRS) is used as the gain mechanism, is a new source with some unique features that make it an attractive imaging source in its own right [132]. Random Raman lasers have the unique advantage that the lasing medium does not need to be highly absorbing at the pump wavelength, in fact the opposite is true. The low absorption at the pump wavelength allows significantly higher power pump laser pulses to be used. With a similar conversion efficiency to other random lasers, the higher pulse energy translates into a much brighter emission that has been shown to be bright enough to observe from kilometers away [45]. Furthermore, random Raman lasers have a very narrow bandwidth, 0.1 nm is typical. This unique property could open the door to new imaging techniques, because bright, narrowband, speckle-free light sources do not presently exist. Fig. 9.1 quantifies this statement. When compared to other low-coherence light sources, in terms of the power useful to imaging, random Raman lasing emission is orders of magnitude brighter, 10,000 times brighter than the commonly used mercury arc lamp for a process with an excitation bandwidth of about 10 nm, such as fluorescence microscopy. This increased brightness directly allows for faster dynamics, and weaker contrast modalities like Raman spectroscopy, to become feasible. Furthermore, random Raman lasing can be achieved at a wide range of wavelengths simply by changing the wavelength of the pump laser.

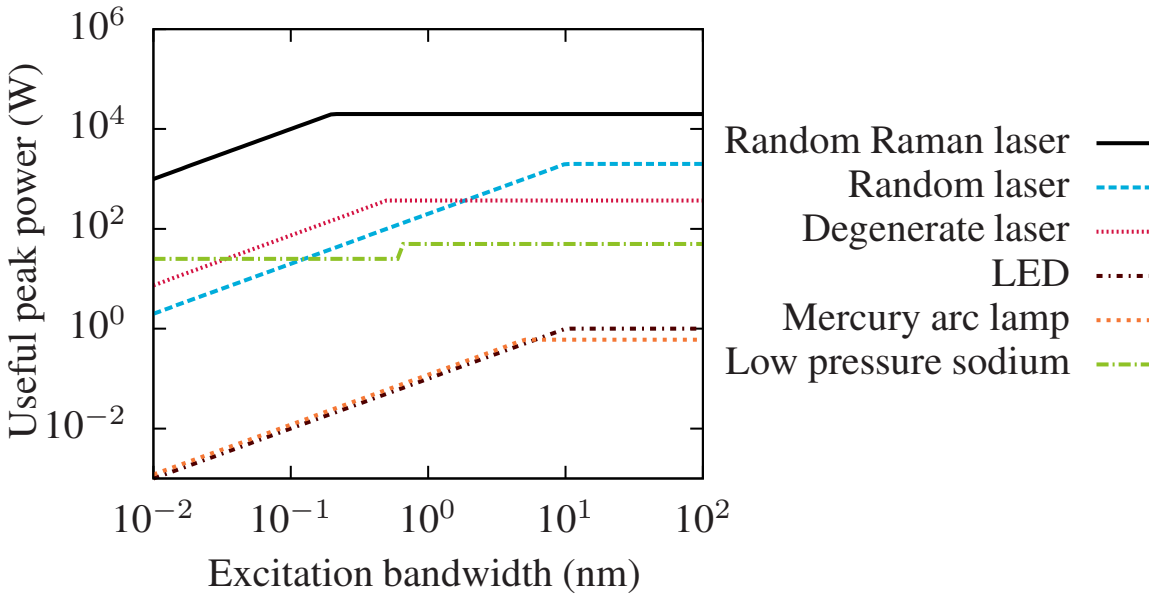

Figure 9.1: Comparison of the useful brightness of various low-spatial coherence light sources compared to the excitation bandwidth of the imaging process. For example, typical fluorescence imaging has a characteristic excitation bandwidth on the order of 10 nm. Useful peak power is defined as the peak power achieved in the specified bandwidth at the optimum wavelength for that light source.

Here, random Raman lasing emission will be evaluated for use as a bright low spatial coherence light source for microscopy. We will demonstrate proof of principle results using random Raman lasing emission as a light source by using it as a strobe light source to elucidate nanosecond dynamics in laser induced breakdown in water. Understanding the mechanical effects of laser induced breakdown in water has important consequences in laser surgery [170]. Often times, the shock-wave resulting from the breakdown leads to secondary damage and reduces the resolution of the procedure [171]. Additionally, we will discuss the spatial coherence properties of the random Raman lasing emission and compare it to other sources.

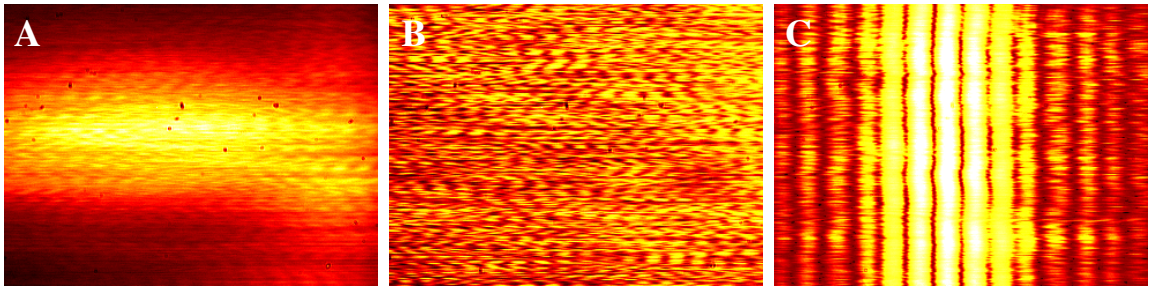

Figure 9.2: Double-slit diffraction pattern generated by (A) random Raman laser emission, (B) elastically scattered 532 nm pump, and (C) Helium-Neon laser.

9.2 Results and Discussion

To more fully explore the spatial coherence properties of RRL emission we have preformed a Young's double-slit experiment illuminated with three different light sources, RRL emission, elastically scattered 532 nm radiation from the pump laser, and a Helium-Neon laser for reference. In this experiment the RRL was pumped with a 50-ps pulse from a Spectra Physics Quanta-Ray GCR-3RA. The pulses had a pulse energy of 530 μJ and were gently focused to a beam diameter of 0.83 mm on the surface of the powder corresponding to an intensity approximately three times larger than the threshold required for random Raman lasing. The surface of the $BaSO_4$ powder was imaged to the double-slit with 10x magnification in a 4-f arrangement. The two slits were 100 μm wide and separated by 350 μm. Following the slit a cylindrical lens was used to image the vertical direction onto the CCD with unit magnification. Thus, this setup effectively probes the spatial coherence of two 10 μm thick lines on the surface of the powder separated by 35 μm. For the elastically scattered pump the laser was attenuated to well below the lasing threshold to avoid artifacts stemming from pump depletion. The Helium-Neon laser was obtained with the same lens arrangement to allow direct comparison.

The results of the double-slit experiment are shown in Fig. 9.2. They clearly show that while a small amount of spatial coherence persist in the RRL emission it is much less pronounced than even that of the elastically scattered pump radiation. This result can be understood most easily by thinking about it in terms of speckle patterns. If a single-spatial-mode laser is passed through a diffuser it will generate a speckle pattern, but if this diffuser is rotated these speckle patters will average out over time to provide a uniform illumination. Each one of these speckle patterns can be thought of as a single mode of the laser diffuser system. In a highly-multimode random laser, including the random Raman laser, each spatial mode of the laser generates a different speckle pattern for a given diffuser (elastic scattering in a random laser). These many speckle patterns average over all to provide a low-coherence source. It should be noted that the spatial coherence properties of the random Raman laser emission showed no noticeable dependence on the pump laser power, suggesting that the random Raman laser is operating in a regime where the number of lasing modes is roughly saturated.

In order to assess the degree of spatial coherence of the random Raman laser emission, we measure the speckle contrast [139]. The speckle contrast is defined to be

$$C = \frac{\sigma}{\langle I \rangle} \tag{9.1}$$

where $\langle I \rangle$ is the average value of the intensity and σ is the standard deviation. To measure the speckle contrast of the light, we first pass it through a 2 m long 600 μm fiber. The light from the fiber is left uncollimated and was allowed to overfill the array of a 16-bit CCD (Orca-ER; Hamamatsu), and the CCD was placed sufficiently far from the fiber so that the speckle grain size is significantly larger than the pixel size of the CCD. To demonstrate the capabilities of the setup and

provide a basis to compare the random Raman lasing emission we used a helium neon laser as a highly coherent source, and a halogen light as a low-coherence source. The resulting images and speckle contrast are shown in Fig. 9.3. To measure the speckle contrast we have chosen a 400x400 region of the CCD that was clear of debris and subdivided that into 25 80x80 sub-regions. The speckle contrast of each sub region is computed independently by first subtracting a pedestal to reduce the effect of the CCD dark counts on the calculation then computing the average and standard deviation [140, 141]. This helps minimize any effects due to non-uniform illumination of the array. Multiple images were taken. Those used in the calculations for the random Raman lasing and halogen light source were selected by rejecting any images with saturated pixels and requiring the average counts per pixel to be greater than 20,000. This minimizes the effect of noise due to the CCD while ensuring that saturation is not occurring. For the Helium-Neon (HeNe) images, the requirement on average pixel count was not enforced, but the laser power was adjusted to maximize the dynamic range of the detector without saturation. All together, 21 images were used for the HeNe calculations, 28 images for the random Raman lasing emission, and 101 images for the white light. All 25 sub-regions from each image were pooled together and averaged. The errors quoted in the figure are the standard deviation of these averages.

There is still a small, but measurable amount of spatial coherence present in the random Raman laser emission. In practice, this is a tolerable amount of speckle for the vast majority of imaging applications, and with a better understanding of the fundamental processes that give rise to this emission this can likely be improved. Furthermore, the random Raman laser has the peculiar property of producing a unique speckle pattern with each laser pulse, allowing the speckle contrast to be reduced by averaging over multiple pulses. The speckle patterns formed from 4

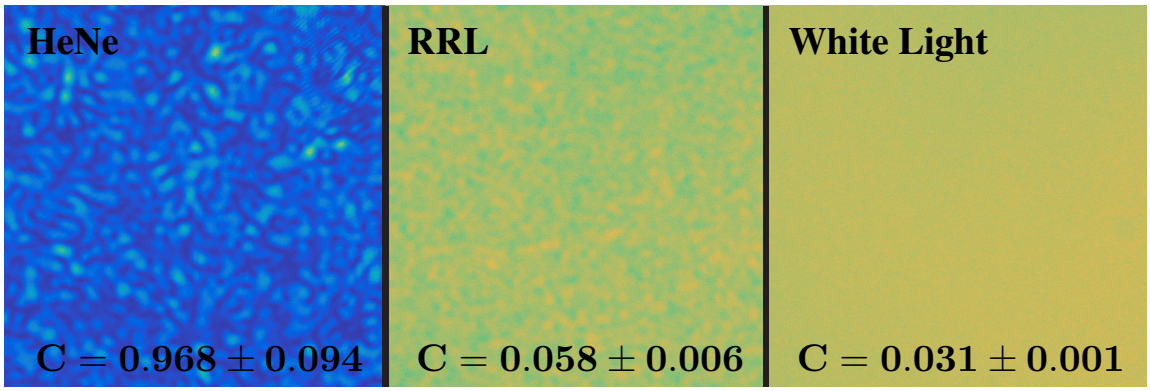

Figure 9.3: Speckle contrast of random Raman laser emission compared to highly coherent and highly incoherent sources.

consecutive laser pulses are shown in Fig. 9.4. This effect is not observed in other random lasers in powder. This could be indicative that the powder is moving slightly from shot to shot, or could be the result of more interesting dynamics of the lasing process itself. Either way, further experiments are needed to explore the mechanism responsible, but the resulting effect is beneficial for imaging applications.

In addition to strobe photography applications, RRL emission could have applications as an spatially-incoherent source for spectroscopy. Fig. 9.5 shows the spontaneous Raman spectrum for $BaSO_4$ has a spontaneous emission bandwidth of 8 cm^{-1} for the strongest Raman line. This linewidth convoluted with the pump laser spectrum (in this case it is sufficiently narrow that it can be neglected) provides the maximum possible bandwidth of the RRL much like the spontaneous emission bandwidth would determine the maximum gain bandwidth of a laser. Additionally, the RRL emission spectrum is shown to illustrate the lack of the weaker Raman peaks seen in the spontaneous spectrum. The wider width of the RRL emission spectrum here is due to the fact that a lower resolution spectrometer was used to acquire this data. Thus the width of this feature is determined solely by the resolution of the

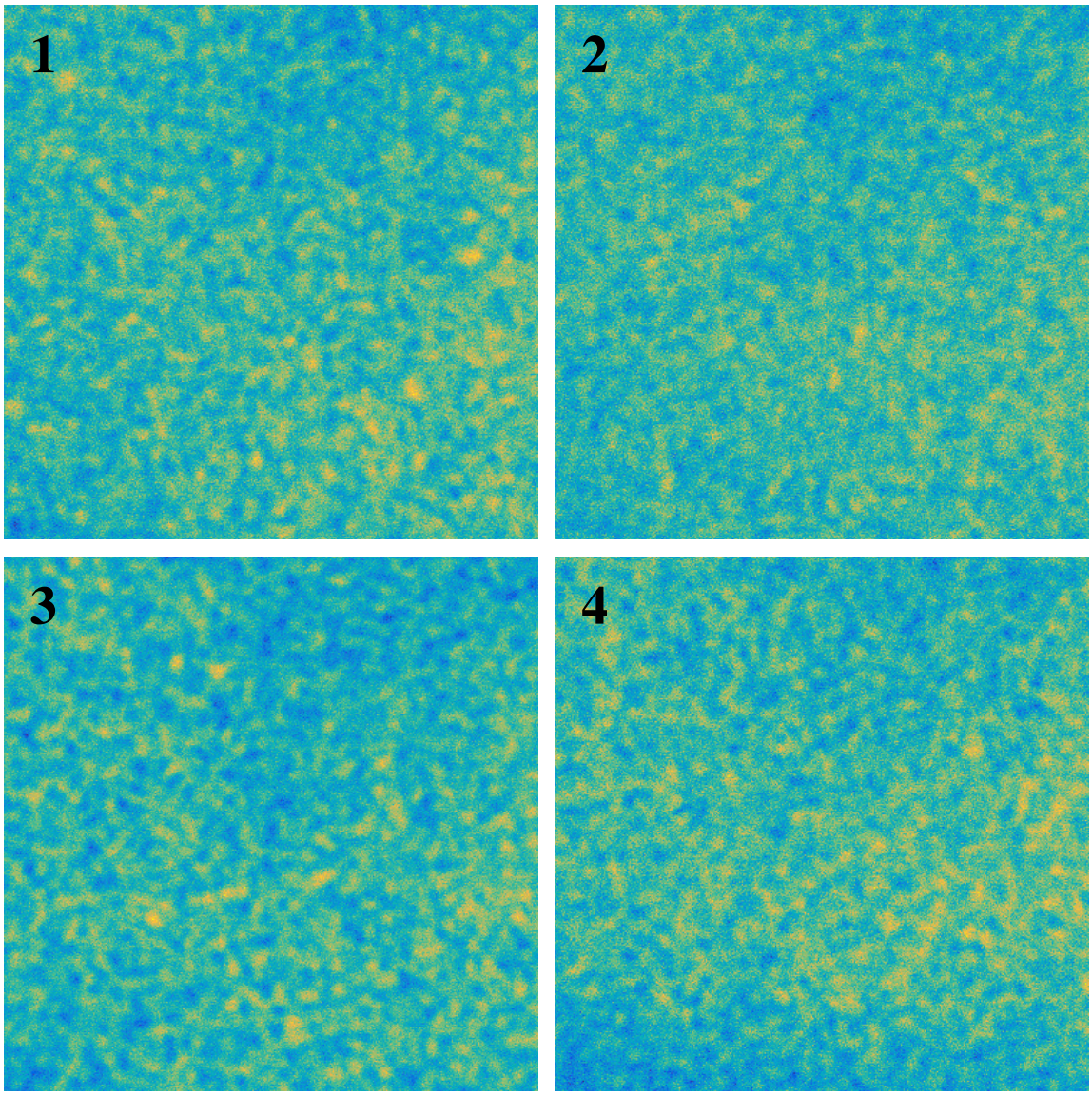

Figure 9.4: Four consecutive pulses out of the random Raman laser, illustrating that a new speckle is generated with each shot. The images have been scaled to maximize the contrast to highlight the faint speckle grains.

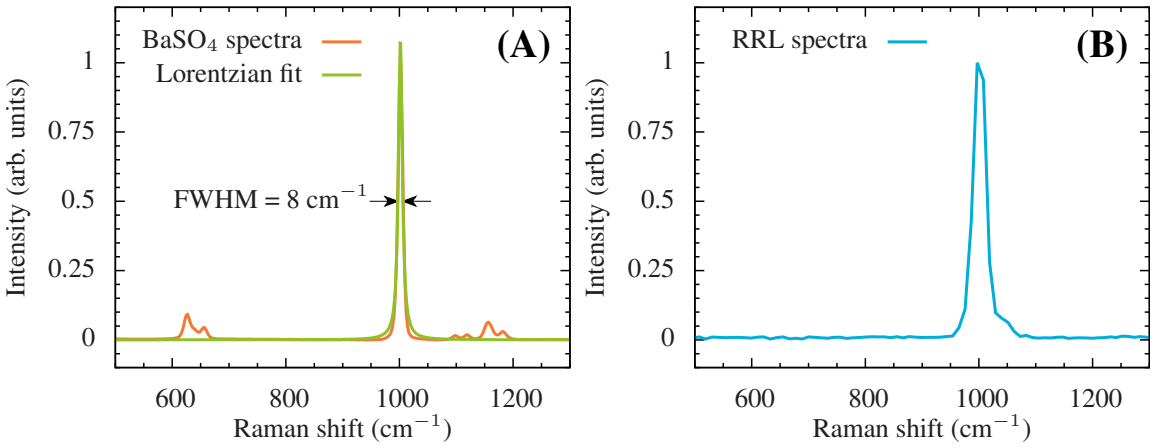

Figure 9.5: (A) Linewidth of the spontaneous Raman spectrum for $BaSO_4$. The Lorentzian fit give the full-width at half-maximum width to be 8 cm^{-1} (0.25 nm at 562 nm). (B) Spectrum of RRL emission. Note that this data set was taken with a lower-resolution spectrometer such that the width of this peak is determined by the resolution of that spectrometer and not by the emission.

spectrometer and not by the RRL emission. The narrow RRL linewidth would be sufficient for full-field Raman spectroscopy. Given the speckle-free nature combined with the narrow line-width of the RRL emission it would in principle be possible to acquire an entire Raman spectral image in a single laser shot. Even if many shots are required to obtain the required signal to noise this would likely still far exceed the speed at which current imaging Raman microscopes can obtain spectroscopic images. The obvious limitation for such a technique is the lack of a spectrometer capable of detecting a Raman spectrum from each point in a 2-dimensional array. Currently, no such detector exists; however, recent advances in compressive sensing offer hope in this area [172].

To image laser induced breakdown in water the setup pictured schematically in Fig. 9.6 was used. A picosecond seeded Nd:YAG regenerative amplifier (Quanta-Ray GCR-3RA; Spectra Physics) generated 50-ps pulses at a repetition rate of 10-Hz.

The residual 1064-nm light from the doubling process was split off and focused into a cuvette containing water using a 10x long working distance microscope objective (Mitutoyo). The power of the 1064 was adjusted using neutral density filters to get a pulse energy of 70 uJ. The 532-nm pulse out of the laser was sent through a delay stage and reflected off a longpass dichroic beamsplitter (Di02-R532; Semrock) prior to being focused onto barium sulfate powder (ReagentPlus; Sigma-Aldrich) that was lightly packed into a 1-cm diameter, 1-cm deep container. Before being focused onto the powder, the 532-nm pulse energy was 1.7 mJ. The sample was placed in front of the focal plane so that the beam on the surface of the powder was approximately 1-mm in diameter. The resulting random Raman lasing emission was transmitted through the dichroic beam-splitter and residual 532-nm light was further attenuated by an additional 6 OD notch filter (NF533-17; ThorLabs). The random Raman laser emission was then used to illuminate the laser induced breakdown as shown in Fig. 9.6B. The laser induced breakdown was imaged to a CCD (Orca-100; Hamamatsu) using an identical 10x microscope objective and a 500 mm focal length lens for a total magnification of 25x. A 560 nm bandpass filter was used to reject any plasma emission or higher order random Raman emission lines [114].

The acquired images are shown in Fig. 9.7. To acquire images at different times, the delay stage was translated. Time zero corresponds to when the breakdown pulse and random Raman laser imaging pulse arrive at the same time. The images were scaled to maximize the contrast but no further image processing was done. The resulting shock wave can be clearly seen moving out from the initial breakdown event as time progresses. There is slight non-uniformity in the illumination, but this could be corrected for through background subtraction or passing the illumination through a multi-mode fiber and imaging the tip of the fiber through the system.

In addition to exhibiting exceptional brightness and nearly speckle-free behav-

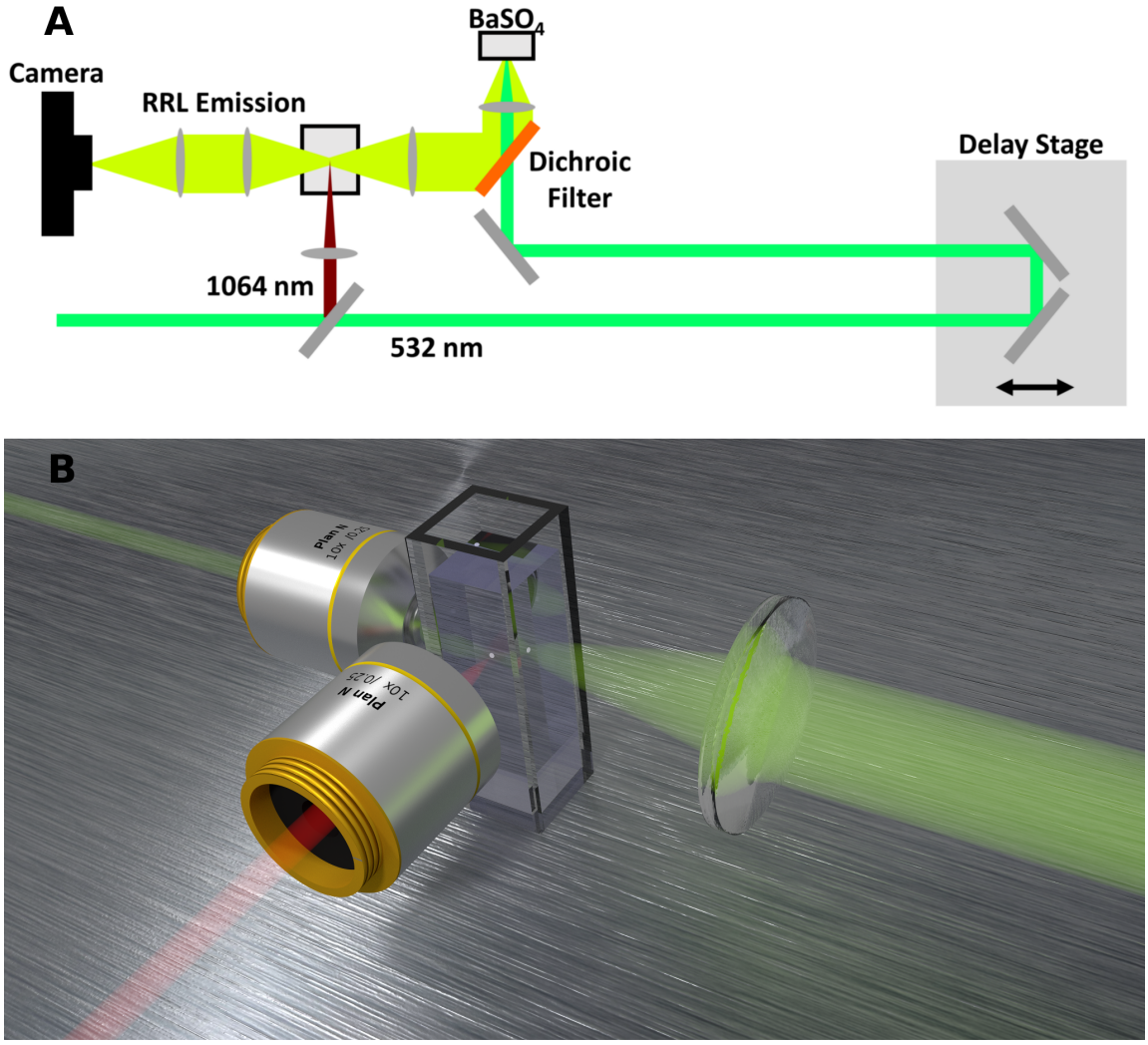

Figure 9.6: Schematic diagram of the experimental setup.

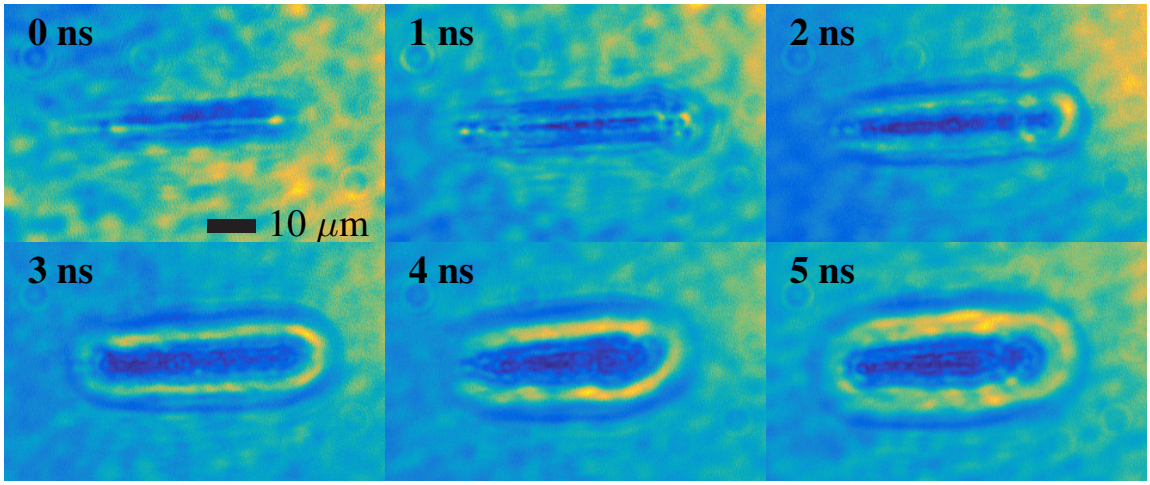

Figure 9.7: Images of laser induced breakdown in water using random Raman lasing emission as the strobe. The images have been scaled to maximize the contrast, but no other image processing was done.

ior, random Raman laser emission has the advantage that the wavelength can be changed relatively simply. In our present setup, the emission undergoes a 985 cm^{-1} Raman shift due to barium sulfate from the 532 nm pump light, resulting in fundamental emission at 562 nm. However, random Raman lasing is capable of producing bright higher order effects that lead to additional emission at 595 nm, and even 632 nm [114]. Another method to acquire different color emission would be to use a different pump wavelength. This could have tremendous applications to fluorescence microscopy where the illumination pulse could be optimized to maximize the fluorescence emission.

9.3 Conclusion

We have shown that random Raman laser emission is a unique source of light. It can be made very bright (a few percent of the pump energy), it is sufficiently narrowband for spectroscopic applications with a linewidth of at most 8 cm^{-1}, and, most importantly, it is sufficiently spatially incoherent such that speckle free full-

frame images can be obtained. If you compare random Raman lasing emission with other low-coherence light sources, the advantage is clear. The random Raman laser is capable of delivering 10,000 times the useful peak power of mercury arc lamps for fluorescence imaging. This will open up a window to study faster dynamics and potentially new applications using weaker, but more chemically specific modalities such as Raman spectroscopy. The random Raman laser light source has the potential to Finally, we demonstrate proof of principle images of laser induced breakdown in water illuminated by random Raman laser emission.

10. CONCLUSION

The effect of the elastic scattering of light on nonlinear interactions yields man interesting effects. While conventional wisdom states that diffusion spreads out light intensity, making it difficult to obtain the high intensities required for nonlinear interactions, this view completely changes on time scales short compared to diffusion. In this regime, the fact that the speed of diffusion is slow compared to the speed of light results in the light being trapped near the surface, forming a transient region of high intensity and allowing nonlinear effects to flourish.

We started by demonstrating that the effects of scattering can be leveraged to enhance linear optical effects through the increased path length the photons take along their random walk through the turbid media. Following that, we outlined the theoretical predictions for the existence of random Raman lasing in a three-dimensional bulk powder and outlining the first steps towards building in nonlinear optical effects into Monte Carlo simulations. Then we discussed the experimental realization of this new physical system, random Raman lasing, as the first three-dimensional random laser based on stimulated Raman gain. Following that, we discussed in detail our nonlinear Monte Carlo model which demonstrated that by assigning what amounts to an interaction between photon packets, we can accurately describe nonlinear optical effects. Furthermore, we can use this model to explain the existence of cascaded higher-order stimulated Raman scattering effects present in random Raman lasing systems. Finally, we discuss several experimentally measured properties of random Raman lasing that cannot be explained through our Monte Carlo model and propose that these discrepancies could be the result of the presence of Anderson localization. If this interpretation is proven true, it would make random

Raman lasing a fantastic system for probing the effects of wave interference on turbid systems with gain.

In addition to outlining the discovery, theoretical model, and fundamental properties of random Raman lasing, we outline a few exciting potential applications of random Raman lasers. First, due to the incredibly bright, chemically specific emission from random Raman lasers, we demonstrated their use in remote sensing. Single shot detection was measured in the lab at a distance of 400 m, but extrapolating our signal to noise to straight line distances in the atmosphere, it would likely be possible to identify a chemical in a single shot, from 10 km away. Additionally, due to the low spatial coherence of the emission, random Raman lasers make an ideal light source for imaging. The short pulse, narrow-band nature of the light source, gives rise to a light source that is 10,000 times more bright than traditionally used light sources, and a full order of magnitude brighter than the brightest proposed light source.

To conclude, we have presented the discovery of random Raman lasing, outlined many of its fundamental properties, and finally, demonstrated many exciting applications.

REFERENCES

[1] P. E. Wolf and G. Maret, "Weak localization and coherent backscattering of photons in disordered media," Phys. Rev. Lett. **55**, 2696–2699 (1985).

[2] H. Cao, Y. G. Zhao, S. T. Ho, E. W. Seelig, Q. H. Wang, and R. P. H. Chang, "Random laser action in semiconductor powder," Phys. Rev. Lett. **82**, 2278–2281 (1999).

[3] M. Segev, Y. Silberberg, and D. N. Christodoulides, "Anderson localization of light," Nat. Photonics **7**, 197–204 (2013).

[4] C. F. Bohren and D. R. Huffman, *Absorption and Scattering of Light by Small Particles* (John Wiley & Sons, 2008).

[5] G. N. Plass and G. W. Kattawar, "Monte Carlo calculations of light scattering from clouds," Appl. Opt. **7**, 415–419 (1968).

[6] L. Wang, S. L. Jacques, and L. Zheng, "MCML - Monte Carlo modeling of light transport in multi-layered tissues," Comput. Meth. Prog. Bio. **47**, 131–146 (1995).

[7] A. Sassaroli, C. Blumetti, F. Martelli, L. Alianelli, D. Contini, A. Ismaelli, and G. Zaccanti, "Monte Carlo procedure for investigating light propagation and imaging of highly scattering media," Appl. Opt. **37**, 7392–7400 (1998).

[8] X. Deng and M. Gu, "Penetration depth of single-, two-, and three-photon fluorescence microscopic imaging through human cortex structures: Monte Carlo simulation," Appl. Opt. **42**, 3321–3329 (2003).

[9] J. C. Ramella-Roman, S. A. Prahl, and S. L. Jacques, "Three Monte Carlo programs of polarized light transport into scattering media: part I," Opt. Express **13**, 4420–4438 (2005).

[10] G. M. Palmer and N. Ramanujam, "Monte Carlo-based inverse model for calculating tissue optical properties. Part I: Theory and validation on synthetic phantoms," Appl. Opt. **45**, 1062 (2006).

[11] A. Leray, C. Odin, E. Huguet, F. Amblard, and Y. Le Grand, "Spatially distributed two-photon excitation fluorescence in scattering media: experiments and time-resolved Monte Carlo simulations," Opt. Commun. **272**, 269–278 (2007).

[12] M. D. Keller, R. H. Wilson, M.-A. Mycek, and A. Mahadevan-Jansen, "Monte Carlo model of spatially offset Raman spectroscopy for breast tumor margin analysis," Appl. Spectrosc. **64**, 607–614 (2010).

[13] Q. Fang, "Mesh-based Monte Carlo method using fast ray-tracing in Plücker coordinates," Biomed. Opt. Express **1**, 165 (2010).

[14] A. Doronin and I. Meglinski, "Peer-to-peer Monte Carlo simulation of photon migration in topical applications of biomedical optics," J. Biomed. Opt. **17**, 90504 (2012).

[15] B. H. Hokr and V. V. Yakovlev, "Raman signal enhancement via elastic light scattering," Opt. Express **21**, 11757–11762 (2013).

[16] V. Periyasamy and M. Pramanik, "Monte Carlo simulation of light transport in turbid medium with embedded objectspherical, cylindrical, ellipsoidal, or cuboidal objects embedded within multilayered tissues," J. Biomed. Opt. **19**, 45003 (2014).

[17] B. H. Hokr, V. V. Yakovlev, and M. O. Scully, "Efficient time-dependent Monte Carlo simulations of stimulated Raman scattering in a turbid medium," ACS Photonics **1**, 1322–1329 (2014).

[18] B. H. Hokr, J. N. Bixler, G. Elpers, B. Zollars, R. J. Thomas, V. V. Yakovlev, and M. O. Scully, "Modeling focusing Gaussian beams in a turbid medium with Monte Carlo simulations," Opt. Express **23**, 8699 (2015).

[19] H. Nguyen, *GPU Gems 3* (Addison-Wesley Professional, 2007), 1st ed.

[20] G. E. P. Box and M. E. Muller, "A note on the generation of random normal deviates," Ann. Math. Stat. **29**, 610–611 (1958).

[21] N. Everall, T. Hahn, P. Matousek, A. W. Parker, and M. Towrie, "Photon migration in Raman spectroscopy," Appl. Spectrosc. **58**, 591–597 (2004).

[22] J. S. Hendricks and T. E. Booth, "MCNP variance reduction overview," in "Monte-Carlo Methods Appl. Neutronics, Photonics Stat. Phys.", , vol. 240 of *Lecture Notes in Physics*, R. Alcouffe, R. Dautray, A. Forster, G. Ledanois, and B. Mercier, eds. (Springer Berlin Heidelberg, 1985), pp. 83–92.

[23] A. S. Haka, K. E. Shafer-Peltier, M. Fitzmaurice, J. Crowe, R. R. Dasari, and M. S. Feld, "Diagnosing breast cancer by using Raman spectroscopy," Proc. Natl. Acad. Sci. U. S. A. **125**, 12371–12376 (2005).

[24] A. Nijssen, K. Maquelin, L. F. Santos, P. J. Caspers, T. C. Bakker Schut, J. C. den Hollander, M. H. A. Neumann, and G. J. Puppels, "Discriminating basal cell carcinoma from perilesional skin using high wave-number Raman spectroscopy," J. Biomed. Opt. **12**, 34004 (2007).

[25] R. Arora, G. I. Petrov, V. V. Yakovlev, and M. O. Scully, "Detecting anthrax in the mail via coherent Raman microspectroscopy," Proc. Natl. Acad. Sci. U.

S. A. **109**, 1151–1153 (2012).

[26] N. Bloembergen, "The stimulated Raman effect," Am. J. Phys. **35**, 989–1023 (1967).

[27] H. Cao, "Lasing in random media," Waves in Random Media **13**, R1–R39 (2003).

[28] X. Jiang and C. M. Soukoulis, "Time dependent theory for random lasers," Phys. Rev. Lett. **85**, 70–73 (2000).

[29] D. S. Wiersma, "The smallest random laser," Nature **406**, 132–133 (2000).

[30] G. van Soest, J. Poelwijk Frank, R. Sprik, and A. Lagendijk, "Dynamics of a random laser above threshold," Phys. Rev. Lett. **86**, 1522–1525 (2001).

[31] S. Mujumdar, M. Ricci, R. Torre, and D. S. Wiersma, "Amplified extended modes in random lasers," Phys. Rev. Lett. **93**, 53903 (2004).

[32] M. A. Noginov, G. Zhu, C. Small, and J. Novak, "Neodymium random laser with external mirrors," Appl. Phys. B Lasers Opt. **84**, 269–273 (2006).

[33] H. E. Türeci, L. Ge, S. Rotter, and A. D. Stone, "Strong interactions in multimode random lasers," Science (80-.). **320**, 643–646 (2008).

[34] B. Redding, M. A. Choma, and H. Cao, "Spatial coherence of random laser emission." Opt. Lett. **36**, 3404–6 (2011).

[35] H. E. Türeci, A. D. Stone, L. Ge, S. Rotter, and R. J. Tandy, "Ab initio self-consistent laser theory and random lasers," Nonlinearity **22**, C1–C18 (2009).

[36] H. Cao, "Review on latest developments in random lasers with coherent feedback," J. Phys. A. Math. Gen. **38**, 10497–10535 (2005).

[37] Z. Hu, Q. Zhang, B. Miao, Q. Fu, G. Zou, Y. Chen, Y. Luo, D. Zhang, P. Wang, H. Ming, and Q. Zhang, "Choerent random fiber laser based on nanoparticles

scattering in the extremely weakly scattering regime," Phys. Rev. Lett. **109**, 253901 (2012).

[38] B. Redding, A. Cerjan, X. Huang, M. L. Lee, A. D. Stone, M. A. Choma, and H. Cao, "Low spatial coherence electrically pumped semiconductor laser for speckle-free full-field imaging." Proc. Natl. Acad. Sci. U. S. A. **112**, 1304–1309 (2015).

[39] G. Pólya, "Über eine Aufgabe der Wahrscheinlichkeitsrechnung betreffend die Irrfahrt im Straßennetz," Math. Ann. **84**, 149–160 (1921).

[40] A. Pick, A. Cerjan, D. Liu, A. W. Rodriguez, A. D. Stone, Y. D. Chong, and S. G. Johnson, "Ab initio multimode linewidth theory for arbitrary inhomogeneous laser cavities," Phys. Rev. A **91**, 063806 (2015).

[41] A. Cerjan, A. Pick, Y. Chong, S. G. Johnson, and A. D. Stone, "Quantitative test of general theories of the intrinsic laser linewidth," p. 24 (2015).

[42] B. Redding, M. A. Choma, and H. Cao, "Speckle-free laser imaging using random laser illumination," Nat. Photonics **6**, 355–359 (2012).

[43] A. Mermillod-Blondin, H. Mentzel, and A. Rosenfeld, "Time-resolved microscopy with random lasers." Opt. Lett. **38**, 4112–5 (2013).

[44] H. Cao, "Random Thoughts," Nat. Photonics **7**, 164–165 (2013).

[45] B. H. Hokr, J. N. Bixler, G. D. Noojin, R. J. Thomas, B. A. Rockwell, V. V. Yakovlev, and M. O. Scully, "Single-shot stand-off chemical identification of powders using random Raman lasing," Proc. Natl. Acad. Sci. **111**, 12320–12324 (2014).

[46] B. Cletus, W. Olds, E. L. Izake, S. Sundarajoo, P. M. Fredericks, and E. Jaatinen, "Combined time- and space-resolved Raman spectrometer for the non-

invasive depth profiling of chemical hazards," Anal. Bioanal. Chem. **403**, 255–263 (2012).

[47] F. Ariese, H. Meuzelaar, M. M. Kerssens, J. B. Buijs, and C. Gooijer, "Picosecond Raman spectroscopy with a fast intensified CCD camera for depth analysis of diffusely scattering media," Analyst **134**, 1192–1197 (2009).

[48] A. Alù and N. Engheta, "Tuning the scattering response of optical nanoantennas with nanocircuit loads," Nat. Photonics **2**, 307–310 (2008).

[49] P. Matousek, "Raman signal enhancement in deep spectroscopy of turbid media," Appl. Spectrosc. **61**, 845–854 (2007).

[50] W. C. Shih, K. L. Bechtel, and M. S. Feld, "Intrinsic Raman spectroscopy for quantitative biological spectroscopy part 1: theory and simulations," Opt. Express **16**, 12726–12736 (2008).

[51] T. J. Pfefer, Q. Wang, and R. A. Drezek, "Monte Carlo modeling of time-resolved fluorescence for depth-selective interrogation of layered tissue," Comput. Meth. Prog. Bio. **104**, 161–167 (2011).

[52] Y. Zhao, X. Li, and L. Ma, "Multidimensional Monte Carlo model for two-photon laser-induced fluorescence and amplified spontaneous emission," Comput. Phys. Commun. **183**, 1588–1595 (2012).

[53] A. Doronin and I. Meglinski, "Online object oriented Monte Carlo computational tool for the needs of biomedical optics," Biomed. Opt. Express **2**, 2461–2469 (2011).

[54] L. G. Henyey and J. L. Greenstein, "Diffuse radiation in the galaxy," Astrophysics **93**, 70–83 (1941).

[55] R. W. Boyd, *Nonlinear Optics* (Academic Press, 2003), 2nd ed.

[56] O. Mengual, G. Meunier, I. Cayré, K. Puech, and P. Snabre, "TURBISCAN MA 2000: multiple light scattering measurement for concentrated emulsion and suspension instability analysis," Talanta **50**, 445–456 (1999).

[57] B. B. Das, F. Liu, and R. R. Alfano, "Time-resolved fluourescence and photon migration studies in biomedical and model random media," Reports Prog. Phys. **60**, 227–292 (1997).

[58] P. Matousek, I. P. Clark, E. R. C. Draper, M. D. Morris, A. E. Goodship, N. Everall, M. Towrie, W. F. Finney, and A. W. Parker, "Subsurface probing in diffusely scattering media using spatially offset Raman spectroscopy," Appl. Spectrosc. **59**, 393–400 (2005).

[59] M. D. Morris, P. Matousek, M. Towrie, A. W. Parker, A. E. Goodship, and E. R. C. Draper, "Kerr-gated time-resolved Raman spectroscopy of equine cortical bone tissue," J. Biomed. Opt. **10**, 14014 (2005).

[60] G. Eckhardt, R. W. Hellwarth, F. J. McClung, S. E. Schwarz, D. Weiner, and E. J. Woodbury, "Stimulated Raman scattering from organic liquids," Phys. Rev. Lett. **9**, 455–457 (1962).

[61] A. E. Perkins and N. M. Lawandy, "Light amplification in a disordered Raman medium," Opt. Commun. **162**, 191–194 (1999).

[62] V. S. Letokhov, "Generation of light by a scattering medium with negative resonance absorption," Sov. Phys. JETP **26**, 835–840 (1968).

[63] A. Z. Genack and J. M. Drake, "Scattering for super-radiation," Nature **368**, 400–401 (1994).

[64] N. M. Lawandy, R. M. Balachandran, A. S. L. Gomes, and E. Sauvain, "Laser action in strongly scattering media," Nature **368**, 436–438 (1994).

[65] B. H. Hokr and V. V. Yakovlev, "A proposal for a random Raman laser," J. Mod. Opt. **61**, 57–60 (2014).

[66] J. Bertolotti, E. G. van Putten, C. Blum, A. Lagendijk, L. Vos Willem, and A. P. Mosk, "Non-invasive imaging through opaque scattering layers," Nature **491**, 232–234 (2012).

[67] I. Tegen, A. A. Lacis, and I. Fung, "The influence on climate forcing of mineral aerosols from disturbed soils," Nature **380**, 419–422 (1996).

[68] D. Malonek and A. Grinvald, "Interactions between Electrical Activity and Cortical Microcirculation Revealed by Imaging Spectroscopy: Implications for Functional Brian Mapping," Science (80-.). **272**, 551–554 (1996).

[69] M. P. V. Albada and A. Lagendijk, "Observation of weak localization of light in a random medium," Phys. Rev. Lett. **55**, 2692–2695 (1985).

[70] O. Katz, E. Small, Y. Bromberg, and Y. Silberberg, "Focusing and compression of ultrashort pulses through scattering media," Nat. Photonics **5**, 372–377 (2011).

[71] A. P. Mosk, A. Lagendijk, G. Lerosey, and M. Fink, "Controlling waves in space and time for imaging and focusing in complex media," Nat. Photonics **6**, 283–292 (2012).

[72] F. Helmchen and W. Denk, "Deep tissue two-photon microscopy," Nat. Methods **2**, 932–940 (2005).

[73] N. G. Horton, K. Wang, D. Kobat, C. G. Clark, F. W. Wise, C. B. Schaffer, and C. Xu, "In vivo three-photon microscopy of subcortical structures within an intact mouse brain," Nat. Photonics **7**, 205–209 (2013).

[74] C. W. Freudiger, W. Min, B. G. Saar, S. Lu, G. R. Holtom, C. He, J. C. Tsai, J. X. Kang, and X. S. Xie, "Label-free biomedical imaging with high sensitivity by stimulated Raman scattering microscopy," Science (80-.). **322**, 1857–1861 (2008).

[75] V. V. Yakovlev, H. F. Zhang, G. D. Noojin, M. L. Denton, R. J. Thomas, and M. O. Scully, "Stimulated Raman photoacoustic imaging," Proc. Natl. Acad. Sci. U. S. A. **107**, 20335–20339 (2010).

[76] E. B. Hanlon, R. Manoharan, T. W. Koo, K. E. Shafer, J. T. Motz, M. Fitzmaurice, J. R. Kramer, I. Itzkan, R. R. Dasari, and M. S. Feld, "Prospects for in vivo Raman spectroscopy," Phys. Med. Biol. **45**, R1 (2000).

[77] Y. R. Shen and N. Bloembergen, "Theory of stimulated Brillouin and Raman scattering," Phys. Rev. **137**, A1787 (1965).

[78] S. M. Spillane, T. J. Kippenberg, and K. J. Vahala, "Ultralow-threshold Raman laser using a spherical dielectric microcavity," Nature **415**, 621–623 (2002).

[79] H. Rong, A. Liu, R. Jones, O. Cohen, D. Hak, R. Nicolaescu, A. Fang, and M. Paniccia, "An all-silicon Raman laser," Nature **433**, 292–294 (2005).

[80] H. Rong, R. Jones, A. Liu, O. Cohen, D. Hak, A. Fang, and M. Paniccia, "A continuous-wave Raman silicon laser," Nature **433**, 725–728 (2005).

[81] M. Troccoli, A. Belyanin, F. Capasso, E. Cubukcu, D. L. Sivco, and A. Y. Cho, "Raman injection laser," Nature **433**, 845–848 (2005).

[82] D. S. Wiersma, "The physics and applications of random lasers," Nat. Phys. **4**, 359–367 (2008).

[83] H. Cao, Y. Ling, J. Y. Xu, and C. Q. Cao, "Photon statistics of random lasers with resonant feedback," Phys. Rev. Lett. **86**, 4524–4527 (2001).

[84] H. Cao, J. Y. Xu, D. Z. Zhang, S.-H. Chang, S. T. Ho, E. W. Seelig, X. Liu, and R. P. H. Chang, "Spatial confinement of laser light in active random media," Phys. Rev. Lett. **84**, 5584–5587 (2000).

[85] S. K. Turitsyn, S. A. Babin, A. E. El-Taher, P. Harper, D. V. Churkin, S. I. Kablukov, J. D. Ania-Castañón, V. Karalekas, and E. V. Podivilov, "Random distributed feedback fibre laser," Nat. Photonics **4**, 231–235 (2010).

[86] B. H. Hokr, J. N. Bixler, M. Cone, J. D. Mason, H. T. Beier, G. D. Noojin, G. I. Petrov, L. A. Golovan, R. J. Thomas, B. A. Rockwell, and V. V. Yakovlev, "Bright emission from a random Raman laser," Nat. Commun. **5**, 4356 (2014).

[87] M. P. van Albada, B. A. van Tiggelen, A. Lagendijk, and A. Tip, "Speed of propagation of classical waves in strongly scattering media," Phys. Rev. Lett. **66**, 3132–3135 (1991).

[88] A. Lubatsch, J. Kroha, and K. Busch, "Theory of light diffusion in disordered media with linear absorption or gain," Phys. Rev. B **71**, 184201 (2005).

[89] H. B. Lin, J. D. Eversole, and A. J. Campillo, "Continuous-wave stimulated Raman scattering in microdroplets," Opt. Lett. **17**, 828–830 (1992).

[90] R. G. Pinnick, A. Biswas, G. Fernández, P. Chlek, R. L. Armstrong, H. Latifi, E. Creegan, V. Srivastava, and M. Jarzembski, "Stimulated Raman scattering in micrometer-sized droplets: time-resolved measurements," Opt. Lett. **13**, 494–496 (1988).

[91] B. C. Wilson and G. Adam, "A Monte Carlo model for the absorption and flux distributions of light in tissue," Med. Phys. **10**, 824–830 (1983).

[92] M. Keijzer, S. L. Jacques, S. A. Prahl, and A. J. Welch, "Light distributions in artery tissue: Monte Carlo simulations for finite-diameter laser beams," Lasers

Surg. Med. **9**, 148–154 (1989).

[93] D. B. Kirk and W.-m. W. Hwu, *Programming Massively Parallel Processors: A Hands-on Approach* (Elsevier, Waltham, MA, 2012), 2nd ed.

[94] J. Y. Qu, C. E. MacAulay, S. Lam, and B. Palcic, "Laser-induced fluorescence spectroscopy at endoscopy: tissue optics, Monte Carlo modeling, and in vivo measurements," Opt. Eng. **34**, 3334–3343 (1995).

[95] A. J. Welch, C. Gardner, R. Richards-Kortum, E. Chan, G. Criswell, J. Pfefer, and S. Warren, "Propagation of fluorescent light," Lasers Surg. Med. **21**, 166–178 (1997).

[96] Q. Liu, C. Zhu, and N. Ramanujam, "Experimental validation of Monte Carlo modeling of fluorescence in tissues in the UV-visible spectrum," J. Biomed. Opt. **8**, 223–236 (2003).

[97] D. Y. Churmakov, I. V. Meglinski, and D. A. Greenhalgh, "Amending of fluorescence sensor signal localization in human skin by matching of the refractive index," J. Biomed. Opt. **9**, 339–346 (2004).

[98] A. M. K. Enejder, T.-W. Koo, J. Oh, M. Hunter, S. Sasic, M. S. Feld, and G. L. Horowitz, "Blood analysis by Raman spectroscopy," Opt. Lett. **27**, 2004–2006 (2002).

[99] P. Matousek, M. D. Morris, N. Everall, I. P. Clark, M. Towrie, E. Draper, A. Goodship, and A. W. Parker, "Numerical simulations of subsurface probing in diffusely scattering media using spatially offset Raman spectroscopy," Appl. Spectrosc. **59**, 1485–1492 (2005).

[100] T. Chaigne, O. Katz, A. C. Boccara, M. Fink, E. Bossy, and S. Gigan, "Controlling light in scattering media non-invasively using the photoacoustic trans-

mission matrix," Nat. Photonics **8**, 58–64 (2014).

[101] C. L. Evans, E. O. Potma, M. Puoris'haag, D. Côté, C. P. Lin, and X. S. Xie, "Chemical Imaging of tissue in vivo with video-rate coherent anti-Stokes Raman scattering microscopy," Proc. Natl. Acad. Sci. U. S. A. **102**, 16807–16812 (2005).

[102] T. W. Kee and M. T. Cicerone, "Simple approach to one-laser, broadband coherent anti-Stokes Raman scattering microscopy," Opt. Lett. **29**, 2701–2703 (2004).

[103] G. I. Petrov, R. Arora, V. V. Yakovlev, X. Wang, A. V. Sokolov, and M. O. Scully, "Comparison of coherent and spontaneous Raman microspectroscopies for noninvasive detection of single bacterial endospores," Proc. Natl. Acad. Sci. U. S. A. **104**, 7776–7779 (2007).

[104] R. Arora, G. I. Petrov, V. V. Yakovlev, and M. O. Scully, "Chemical analysis of molecular species through turbid medium," Anal. Chem. **86**, 1445–1451 (2014).

[105] C. M. Blanca and C. Saloma, "Monte Carlo analysis of two-photon fluorescence imaging through a scattering medium," Appl. Opt. **37**, 8092–8102 (1998).

[106] R. L. Burden and J. D. Faires, *Numerical Analysis* (Brookes/Cole, Boston, MA, 2010), 9th ed.

[107] R. P. Brent, *Algorithms for Minimization Without Derivatives* (Dover Publications, 1973), 1st ed.

[108] H. C. de Hulst, *Multiple light scattering: tables, formulas, and applications* (Academic press, 1980).

[109] N. Bachelard, P. Gaikwad, R. Backov, P. Sebbah, and R. A. L. Vallée, "Disorder as a Playground for the Coexistence of Optical Nonlinear Effects: Competition

between Random Lasing and Stimulated Raman Scattering in Complex Porous Materials," ACS Photonics p. 10.1021/ph500280m (2014).

[110] W. E. Martin and R. J. Winfield, "Nonlinear effects on pulsed laser propagation in the atmosphere," Appl. Opt. **27**, 567–577 (1988).

[111] B. H. Hokr, G. D. Noojin, G. I. Petrov, H. T. Beier, R. J. Thomas, B. A. Rockwell, and V. V. Yakovlev, "How to drive CARS in reverse," J. Mod. Opt. **61**, 53–56 (2014).

[112] Q. Fang and D. A. Boas, "Monte Carlo simulation of photon migration in 3D turbid media accelerated by graphics processing units," Opt. Express **17**, 20178 (2009).

[113] M. Matsumoto and T. Nishimura, "Mersenne twister: a 623-dimensionally equidistributed uniform pseudo-random number generator," ACM Trans. Model. Comput. Simul. **8**, 3–30 (1998).

[114] B. H. Hokr, J. N. Bixler, and V. V. Yakovlev, "Higher order processes in random Raman lasing," Appl. Phys. A **117**, 681–685 (2014).

[115] A. Taflove and S. C. Hagness, *Computational Electrodynamics: The Finite-Difference Time-Domain Method* (Artech House, 2005), 3rd ed.

[116] M. Xu, "Electric field Monte Carlo simulation of polarized light propagation in turbid media," Opt. Express **12**, 6530 (2004).

[117] A. Doronin, C. Macdonald, and I. Meglinski, "Propagation of coherent polarized light in turbid highly scattering medium." J. Biomed. Opt. **19**, 025005 (2014).

[118] A. Doronin, A. J. Radosevich, V. Backman, and I. Meglinski, "Two electric field Monte Carlo models of coherent backscattering of polarized light," J. Opt. Soc. Am. A **31**, 2394 (2014).

[119] D. S. Wiersma and A. Lagendijk, "Light diffusion with gain and random lasers," Phys. Rev. E **54**, 4256 (1996).

[120] D. S. Wiersma, M. P. van Albada, and A. Lagendijk, "Coherent backscattering of light from amplifying random media," Phys. Rev. Lett. **75**, 1739–1742 (1995).

[121] D. S. Wiersma, P. Bartolini, A. Lagendijk, and R. Righini, "Localization of light in a disordered medium," Nature **390**, 671–673 (1997).

[122] A. A. Chabanov, M. Stoytchev, and A. Z. Genack, "Statistical signatures of photon localization," Nature **404**, 850–853 (2000).

[123] S. E. Skipetrov and B. A. Van Tiggelen, "Dynamics of Anderson localization in open 3D media," Phys. Rev. Lett. **96**, 43902 (2006).

[124] T. Schwartz, G. Bartal, S. Fishman, and M. Segev, "Transport and Anderson localization in disordered two-dimensional photonic lattices," Nature **446**, 52–55 (2007).

[125] R. Arora, G. I. Petrov, and V. V. Yakovlev, "Hyperspectral coherent anti-Stokes Raman scattering microscopy imaging through turbid medium," J. Biomed. Opt. **16**, 21116 (2011).

[126] V. V. Yakovlev, G. D. Noojin, M. L. Denton, B. A. Rockwell, and R. J. Thomas, "Monitoring stimulated Raman scattering with photoacoustic detection," Opt. Lett. **36**, 1233–1235 (2011).

[127] V. V. Yakovlev, G. I. Petrov, H. F. Zhang, G. D. Noojin, P. A. Thomas, M. L. Denton, B. A. Rockwell, and R. J. Thomas, "Chemically specific imaging through stimulated Raman photoexcitation and ultrasound detection: minireview," Aust. J. Chem. **65**, 260–265 (2012).

[128] M. Zhi and A. V. Sokolov, "Broadband coherent light generation in a Raman-active crystal driven by two-color femtosecond laser pulses," Opt. Lett. **32**, 2251–2253 (2007).

[129] J. Liu, P. D. Garcia, S. Ek, N. Gregersen, T. Suhr, M. Schubert, J. Mørk, S. Stobbe, and P. Lodahl, "Random nanolasing in the Anderson localized regime." Nat. Nanotechnol. **9**, 285–9 (2014).

[130] P. W. Anderson, "Absence of diffusion in certain random lattices," Phys. Rev. **109**, 1492–1505 (1958).

[131] P. A. Lee, "Disordered electronic systems," Rev. Mod. Phys. **57**, 287–337 (1985).

[132] B. H. Hokr, M. S. Schmidt, J. N. Bixler, P. N. Dyer, G. D. Noojin, B. Redding, R. J. Thomas, B. A. Rockwell, H. Cao, V. V. Yakovlev, and M. O. Scully, "A narrow-band speckle-free light source via random Raman lasing," J. Mod. Opt. **63**, 46–49 (2016).

[133] E. Akkermans and G. Montambaux, *Mesoscopic Physics of Electrons and Photons* (Cambridge University Press, 2007).

[134] E. M. Patterson, C. E. Shelden, and B. H. Stockton, "Kubelka-Munk optical properties of a barium sulfate white reflectance standard." Appl. Opt. **16**, 729–32 (1977).

[135] H. Türeci, A. Stone, and B. Collier, "Self-consistent multimode lasing theory for complex or random lasing media," Phys. Rev. A **74**, 043822 (2006).

[136] L. Ge, Y. D. Chong, and A. D. Stone, "Steady-state ab initio laser theory: Generalizations and analytic results," Phys. Rev. A **82**, 063824 (2010).

[137] A. Cerjan, Y. Chong, L. Ge, and A. D. Stone, "Steady-state ab initio laser theory for N-level lasers." Opt. Express **20**, 474–88 (2012).

[138] A. Cerjan, Y. D. Chong, and A. D. Stone, "Steady-state ab initio laser theory for complex gain media." Opt. Express **23**, 6455–77 (2015).

[139] J. W. Goodman, *Speckle Phenomena in Optics: Theory and Applications* (Roberts and Company Publishers, 2007).

[140] J. D. Briers, G. Richards, and X. W. He, "Capillary Blood Flow Monitoring Using Laser Speckle Contrast Analysis (LASCA)." J. Biomed. Opt. **4**, 164–75 (1999).

[141] G. J. Richards and J. D. Briers, "Capillary-blood-flow monitoring using laser speckle contrast analysis (LASCA): improving the dynamic range," Proc. SPIE 2981, Coherence Domain Opt. Methods Biomed. Sci. Clin. Appl. **160**, 160–171 (1997).

[142] J. Liu, J. Dai, S. L. Chin, and X.-C. Zhang, "Broadband terahertz wave remote sensing using coherent manipulation of fluorescence from asymmetrically ionized gases," Nat. Photonics **4**, 627–631 (2010).

[143] A. K. Misra, S. K. Sharma, T. E. Acosta, J. N. Porter, and D. E. Bates, "Single-pulse standoff Raman detection of chemicals from 120 m distance during daytime," Appl. Spectrosc. **66**, 1279–1285 (2012).

[144] P. Rohwetter, J. Yu, G. Méjean, K. Stelmaszczyk, E. Salmon, J. Kasparian, J.-P. Wolf, and L. Wöste, "Remote LIBS with ultrashort pulses: characteristics in picosecond and femtosecond regimes," J. Anal. At. Spectrom. **19**, 437–444 (2004).

[145] R. Munro, R. Siddans, W. J. Reburn, and B. J. Kerridge, "Direct measurement of tropospheric ozone distributions from space," Nature **392**, 168–171 (1998).

[146] A. Ansmann, M. Riebesell, and C. Weitkamp, "Measurement of atmospheric aerosol extinction profiles with a Raman lidar," Opt. Lett. **15**, 746–748 (1990).

[147] J. Kasparian, M. Rodríguez, G. Méjean, J. Yu, E. Salmon, H. Wille, R. Bourayou, S. Frey, Y.-B. André, A. Mysyrowicz, and Others, "White-light filaments for atmospheric analysis," Science (80-.). **301**, 61–64 (2003).

[148] D. Pestov, X. Wang, G. O. Ariunbold, R. K. Murawski, V. A. Sautenkov, A. Dogariu, A. V. Sokolov, and M. O. Scully, "Single-shot detection of bacterial endospores via coherent Raman spectroscopy," Proc. Natl. Acad. Sci. U. S. A. **105**, 422–427 (2008).

[149] F. Poulet, J.-P. Bibring, J. F. Mustard, A. Gendrin, N. Mangold, Y. Langevin, R. E. Arvidson, B. Gondet, C. Gomez, M. Berthé, and Others, "Phyllosilicates on Mars and implications for early Martian climate," Nature **438**, 623–627 (2005).

[150] D. S. Moore, "Instrumentation for trace detection of high explosives," Rev. Sci. Instrum. **75**, 2499–2512 (2004).

[151] S. Wallin, A. Pettersson, H. Östmark, and A. Hobro, "Laser-based standoff detection of explosives: a critical review," Anal. Bioanal. Chem. **395**, 259–274 (2009).

[152] P. R. Hemmer, R. B. Miles, P. Polynkin, T. Siebert, A. V. Sokolov, P. Sprangle, and M. O. Scully, "Standoff spectroscopy via remote generation of a backward-propagating laser beam," Proc. Natl. Acad. Sci. U. S. A. **108**, 3130–3134 (2011).

[153] A. Dogariu, J. B. Michael, M. O. Scully, and R. B. Miles, "High-gain backward lasing in air," Science (80-.). **331**, 442–445 (2011).

[154] A. J. Traverso, R. Sanchez-Gonzalez, L. Yuan, K. Wang, D. V. Voronine, A. M. Zheltikov, Y. Rostovtsev, V. A. Sautenkov, A. V. Sokolov, S. W. North, and Others, "Coherence brightened laser source for atmospheric remote sensing," Proc. Natl. Acad. Sci. U. S. A. **109**, 15185–15190 (2012).

[155] V. Kocharovsky, S. Cameron, K. Lehmann, R. Lucht, R. Miles, Y. Rostovtsev, W. Warren, G. R. Welch, and M. O. Scully, "Gain-swept superradiance applied to the stand-off detection of trace impurities in the atmosphere," Proc. Natl. Acad. Sci. U. S. A. **102**, 7806–7811 (2005).

[156] M. O. Scully, G. W. Kattawar, R. P. Lucht, T. Opatrnỳ, H. Pilloff, A. Rebane, A. V. Sokolov, and M. S. Zubairy, "FAST CARS: Engineering a laser spectroscopic technique for rapid identification of bacterial spores," Proc. Natl. Acad. Sci. U. S. A. **99**, 10994–11001 (2002).

[157] B. H. Hokr, M. Cone, J. D. Mason, H. T. Beier, B. A. Rockwll, R. J. Thomas, G. D. Noojin, G. I. Petrov, L. A. Golovan, and V. V. Yakovlev, "Random Raman lasing," arXiv e-print **arXiv:1307** (2013).

[158] O. Katz, E. Small, and Y. Silberberg, "Looking around corners and through thin turbid layers in real time with scattered incoherent light," Nat. Photonics **6**, 549–553 (2012).

[159] B. L. Welch, "The generalization ofstudent's' problem when several different population variances are involved," Biometrika pp. 28–35 (1947).

[160] C. A. Lieber and A. Mahadevan-Jansen, "Automated method for subtraction of fluorescence from biological Raman spectra," Appl. Spectrosc. **57**, 1363–1367 (2003).

[161] H. T. Beier, G. D. Noojin, and B. A. Rockwell, "Stimulated Raman scattering using a single femtosecond oscillator with flexibility for imaging and spectral applications." Opt. Express **19**, 18885–92 (2011).

[162] Y. Ozeki, W. Umemura, Y. Otsuka, S. Satoh, H. Hashimoto, K. Sumimura, N. Nishizawa, K. Fukui, and K. Itoh, "High-speed molecular spectral imaging of tissue with stimulated Raman scattering," Nat. Photonics **6**, 845–851 (2012).

[163] Z. Meng, G. I. Petrov, and V. V. Yakovlev, "Continuous-wave stimulated Raman scattering (cwSRS) microscopy," Appl. Phys. B Lasers Opt. **112**, 99–103 (2013).

[164] C. H. Camp Jr, Y. J. Lee, J. M. Heddleston, C. M. Hartshorn, A. R. H. Walker, J. N. Rich, J. D. Lathia, and M. T. Cicerone, "High-speed coherent Raman fingerprint imaging of biological tissues," Nat. Photonics **8**, 627–634 (2014).

[165] W. Denk, J. H. Strickler, and W. W. Webb, "Two-photon laser scanning fluorescence microscopy," Science (80-.). **248**, 73–76 (1990).

[166] S. W. Hell and J. Wichmann, "Breaking the diffraction resolution limit by stimulated emission: stimulated-emission-depletion fluorescence microscopy," Opt. Lett. **19**, 780 (1994).

[167] J. W. Lichtman and J.-A. Conchello, "Fluorescence microscopy." Nat. Methods **2**, 910–9 (2005).

[168] D. F. Albeanu, E. Soucy, T. F. Sato, M. Meister, and V. N. Murthy, "LED arrays as cost effective and efficient light sources for widefield microscopy." PLoS One **3**, e2146 (2008).

[169] M. Nixon, B. Redding, A. A. Friesem, H. Cao, and N. Davidson, "Efficient method for controlling the spatial coherence of a laser." Opt. Lett. **38**, 3858–61 (2013).

[170] J. Noack, D. X. Hammer, G. D. Noojin, B. A. Rockwell, and A. Vogel, "Influence of pulse duration on mechanical effects after laser-induced breakdown in water," J. Appl. Phys. **83**, 7488 (1998).

[171] A. Vogel, "Shock wave emission and cavitation bubble generation by picosecond and nanosecond optical breakdown in water," J. Acoust. Soc. Am. **100**, 148 (1996).

[172] L. Gao, J. Liang, C. Li, and L. V. Wang, "Single-shot compressed ultrafast photography at one hundred billion frames per second," Nature **516**, 74–77 (2014).